UNIVERSITY
OF TRENTO - Italy
DEPARTMENT OF INDUSTRIAL ENGINEERING

XXVI cycle

Doctoral School in Materials Science and Engineering

Cu_2ZnSnS_4 thin films and solar cells: material and device characterization

An investigation into the stoichiometry effect on CZTS microstructure and optoelectronic properties

Claudia Malerba

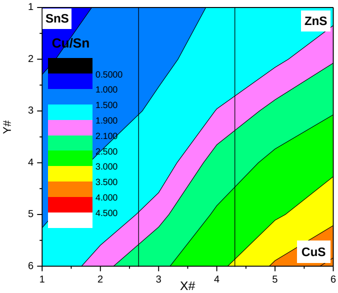

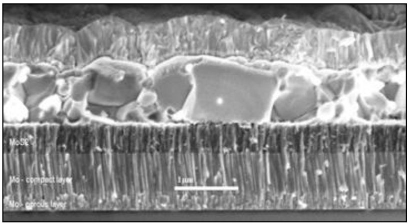

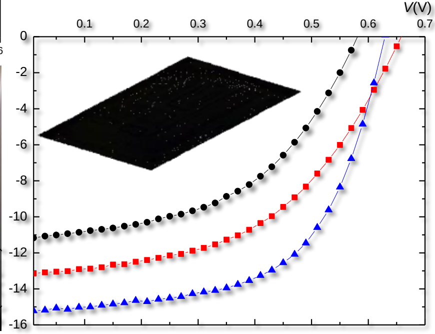

June 2014

Cu_2ZnSnS_4 THIN FILMS AND SOLAR CELLS: MATERIAL AND DEVICE CHARACTERIZATION

AN INVESTIGATION INTO THE STOICHIOMETRY EFFECT ON CZTS MICROSTRUCTURE AND OPTOELECTRONIC PROPERTIES

Claudia Malerba
E-mail: claudia.malerba-1@unitn.it

Approved by:
Prof. Paolo Scardi, Advisor
Department of Civil, Environmental and Mechanical Engineering
University of Trento, Italy.

Dr. Alberto Mittiga, co-advisor
Enea-Casaccia Research Centre
Rome, Italy.

Ph.D. Commission:
Prof. Paolo Scardi,
Department of Civil, Environmental and Mechanical Engineering
University of Trento, Italy.

Prof. Rachel Morrish,
Department of Chemical Engineering
Colorado School of Mines, Golden, US.

Prof. Maurizio Acciarri,
Department of Material Science & MIB-SOLAR
University of Milan-Bicocca, Italy.

University of Trento,
Department of Industrial Engineering

June 2014

University of Trento - Department of Industrial Engineering

Doctoral Thesis

Claudia Malerba - 2014
Published in Trento (Italy) – by University of Trento

“Learn from yesterday,
live for today,
hope for tomorrow.
The important thing is not to stop questioning.”

Albert Einstein

Abstract

Cu_2ZnSnS_4 (CZTS) quaternary compound has attracted much attention in the last years as new abundant, low cost and non-toxic material, with desirable properties for thin film photovoltaic (PV) applications.

In this work, CZTS thin films were grown using two different processes, based on vacuum deposition of precursors, followed by a heat treatment in sulphur atmosphere. The precursors were deposited using two different approaches: (i) electron-beam evaporation of multiple stacks made of ZnS, Sn and Cu and (ii) co-sputtering deposition of the three binary sulphides CuS, SnS and ZnS.

All the materials were characterized both as isolated films and as absorber layer in solar cells, produced using the typical structure Mo/CZTS/CdS/i:Zno/AZO.

Both growth processes were found to give good quality kesterite films, showing CZTS as the main phase, large grains and suitable properties for PV application, but higher homogeneity and stoichiometry control were achieved using the co-sputtering route.

A detailed investigation on CZTS optical properties, microstructure, intrinsic defect density and their correlation with the material composition is presented. A strong effect of the tin content on the bandgap energy, sub-gap absorption coefficient, crystalline domain and grain size is shown and a model based on the increase of the intrinsic defect density induced by a reduced tin content is proposed. These studies suggested a correlation between the increase of the bandgap energy and the improvement of the material quality, which was also confirmed by the performances of the final devices.

CZTS thin films were then assembled into the solar cells and their properties as absorber layer were optimized by varying both composition and thickness.

CZTS samples produced from stacked evaporated precursors allowed achieving a maximum efficiency of 3.2%, but reproducibility limits of the evaporation process made difficult to obtain further and rapid efficiency improvements.

The co-sputtering route was demonstrated to be a more successful strategy, assuring a fine-control of the film composition with good process reproducibility. A fast improvement of solar cell efficiency was obtained using this approach and a maximum efficiency of 5.7% was achieved. The relationship between the absorber layer stoichiometry and the device performances was investigated: the effect of the Zn enrichment and a possible influence of the Cu/Sn ratio on the device performances are discussed.

Investigation on CZTS/CdS and CZTS/MoS_2 interfaces revealed that the optimization of both buffer-layer and back-contact technology is a primary need for further improvement of CZTS solar cells.

Acknowledgments

Before beginning this thesis, I would like to express my gratitude to the many people who contributed to its creation. I first thank my supervisor, Paolo Scardi, for giving me support and encouragement, and my co-supervisor, Alberto Mittiga, for sharing his experience and for giving me valuable advice on writing this thesis.

A special thanks to my colleagues and friends in Rome, Matteo Valentini and Francesco Biccari, who have been a great source of discussions and camaraderie during all the research activity and my friend and colleague Cristy Azanza, in Trento, for sharing her enthusiasm and expertise in material characterization.

Many others have contributed to the scientific content of this thesis. I want to thank Antonino Santoni for having conducted the XPS measurements; Mario Barozzi and Massimo Bersani for SIMS characterizations, Luciano Pilloni who taught me how to use SEM and EDX; Enrico Salza and Pietro Mangiapane for their technical support for deposition of Mo, ZnO and stacked precursors.

I am grateful to the Italian Ministry of Economic Development for funding the research activity, to the Research Center Enea-Casaccia and University of Trento for having involved me in this project. I am also grateful to the Doctoral School in Materials Science and Engineering and to the Department of Civil environmental and mechanical engineering of the University of Trento for providing me with conference funding and scholarships.

And I do not forget to thank those who ensured my well being while I worked on this thesis, in Trento as well as in Rome. In particular, a special thanks to Cristy, Luca, Alberto, Melanie for their friendship and the laughs in the “red small house” (which is not red!!!) of the microstructure labs; thanks to my housemates Fulvia, Eleonora and to all the guests of viapal23 for the funny time spent together in Trento, and thanks to all my friends in Rome (too many to list here but you know who you are!), for providing support and friendship that I needed.

With all the thanks I have left, I thank my family for encouraging and supporting me throughout my life and career and for being a constant presence during my many times of stress, excitement, frustration and celebration.

Grazie a tutti!

Table of contents

Chapter I

Chapter II

Chapter III

Chapter IV
CZTS thin films from co-sputtered precursors 75

Chapter V
Solar cells based on Cu_2ZnSnS_4 absorber layer: fabrication and characterization..99

Chapter I

Introduction

1.1 Advantages of thin film solar cells and limits of the actual technologies

Cu_2ZnSnS_4 quaternary compound has attracted much attention in the last years being an earth abundant, low cost and non-toxic material, with desirable properties for thin film photovoltaic (PV) applications.

Thin film solar cells (TFSCs) belong to the so-called *second-generation* PV, in which the active bulk-material, used as absorber layer in the standard (*first generation*) PV technology, is replaced by a thin-film, with typical thickness of micron.

The huge reduction of the active material requirement respect to the standard technology allows a large decrease of the device costs. Moreover, the large versatility in the device design and fabrication, due to the wide choice of different substrates (rigid, flexible) and deposition techniques for the different device layers, allow engineering and optimizing the solar cell stack in order to enhance the device performances [23]. Thin film PV has been therefore recognised as a promising strategy to obtain high efficiency and low cost devices, thus fulfilling the actual requirements for the increasing electrical demand.

TFSCs based on chalcogenide, such as $Cu(In,Ga)(S,Se)_2$ (CIGS) and CdTe, have shown significant improvement of the device efficiency in the last 30 years and have currently reached mass production. In 2014, small area CIGS solar cells have reached an efficiency of 20.9% [169] (close to the record efficiency of bulk-crystalline Si solar cells (25%) [47]) and large-area modules with efficiency of about 13-14% are currently produced on industrial scale. Even CdTe solar cells (with a record efficiency of 19.1% for research cell and 16.1%. for total area module [168]), have already an annual industrial production larger than 1.5 GW. Despite the large development of the actual chalcogenide-based PV, these technologies suffer from using toxic (Cd) and rare elements, such as In, Ga and Te, whose critical supply could be one of the main limits for the sustainability of these technologies in the years to come [26, 108, 24].

The development of new abundant, environmental friendly and low cost materials as possible alternative to CIGS alloys is a challenge to fulfil the requirements of PV massive production on terawatt scale foreseen in 2020-2040. [26, 49, 2].

1.2 $Cu_2ZnSnS(Se)_4$ compounds as alternative to CIGS alloys

In the last two decades, many efforts have been addressed to the development of a new class of quaternary compounds as possible candidates to replace CIGS in thin film solar cells. These materials can be thought of as a derivation of CIGS chalcopyrite structure, by a process known as “cross-substitution”, consisting in the replacement of one element (In or Ga in the present case) with a couple of two elements of different groups of the periodic table, keeping fixed the ratio between the number of atoms and valence electrons. The resulting materials are therefore quaternary compound given by the chemical formula Cu_2-*II*-*IV*-VI_4, where VI is a chalcogen element (S or Se) while II and IV represent divalent (Zn, Cd, Fe) and tetravalent (Sn, Ge, Si) elements, respectively.

Among the possible Cu_2-*II*-*IV*-VI_4 compounds, kesterites $Cu_2ZnSn(S,Se)_4$ (CZTS(Se)) are the most studied and the rapid improvement of photovoltaic performances obtained in the recent years makes these materials even much attractive.

Kesterites are very promising materials, being composed by low cost, widely available and non toxic elements (although selenium is sometimes added to the alloy) and showing desirable properties for thin film photovoltaic applications. CZT(S,Se) are spontaneously p-type semiconductors, with a direct band gap energy between 1 eV (for the pure selenide $Cu_2ZnSnSe_4$ alloy) and 1.5 eV (for the pure sulphide Cu_2ZnSnS_4), close to the optimal value to match the solar spectrum (in the limit of radiative recombination only, the theoretical conversion efficiency predicted by Schokley and Queisser for such semiconductors is as high as 30%). The direct band gap gives a high absorption coefficient, making these materials suitable as thin film photoactive layers, since a sensible absorption of the incoming light occurs within about one micron.

Solar cells based on a mixed sulphide-selenide $Cu_2ZnSnS_xSe_{4-x}$ absorber layer have recently reached an efficiency of 12.6% [162], while slightly lower efficiencies (with a record of 9.2% [74]) has been reported for Se-free CZTS compounds. Despite their current lower performances, the use of Se-free CZTS is obviously preferable from an environmental point of view as well as for the technical benefits related to its higher Eg value [139, 97] and extensive research in the kesterite field is currently addressed to the development of pure sulphide phase.

The present work focuses on Cu_2ZnSnS_4 compound and is devoted to clarify some issues that can be important both for a better understanding of the material physical properties and for its application as absorber layer in photovoltaic devices.

1.3 CZTS: history and research needs

First evidence of PV effect in CZTS heterojunctions was reported in 1988 by Ito and Nakazawa [62], using a Cu_2ZnSnS_4 thin film deposited by atom beam sputtering.
Thereafter, many works have been devoted to the development of this material as absorber layer and the extensive research led to a rapid and continuous improvement of CZTS solar cell performances. An efficiency of 6.7% was reported in 2008 by the Japanese group headed by Katagiri [72], using a Cu_2ZnSnS_4 thin film deposited by co-sputtering technique. A rapid improvement was then demonstrated: in 2011 the IBM group [139] reported a 8.4% efficiency solar cell obtained from co-evaporated CZTS; vacuum-deposition based CZTS submodules (about 5×5 cm^2-sized) with efficiency increasing from 6.2 [57] to 8.6% [143] have been reported by Solar Frontier between 2011 and 2012 and very recently an efficiency of 9.2% has been achieved [74].

Despite this rapid improvement, performances of CZTS based solar cells remain still far from their theoretical limit of about 30% [141]. The most important limiting factor has been identified with the low value of the open-circuit voltage (Voc) [116]. Even though an open circuit voltage of 711 mV has been recently achieved [143], Voc values are usually reported to be about 0.65 V, thus showing a large deficit with respect to the theoretical limit (Eg/q) of about 1.23 V predicted for CZTS-based solar cells ($Eg(CZTS) \approx 1.5$ eV).
Several factors can be responsible for the low Voc of the actual CZTS devices, depending both on the absorber layer quality, and on the device architecture.

CZTS phase stability and control of the intrinsic defects can be identified as the two major challenges to be addressed to further increase the material quality.
Spurious phase segregation is a widely reported problem in the CZTS literature. Indeed, the Cu_2S-ZnS-SnS_2 pseudoternary phase diagram predicts a narrow stability

region for CZTS phase [109] and even small deviations from stoichiometry can lead to the formation of secondary phases, which can be detrimental for photovoltaic performances. Copper compounds, such as Cu_xS_y and $Cu_{2-x}Sn_xS_3$, are known to be the most harmful [131], as their high conductivity can give rise to possible shunting paths, with consequential reduction of the Voc.

Cu-poor and Zn-rich composition would be desirable to prevent the formation of detrimental copper-sulphide phases and this could likely explain why the best solar cells have been historically obtained using such compositions. However, as a result of the Zn-rich stoichiometry, a ZnS phase is often detected even in the best solar cells. The effect of this phase on the device performances is still unclear, but its role seems to be not harmful [74].

A more critical issue to improve the material quality as absorber layer is the control of intrinsic defects. The low Voc has been indeed attributed to the electron-hole pair recombination phenomena, due to the activity of detrimental defects, which can be located into the bulk [17, 22, 120] as well as at the grain boundaries [6].

Theoretical works investigated the possible intrinsic defects, their formation energy and the position of their energy levels inside the bandgap [18, 22, 17]. However, further efforts are required to experimentally clarify which defects are produced by the off-stoichiometry compositions and non-equilibrium conditions, typical of the actual fabrication processes. A deep knowledge of defect nature, their formation mechanism, location and impact on CZTS opto-electronic properties is indeed a very important issue to identify both the proper growth conditions and the optimal film composition that allow suppressing harmful defect formation.

A clear understanding of these issues still remains an open problem: despite the difficulty related to different growth methods and process conditions, the role of the film composition on the material physical properties and on its intrinsic defect density is still unclear and part of the present work is devoted to investigate on this problem.

Beside the optimization of the absorber layer, improvement of solar cell architecture and engineering is also required to further increase the device efficiency.

One of the advantages of similarity between kesterite and chalcopyrite is that the standard device structure adopted for CIGS can be directly extended to CZTS, by simply replacing CIGS absorber layer with p-type CZTS thin films. A scheme of the typical solar cell stack is reported in Figure 1.

The back contact is made of molybdenum, deposited onto soda lime glass (SLG) substrate. At the front interface, a CdS (n-type) buffer layer is deposited onto the CZTS (p-type) absorber, thus forming a p-n rectifying heterojunction, which allows charge separation. The top contact (referred to as the “window layer”) is obtained by deposition of a Transparent Conductive Oxide (TCO), usually made of aluminum n-doped ZnO (AZO). A thin layer of intrinsic zinc oxide (i:ZnO) is often introduced between CdS buffer and AZO layer to prevent possible shunting paths, even though high efficiency devices have been obtained in the literature without i:ZnO [69]. Solar cell stack is then usually completed with a metal contact grid and a MgF_2 anti-reflection coating, used to enhance the charge collection and to reduce the reflected-light loss, respectively.

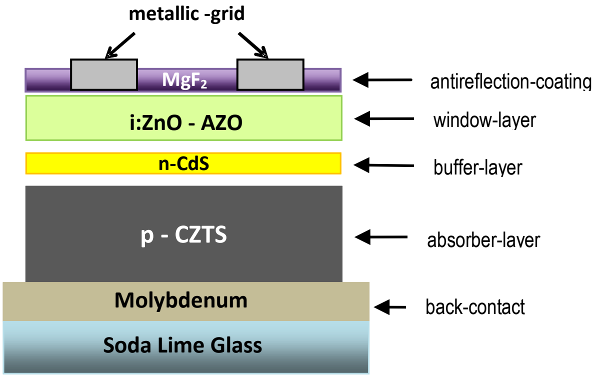

Figure 1: Typical structure of solar cells based on CZTS absorber layer.

When CZTS is used in substitution for CIGS absorber, the back and the front interfaces can show off-optimum behaviour, thus limiting the device performances.

Possible non-ohmic behaviour of the back contact has been suggested in the literature [160, 50, 140] as a limiting factor for the device performances. This behaviour has been imputed to the formation of a rectifying Schottky barrier between the absorber and the MoS_2 interfacial layer, which usually forms as a result of the absorber fabrication process (which typically requires a heat treatment in sulphur atmosphere). However, the role of MoS_2 is still unclear, as, if grown with proper electrical properties, its formation could be beneficial and even necessary to provide a good ohmic contact between CZTS and Mo [12] (as it also happens in CIGS devices [156]).

Another important issue for the development of CZTS technology concerns the absorber-buffer layer interface. The typical material used as buffer layer is CdS, being found to give the best performances devices both in CIGS and CZTS. Due to its 2.4 eV energy gap, the use of CdS gives rise to a parasitic absorption in the blue energy region (for wavelength lower than 500 nm). To minimize these undesired absorption phenomena, typical CdS thicknesses reported in the literature are less than 100 nm, but alternative buffer layers with wider band-gap energy than CdS would be preferable.

A more critical issue is the band-alignment between CdS and CZTS. Off-optimum band alignment (*cliff-like*) at CZTS/CdS heterojunction has been widely reported in the literature [10, 142, 21] and it has been identified as a detrimental factor for the device efficiency, because of the enhanced interfacial recombination phenomena [160, 50, 99]. However, the values of the conduction and valence band offset are still controversial and there are even works reporting on optimal band matching (*spike-like* alignment) between CZTS and CdS [53], which, on the contrary, would minimize electron-hole pair recombination at the interface.

Many efforts are currently devoted to the engineering of alternative buffer layers, in order to optimize the interface band-offset and to reduce parasitic absorption phenomena. Cd-free buffer layers are obviously desirable from an environmental point of view, to avoid using a toxic material. Promising results by using not-specified Zn-based and In-based buffer layer have been recently reported in the literature [58]. However, CdS has to date yielded the best device performances and it has been also used in the present work as the standard buffer layer for device fabrication.

Part of our research on CZTS solar cells has been devoted to investigate on the role of MoS_2 on the back contact behaviour and to clarify the controversy on the band-alignment at the CZTS/CdS front interface.

1.4 Framework and aim of the work

The present thesis is in the frame of a wider project for renewable and sustainable energy promoted by the Italian Ministry of Economic Development. Part of the funding has been devoted to Enea-Research Center for the development of Cu_2ZnSnS_4 compounds as innovative materials for photovoltaic applications, with the objective of achieving conversion efficiency of 5% in three years.

The research activity started in 2010 and has been carried out in Enea laboratories in Rome, in collaboration with University of Trento and University of Rome.

At that time, the activities on this subject at Trento as well as at Rome were just at the beginning and the achievement of the objective required different kinds of activities, concerning both the material synthesis and the development of device technology.

Part of the work has been devoted to the development of the facilities and to the optimization of the techniques necessary for the growth of CZTS thin films, with the aim of obtaining materials with sufficiently good properties for PV application. Beside the work on material synthesis, parallel activities have been devoted to the

development of all the technologies and deposition processes necessary for solar cell fabrication.
The work has been organized by setting the following interim goals:

Material research area:

1) Development of experimental processes to fabricate CZTS thin films with correct phase, good crystallinity, uniform and controlled composition.

2) Insight into CZTS basic physical properties to investigate some important issues of scientific interest, which can also be important for the optimization of material as absorber layer. The main points to explore are the CZTS optical properties, microstructure, intrinsic defect density and their correlation with the material composition.

Device research area:

3) Development of the growth processes for the deposition of all the layers necessary for solar cell fabrication. Each material (back-contact, buffer and window layer) must show suitable properties for its application into the solar cell stack.

1.5 Strategy and achievement of the objectives

For a fast improvement of CZTS solar cells, two different activities have been developed in the material research area, mainly differing for the growth methods used for the synthesis of CZTS thin films.

At start of this work, we prepared an experimental set-up to produce CZTS thin films by sulphurization of stacked layer precursors, containing all the metals (Zn, Cu and Sn, or their sulphides) necessary for CZTS phase formation. Precursors have been deposited by electron-beam evaporation and have been annealed in a sulphur atmosphere in a tube oven. A similar approach was already been reported in the literature and was demonstrated to give good results in terms of device efficiency. One of the leader groups in the CZTS field, headed by Prof. Katagiri, reported on CZTS solar cells with over 5% of efficiency for CZTS absorber layer grown from stacked evaporated precursors, which were then annealed in H_2S flux [69]. Our approach is slightly different, as elemental sulphur is used instead of H_2S.
This growth process allows us to quickly launch the research activity, as an electron-beam evaporator and a tube-oven were available facilities in the ENEA laboratory.
The process was demonstrated to give good quality CZTS thin films, showing CZTS as the main crystalline phase, large grain size, with suitable properties for PV

applications. Solar cells with efficiencies over 3% have been produced using this approach.

However, an accurate and fine control of the film composition was an issue. Despite the film stoichiometry can be controlled by varying the metal proportions into the starting precursors, the growth method, with the available facilities, revealed some limits in terms of sample homogeneity, control and reproducibility of the process, thus making difficult to obtain fast improvements of the device performances.
Despite the possibility for further development of CZTS thin films produced from staked precursors, the activities on these materials were stopped in 2012, to explore a new promising fabrication route, based on co-sputtered deposition of precursors.

With the new process, adopted in a second stage of our activity after an upgrade of the deposition systems, CZTS thin films were grown by sulphurization of precursors obtained by simultaneous sputtering of the three binary sulphides: CuS, ZnS, SnS.
The use of co-deposited precursors was already suggested in the literature as a promising strategy in terms of uniformity and control of material composition [72, 160], as all the elements necessary for CZTS phase formation are already present and homogeneously mixed in the starting film.
However, at the beginning of our activity, the co-sputtering from three different targets was not a widely explored route, being reported only by the Katagiri pioneering group, which used elemental Cu, ZnS and SnS compounds as sputtering sources. Co-sputtering from the three binary sulphides adopted in the present work is a quite innovative route, as both metals and sulphur can be incorporated in the correct proportion into the starting precursor. A similar approach, but based on Cu_2S, SnS_2 and ZnS targets, has then been reported in the course of our activities [59].

Co-sputtering method allowed obtaining good results in terms of control and reproducibility of the process. The chemical homogeneity of both precursor and final material, together with the possibility for an accurate control of the film stoichiometry by properly setting the sputtering powers, allowed fulfilling all the requirements of the first interim goal and also gave the possibility for a fast optimization of materials as absorber layers. CZTS solar cells produced from co-sputtered materials achieved efficiency close to 6% in 2013, thus fully achieving the final goal of the project.

1.6 Structure of the work

A brief overview of CZTS basic properties is presented in Chapter II. This thesis is then structured in three main experimental chapters:

- Chapter III focuses on CZTS thin films produced by sulphurization of stacked layer precursors. After a description of the growth process, the characterization of the optimized materials in terms of chemical composition, optical properties and microstructure is presented. A detailed investigation on the stoichiometry effect on CZTS physical properties, such as energy gap, grain dimensions and intrinsic defect density is also presented in this chapter.

- Chapter IV concerns the development of CZTS thin films by co-sputtering deposition technique and mainly focuses on the optimization of these materials in view of their application as absorber layers in solar cells.

- Chapter V is related to the research activity on CZTS devices and it is structured in three main parts: in the first part, solar cell fabrication processes are described and the characterization of all the layers (back-contact, buffer and window layer) necessary for the device is presented. The second part concerns our investigations on the back contact and front interface, while the third part focuses on the efficiency evolution of solar cells produced by using both staked evaporated and co-sputtered precursors.

Conclusion and future perspectives are then presented in Chapter VI.

Chapter II

General properties of Cu_2ZnSnS_4: a brief overview

2.1 Crystal structure and polymorphism

Cu_2ZnSnS_4 compounds may exist in two main crystal structures, known as kesterite and stannite [54]. Both are tetragonal structures, consisting in a cubic closed packed array of sulphur anions, with cations occupying one half of the tetrahedral voids, with a stacking similar to zincblende. The structural differences are related to a different order in the cation sublattice: kesterite, with space group $I\bar{4}$, is characterized by alternating cation layers of CuSn, CuZn, CuSn and CuZn at z=0, 1/4, 1/2 and 3/4, respectively, whereas in stannite structure, with $I\bar{4}2m$ symmetry, ZnS layers alteranate with Cu2 layers. Tin and sulphur ions occupy the same lattice positions in both structures. Tetragonal supercells of kesterite and stannite are reported in Figure 2. The lattice constants *a* and *c* are similar for both structures: according to Paier et al. [112], for kesterite structure $a \approx 5.46$ Å and $c \approx 10.93$ Å, but slightly different values can be found in other works [114, 126].

All the ab-initio calculations [112, 114] predict that the stable structure for Cu_2ZnSnS_4 is kesterite (possibly along with cation disorder within the Cu–Zn layer), but different polymorphs, with only slightly higher total energy [112, 173] have been considered in the literature. The most important is stannite, with an energy difference (ΔE) respect

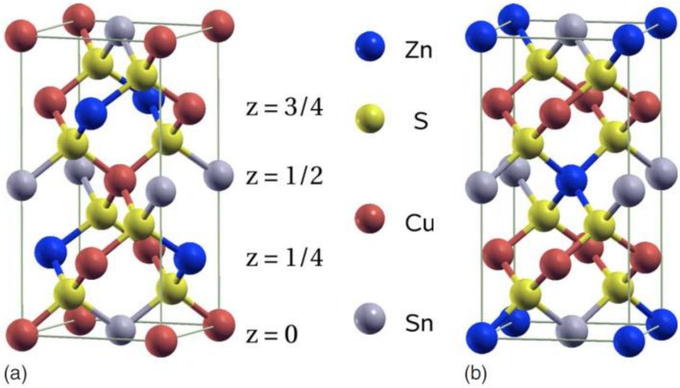

Figure 2: Schematic representations of the kesterite (a) and stannite (b) structures, from [112]

to kesterite of only few meV per atom (ΔE values between 1.3 and 3.4 meV/at can be found in the literature [19, 112, 114]). Additional tetragonal structural modifications have been predicted [112, 173, 137]. These modifications belong to the space groups $P\bar{4}2c$, $P\bar{4}2_1c$ and $P2$ and are obtained by the exchange of two ions on the cation sublattice. The bandgap and the formation energies of the CZTS structures generally considered in the literature are reported in Table 1. The total energy excess (ΔE) of $P\bar{4}2c$ and $I\bar{4}2m$ symmetry structures respect to kesterite stable state ($I\bar{4}$) is much lower than kT at room temperature, so that the possible co-existence of these three polymorphs has been suggested in the literature [137, 61].

These theoretical results are partially confirmed by neutron diffraction data reported in [126], revealing a disordered distribution of Zn and Cu atoms in CZTS samples, showing kesterite structure.

Table 1: Energy gap (Eg) and formation energy difference (ΔE) with respect to the stable kesterite state as obtained from the ab-initio calculations reported in [112].

Symmetry	$I\bar{4}$	$P\bar{4}2c$	$I\bar{4}2m$	$P2$	$P\bar{4}2_1c$
*E*g (eV)	1.49	1.46	1.29	1.07	1.20
ΔE(meV/at)	0	0.75	3.37	17	24.4
structure	Kest.	Mod.	Stann.	Mod.	Mod.

2.2 *Opto-electronic properties*

2.2.1 Electronic Band structure and effective masses

The electronic structure of CZTS and CZTSe and other related compounds were investigated by first principle calculations in several works [104, 88, 114, 112] Details of the electronic band structure of CZTS(e) can be found in [114]. The results show a direct Γ-point energy gaps for both CZTS kesterite and stannite structures, with energy gap values of 1.56 and 1.42 eV, respectively. These values agree quite well with experimental works on CZTS single-crystals [60, 95], even though some spread of results (varying from 1.4 to 1.7 eV) can be found in the literature for CZTS thin films [95, 73, 148, 39, 102]. The electronic diagram and density of states (DOS) predicted by Persson [114] for Cu_2ZnSnS_4 kesterite structure are reported in Figure 3.

An isolated conduction band (CB) is predicted by these calculations: the energy gap between the lowest CB and higher lying CBs is about 1 eV, and thus the higher CBs do not contribute to the optical absorption in the low energy regime. As a consequence, a decrease of the CZTS absorption coefficient is expected at energy higher than about 2 eV, thus giving a peak in the absorption spectra. A similar behaviour is also expected for CZTSe [114], as confirmed by recent experimental work [51].

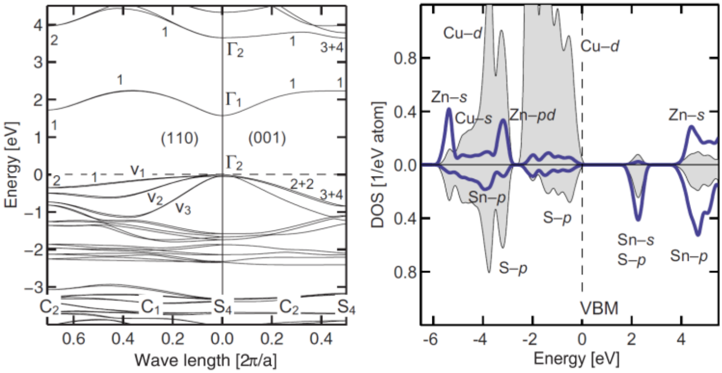

Figure 3: Electronic band structure of Cu_2ZnSnS_4 kesterite structure predicted by Persson [114].

First principle calculations by Persson [114] also provide important information on the charge carrier effective masses.

The results, reported in Table 2, predict a fairly good isotropic electron effective mass (m_e) of the lowest CB, whereas hole masses show strong anisotropy in both CZTS(e) kesterite and stannite-type structures. The value of electron effective mass is about 0.18 m_0 in CZTS and about 0.07 m_0 in CZTSe, comparable with that of CIGS (~0.20 m_0) and CIGSe (~0.10 m_0) [113]. The smaller electron masses in the Se-based compounds compared to the sulphide phases result in higher mobility of the minority carriers, so that a better response to an applied electric field is expected in CZTSe compared to CZTS. However, it has to be pointed out that the mobility is strongly influenced by scattering mechanisms and therefore it depends on the material quality. Some experimental values of the Hall mobility measured in CZTS and CZTSe samples are reported later on.

Table 2: Γ-point effective electron masses (m_e) and hole masses (m_{vn}, for n=$v1, v2, v3$, where $v1$ is the topos VB). The symbols ∥ and ⊥ are used for longitudinal and transverse masses respectively (from [114]).

Effective mass	kesterite	Stannite
$m_e^{\perp}$ $[m_0]$	0.18	0.17
$m_e^{\parallel}$ $[m_0]$	0.20	0.18
$m_{v1}^{\perp}$ $[m_0]$	0.71	0.33
$m_{v1}^{\parallel}$ $[m_0]$	0.22	0.84
$m_{v2}^{\perp}$ $[m_0]$	0.35	0.27
$m_{v2}^{\parallel}$ $[m_0]$	0.52	0.88
$m_{v3}^{\perp}$ $[m_0]$	0.26	0.73
$m_{v3}^{\parallel}$ $[m_0]$	0.76	0.17

Using the mass values reported before, it is possible to calculate the effective density of states in a given band (x) from the expression [147]:

$$N_x = 2\left(\frac{2\pi\widetilde{m}_x\, K_B T}{h^2}\right)^{3/2} = 2.5\cdot 10^{19}\left(\frac{\widetilde{m}_x}{m_0}\right)^{3/2} \quad ,$$

where $\widetilde{m}_x$ is the geometric mean of the effective masses of the free charge carrier (electron or hole) along the three directions of the ellipsoidal equipotential surfaces (centred at the : Γ −point):

$$\tilde{m}_x = \sqrt{m_2^{\parallel}(m_2^{\perp})^2} \quad \Rightarrow \quad \begin{cases} \tilde{m}_e = 0.186\, m_0 \\ \tilde{m}_{v1} = 0.48\, m_0 \\ \tilde{m}_{v2} = 0.40\, m_0 \\ \tilde{m}_{v3} = 0.371\, m_0 \end{cases}$$

The corresponding density of states in the CB and in the three VBs are about:

$$\begin{aligned} N_C &= 2.5 \cdot 10^{18}\, cm^{-3} \\ N_{v1} &= 8.3 \cdot 10^{18}\, cm^{-3} \\ N_{v2} &= 6.3 \cdot 10^{18}\, cm^{-3} \\ N_{v2} &= 5.6 \cdot 10^{18}\, cm^{-3} \end{aligned}$$

2.2.2 Intrinsic defects and electronic properties

In a quaternary compound such as CZTS, several intrinsic point defects are possible, including vacancies (V_{Cu}, V_{Zn}, V_{Sn}, and V_S), antisite defects (Cu_{Zn}, Zn_{Cu}, Cu_{Sn}, Sn_{Cu}, Zn_{Sn}, and Sn_{Zn}), and interstitial defects (Cu_i, Zn_i, and Sn_i). These defects can introduce shallow or deep levels within the bandgap, can show donor or acceptor behaviour, can act as traps or recombination centre, thus influencing the opto-electronic properties of the host material.

CZTS show spontaneous p-type conductivity. This behaviour has been attributed to the presence of intrinsic acceptor defects with low formation energy.

Theoretical calculations of defect formation in CZTS compounds have been actively reported since 2010 [20, 22, 103, 89]. The values of the intrinsic defect ionization levels within the band gap of Cu_2ZnSnS_4 predicted by Chen et al. [22] are summarized in Figure 4 [159].

According to these works, the copper vacancy results in a shallow acceptor level just above the valence band, while the Cu_{Zn} antisite results in a level 0.12 eV higher in energy. Contrary to CIS, in which the V_{Cu} is the dominant defects, ab-initio calculation [22, 103] show that in CZTS the intrinsic dominant defect is Cu_{Zn} antisite, showing the lowest formation energy. A negative value is reported in [103], whereas calculations reported in [22] predict that the Cu_{Zn} formation energy becomes negative for Fermi Level higher than 0.12 eV. Both works reveal a self-compensation mechanism, which prevents the possibility for a n-type doping and for a CZTS type-inversion at p-n heterojunctions.

In addition to the Cu_{Zn} antisites, other four dominant defects are predicted, showing a relatively low formation energy for Cu-poor CZTS composition (which is typically used in PV application). These defects, in order of increasing formation energy, are: V_{Cu}, Zn_{Sn}, V_{Zn} and Cu_{Sn}.

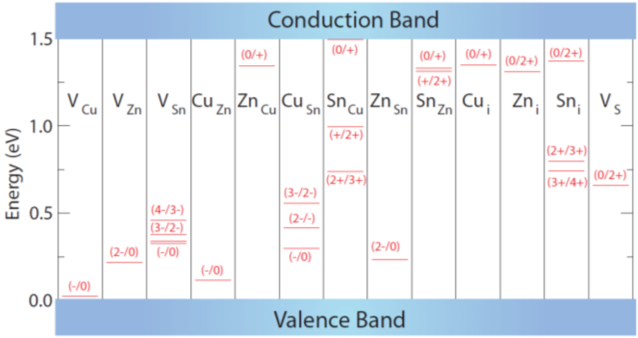

Figure 4: The ionization levels of intrinsic defects in the bandgap of Cu_2ZnSnS_4 [159].

Intrinsic defects play an important role in view of semiconductor performances as absorber layers. Deep levels are indeed detrimental for PV applications as they introduce traps or recombination centres for photogenerated electron-hole pairs.

First principle calculations reported in [22] predict the Cu_{Sn}^{3-} antisite as a deep level acceptor defect, with energy close to the midgap and with low formation energy. This defect is therefore expected to be the most active recombination centre in CZTS [120, 22]. However, the same calculations show that charge-compensated defect complexes such as [Cu_{Sn} + Sn_{Cu}] are likely to form and passivate deep levels in CZTS [22]. More recent calculations [18] also predict the [Cu_{Zn}+Sn_{Zn}] defect cluster as a detrimental defect for photovoltaic performances, showing relatively low formation energy and producing a deep donor level. According to these predictions, Cu-poor and Zn-rich composition would be desired to suppress the formation of these detrimental defects. This could also explain why the best solar cells have been historically produced using CZTS with such composition. In addition to the defect complexes previously mentioned, a large number of possibilities have been also predicted. Among them, those with the lowest formation energy (for Cu-poor composition) are [V_{Cu}^{-} + Zn_{Cu}^{+}], [Zn_{Sn}^{2-} + $2Zn_{Cu}^{+}$] [22] and [$2Cu_{Zn}$+Sn_{Zn}] [18].
The theoretical results reported in the literature and briefly described here give an important contribution to understand the electronic properties of CZTS and their relation with the material intrinsic defects. However, further investigations are necessary to understand the nature of different defects which may result from off-stoichiometry compositions and non-equilibrium conditions, typical of the actual fabrication processes, in order to control detrimental defects and improve the material quality as absorber layer.

2.2.3 Conductivity and mobility data

Experimental results confirm that CZTS is a spontaneously p-type semiconductor. A wide range of conductivity and mobility values can be found in the literature, depending on the film composition and growth technique [172, 148, 105, 174]. Free carrier mobility is strongly influenced by scattering mechanisms, and therefore different results are obtained depending on the material quality (defect density, presence of spurious phases).

Values between 5 and 12 cm^2/(V s) are reported for materials grown by sulphurization of metallic precursors deposited by ion-beam sputtering [172], whereas lower values (about 6 - 7 cm^2/(V s)) were found for precursors deposited by RF magnetron sputtering. Resistivity values lower than 1 Ω cm are reported for these samples. The highest mobility reported for CZTS is 30 cm^2/(V s) [84], obtained for a film grown by reactive co-sputtering deposition of metallic precursors in H_2S atmosphere. The final material showed a resistivity of 5.4 Ω cm.

High resistivity values (about 200 Ω cm) are reported in [105], where CZTS samples are obtained upon heat treatment in H_2S of quaternary polycrystalline precursors prepared by spray-deposition. A rapid decrease of resistivity (down to 10^{-2} Ω cm) was observed by the authors for increasing copper content and a similar trend was also recently reported for co-evaporated CZTSe samples [145]. For Cu-rich samples, conductive copper sulphide phases are often detected and are suggested to be responsible for the low sample resistivity [105], [148]. However, the high conductivity of Cu-rich CZTS samples could also depend on higher Cu_{Zn} defect concentration compared to stoichiometric film.

Some reported resistivity, mobility and hole density values obtained from Hall measurements are shown in Table 3.

Table 3: Reported resistivity, mobility and carrier density values as determined by Hall effect measurements.

ρ Ω cm	*μ* cm^2/(V s)	*p* cm^{-3}	*Ref.*
0.15	6.3	$8.2\cdot10^{18}$	[172]
0.13	6.0	$8.0\cdot10^{18}$	[148]
~ 0.13	12.6	$3.8\cdot10^{18}$	[174]
0.36	11.6	$4.5\cdot10^{17}$	[172]
5.4	30	$3.9\cdot10^{16}$	[84]

Estimates of the hole concentration were also obtained from Capacitance-Volatage (C-V) measurements [132, 69] performed on the final devices. For good performance solar cells, the hole density was found to be in the order of 10^{16}-10^{17} cm^{-3}, whereas materials with higher carrier density (up to about 10^{18} cm^{-3}) were found to give worst devices [69]. The analysis of QE curves of these solar cells revealed that the minority carrier diffusion length increases with decreasing acceptor concentration.

These results suggest that good quality CZTS thin films have to show sufficiently high resistivity, likely correlated to a low defect concentration. A lower limit for the material resistivity to obtain working devices seems to be 10 Ωcm, which, using a mobility of 5 $cm^2/(Vs)$, corresponds to a free carrier concentration of about $10^{17}cm^{-3}$.

2.3 Cu_2S-SnS_2-ZnS pseudo-ternary phase diagram: CZTS phase stability and spurious phases

Control of the phase stability is a central point for the development of high quality CZTS absorber layers. The representation of the Cu-Zn-Sn-S quaternary system is obviously quite complex since quaternary compounds would require a four dimensional diagram, and the temperature would also introduce an additional variable. This problem can be simplified by considering a pseudo-ternary phase diagram in which a perfect balance between metal and sulphur is assumed. This means that the amount of sulphur incorporated in the material is assumed to be only dependent on the amount of metals and on their valence: Cu(I), Zn(II) and Sn(IV).

A quasi-ternary system of practical interest for Cu_2ZnSnS_4 is Cu_2S–ZnS–SnS_2. The phase equilibria were investigated by Olekseyuk et al [109], who presented the phase diagram, reported in Figure 5, for the system at 400°C.

A very narrow stability region is expected for CZTS, which shows a Cu_2ZnSnS_4 single phase only within the small filled area at the centre of the diagram. Stoichiometry variations out of this region lead to the formation of additional secondary phases. Depending on the system composition, different secondary phases are expected and are shown in Figure 5, in the corresponding regions of the phase diagram. Cu_xS compounds can be expected for Cu-rich compositions, as well as for Sn- and Zn-poor stoichiometry. In this last region, Cu-Sn-S ternary phases are also expected. No stable ternary compound is expected to form neither between ZnS and SnS_2 nor between ZnS and Cu_2S. ZnS is expected as a single phase (alongside CZTS) for Zn-rich composition. For Cu-poor or Sn-rich samples, a second quaternary compound $Cu_2ZnSn_3S_8$ (discovered by Olekseyuk et al. in [109]) is also expected from the reaction of SnS_2 and CZTS at 700°C.

It has to be pointed out that, because of the previous assumption of a perfect balance between sulphur and metals, only secondary compounds with Cu(I), Zn(II) and Sn(IV) are taken into account in the Cu_2S-ZnS-SnS_2 system diagram, whereas those involving metals in different oxidation states (such as Cu_2SnS_4, Cu_3SnS_4 or Cu_4SnS_6) are not considered.

A wide list of possible spurious compounds (also detected either as reaction products during CZTS formation [128, 165] or as segregated phases in the final CZTS films [161, 38]) are reported in Table 4 [164, 68].

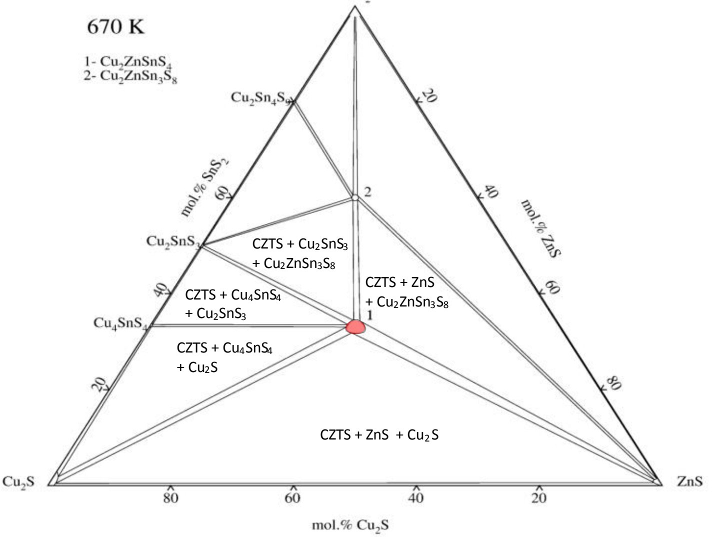

Figure 5: Isothermal section of the Cu_2S–ZnS–SnS_2 quasi-ternary system at 400°C [109]. Secondary phases expected in the different regions of the phase diagram are also reported.

Table 4: Secondary phases for the Cu-Zn-Sn-S system. For each material, the stability region, the crystal structure, the bandgap energy Eg and the XRD card are reported.

Chemical formula	Mineral	Stabiliy	Structure	E_g (eV)	XRD card
CuS	Covellite	$T < 507°C$	exagonal	1.7	06-0464 75-2233
Cu_2S	Low-Chalcocite	$0°C < T < 104°C$	orthorhombic	1.18 [96]	23-0961 73-1138

Chemical formula	Mineral	Stabiliy	Structure	E_g (eV)	XRD card
Cu_2S	High-Chalcocite	90°C < T < 435°C	exagonal		84-0206
Cu_9S_5	Digenite	72°C < T < 1130°C	rhombohedral	1.8 [87]	47-1748 84-1770
$Cu_{31}S_{16}$	Djurleite	T < 93°C	orthorhombic	1.4	42-0564 83-1463
Cu_7S_4	Anilite	T < 75°C	orthorhombic		72-0617
2H-ZnS	Wurtzite		exagonal	3.91	79-2204
ZnS	Sphalerite		cubic	3.54	05-0566 71-5975
α-SnS	Herzenbergite	T_{melt} < 605°C	orthorhombic	1.3 [123]	83-1758 (Amnm)
β-SnS		T_{melt} > 605°C			73-1859 (Pbnm)
Sn_2S_3	Ottemanite			1 [123]	75-2183
2H-SnS_2	Berndtite	T_{melt} = 870°C	exagonal	2.2 [123]	23-0677 83-1705
4H-SnS_2					21-1231
Cu_2SnS_3		T>400°C	Cubic	0.96 [37]	
Cu_2SnS_3		T<400°C	tetragonal	1.35 [37]	
Cu_3SnS_4	Isostanite		orthorhombic	1.60 [37]	36-0218
Cu_4SnS_6	Synthetic	T_{melt} <537°C	rhombohedral		36-0053
Cu_2ZnSnS_4	Kesterite		tetragonal	1.5	26-0575

2.3.1 Effect of secondary phases on CZTS absorber layer and solar cells

The control of secondary phase formation in CZTS is a critical issue to obtain high efficiency devices.

Cu-S and Cu-Sn-S compounds are detrimental for PV application of CZTS, being highly conductive phases [157, 107, 167], which can create shunting paths in the final devices. Cu_2SnS_3 (CTS) can form a solid solution with CZTS, lowering the Eg and increasing the conductivity of the final compound.

Cu_xS phases are often detected also in CIS alloys as a result of the Cu-rich compositions, usually adopted to enhance the grain growth [153]. In CIS, Cu_xS phases segregate on the surface and can be removed by KCN chemical treatment. The effect of Cu-rich composition on CZTS seems to be still controversial: similar to CIS, an improvement of crystallinity with the increase of copper-content in co-evaporated CZTS films grown is reported in [151], but opposite trends are observed in [29, 128, 149], for CZTS samples grown by sol-gel and electrochemical deposition. A trend opposite to CIS was also reported by Katagiri group [66] for CZTS films grown from co-sputtered precursors, where an improvement of CZTS morphology was observed for decreasing copper content. Similar to CIS, copper sulphides segregated on the CZTS top surface can be removed by KCN chemical treatment, but undesirable voids can result upon etching in case of dispersed or large Cu_xS/CTS segregations [35], [170]. Copper-poor and zinc-rich compositions are therefore desirable to suppress Cu-S detrimental phase formation and are usually adopted in the literature for realization of high efficiency CZTS devices [72, 160].

As a result of the Cu-poor and Zn-rich composition, ZnS phases are often detected in the final CZTS films. The effect of this phase on the final devices is not clear. Indeed, due to its quite high bandgap energy (3.54 eV), ZnS segregations can give insulator regions in the CZTS absorber layer, thus lowering the device performances. However, ZnS segregations have been often detected even in the best solar cells reported in the literature [74, 161], so that its role on the device performances seems to be not-harmful.

Tin sulphide phases can also result from Cu-poor (and Sn-rich) composition. Sn-S phases have been detected by in-situ XRD measurements as reaction products during CZTS formation [165, 128] and can also be found as segregated phases in the final CZTS films [34]. No detrimental effect of SnS_2 phases for PV performances has been reported. However, due to the quite high vapour pressure of SnS, tin losses due to SnS evaporation from CZTS films have been widely reported in the literature [42, 163, 134] and can be harmful (especially for vacuum-based processing) in terms of both stoichiometry control and CZTS phase stability [134].

2.3.2 Detecting secondary phases in CZTS

X-ray diffraction (XRD) and Raman Spectroscopy are generally used as complementary techniques to characterize CZTS samples.

$Cu_{2-x}S$ spurious phases, as well as Sn_xS_y compounds (SnS, SnS_2 and Sn_2S_3) can be easily identified by X-ray diffraction, showing diffraction peaks clearly distinct from those of CZTS. However, as shown in Figure 6 [159], ZnS and Cu_xSnS_{x-1} (CTS) phases are quite difficult (if not impossible) to be distinguished from CZTS phase.

Indeed, the most probable ZnS cubic phase show a crystal structure very similar to CZTS (having the same in-plane cell parameters and being the kesterite *c* parameter a multiple of the ZnS one). Therefore, ZnS diffraction pattern is superimposed to the CZTS one. Among CTS compounds, only the orthorhombic Cu_3SnS_4 phase can be detected in CZTS samples by XRD, whereas problems similar to ZnS are found for Cu_2SnS_3 compounds: because of their similar symmetry and lattice constant with CZTS, the diffraction peaks of both cubic and tetragonal Cu_2SnS_3 are superimposed to those of CZTS phase [38].

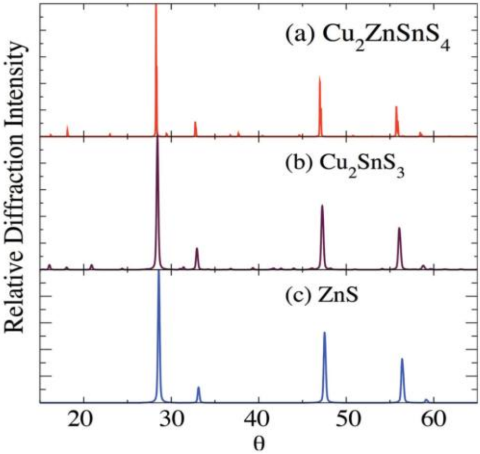

Figure 6: Overlapping of CZTS, Cu_2SnS_3 and ZnS XRD peaks [159].

Raman spectroscopy is an alternative means to distinguish possible secondary phases present in CZTS samples. It has to be noted, however, that with the typical laser excitation sources (∼300÷650 nm) used in Raman spectroscopy, the light penetration depth is in the order of hundred nanometers or less (the penetration depth can be roughly estimated as $1/(2\alpha)$, where α is the sample absorption coefficient) and therefore only the surface region of the samples can explored in planar configuration. In-depth analysis can be performed using the sample cross-section, or by measuring the Raman spectra while sputtering the sample to different depths.

A clear Raman spectrum of a Cu_2ZnSnS_4 sample (measured on a monograin powder) showing all the CZTS characteristic peaks is reported in [4] and it is shown here in Figure 7. A list of the Raman peaks of other phases of practical interest is reported in Table 5.

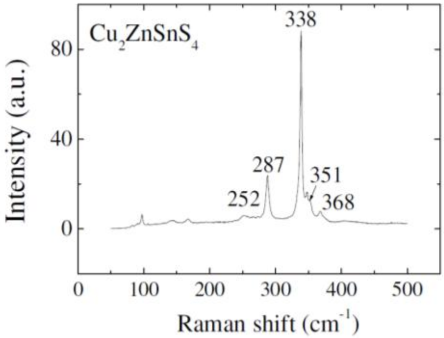

Figure 7: Typical Raman spectrum of a Cu_2ZnSnS_4 monograin powder [4].

Table 5: Reported Raman peaks of CZTS and related ternary and binary phases.

	Raman Shift (cm^{-1})	Reference
CZTS	338, 287, 351, 368, 257	[4, 34]
ZnS	352, 275	[106]
Cu_2SnS_3 (tetragonal)	337, 352, 297	[37, 36]
Cu_2SnS_3 (cubic)	303, 356	[37, 36]
Cu_3SnS_4	318, 295, 348	[37, 36]
$Cu_{2-x}S$	476	[34]
SnS	160, 190, 219	[86]
Sn_2S_3	307	[86]
SnS_2	215, 315	[86]

Looking at these data, it appears that the main vibrational peaks of ZnS and tetragonal Cu_2SnS_3 are very close to CZTS characteristic peaks. Using laser excitation in the red-energy region, a clear identification of these phases could be difficult, especially when only traces of ZnS and CTS coexist with CZTS. Quite recent works showed that unambiguous identification of ZnS (even when present only in small quantity) can be possible by using Raman spectroscopy with UV resonant excitation conditions (λ = 325 nm) [33].

Other experimental techniques can be useful to detect spurious phases in CZTS samples. EDX scans in STEM mode have been reported in the literature [161] and allowed identifying secondary phases present as segregated clusters both in the bulk and at the grain boundaries.

Chemical depth profiles (using several techniques such as EDX, XPS, SIMS and GDOES) can also be useful to detect spurious phases, which tend to be localized in particular region the sample. For example, ZnS segregations on the bottom of CZTS thin films are widely reported in the literature and can be clearly revealed by measuring the Zn-depth profile [139, 74].

Optical measurements can also be used to evaluate the presence of possible spurious phases. For example, conductive copper sulphide phases are expected to lower the sample transmittance and give a contribution to the optical absorption in the energy region below the CZTS bandgap. These phases, indeed, show a high absorption coefficient in the infrared region due to a high defect and free carrier density. A contribution in the infrared region is also expected when spurious phases with Eg lower than the CZTS bandgap (such as SnS, Sn_2S_3 and Cu_2SnS_3) are present in the sample.

Chapter III

CZTS thin films from stacked evaporated precursors

Part of this chapter has been published in:

C. Malerba, F. Biccari, C.L. Azanza Ricardo, M. Valentini, R. Chierchia, M. Müller, A. Santoni, E. Esposito, P. Mangiapane, P.Scardi and A.Mittiga

"CZTS stoichiometry effects on the band gap energy",
Journal of Alloys and Compounds, 582 (2014) 528-534

C. Malerba, C.L. Azanza Ricardo, M. Valentini, F. Biccari, M. Müller, L. Rebuffi, E. Esposito, P. Mangiapane, P.Scardi and A.Mittiga

"Stoichiometry Effect on CZTS Thin Films Morphological and Optical Properties",
Journal of Renewable and Sostainable Energy, 6 (2014) 011404.

3.1 Introduction

The present chapter concerns our investigations on CZTS thin films grown by sulphurization of stacked evaporated precursors deposited by electron beam evaporation. This method has been reported in the literature as a successful route to grow high quality CZTS thin films, giving devices with efficiency over 5% [69]. A description of the growth process and its optimization to obtain CZTS samples with good quality in terms of phase stability, composition control and homogeneity is presented in the first sections, whereas attention is then paid to investigations on the basic physical properties of the final materials. A detailed study of optical, microstructural and morphological properties of CZTS thin films is presented and the correlations with the material stoichiometry are discussed.

A deep knowledge of the material physical properties and their correlation with the growth conditions is a key point to improve the material quality as absorber layer, but a clear understanding of these issues still lacks. It is widely accepted that Zn-rich and Cu-poor compositions give the best results in terms of conversion efficiency of the final devices [71], but the role of the stoichiometry on the basic physical properties of CZTS has not yet been completely understood.

A large spread of energy gap values can be found in the literature, where values from 1.4 to 1.7 eV are reported [38, 73, 101, 150]. Even though this variability can partially depend on the extrapolation method used to derive the Eg value from the optical data, it appears that both composition and sulphurization/growth conditions influence the CZTS optical properties [70, 149, 150]. However, no clear trends have been yet univocally established [69, 144, 149] , thus making difficult to devise a suitable explanation for this variability.

Another issue of utmost importance and not completely understood is the influence of the material composition on the final morphology and microstructure. For example, the influence of the copper content on the grain growth is quite controversial: Tanaka et al. [151] report an improvement of the crystallinity of co-evaporated CZTS thin films with the increase of the copper content, in accordance with the results also obtained in CIGS [153] , whereas opposite trends are reported in other works [29, 149], where larger grains are found to form with the decreasing copper concentration in kesterite thin films obtained by sol-gel and electrochemical deposition.

Even though the microstructure is also influenced by the growth process, further investigations on the stoichiometry effects on the CZTS morphology are an important issue, since a material with large grains helps to get better device performances. Indeed, the grain boundaries typically introduce additional defects, which can act as recombination centres for the electron-hole pairs, reducing the cell efficiency. This problem should be particularly important in CZTS-based devices, since the grain boundary effect could be more detrimental than in chalcopyrites (CIGS) [82].

3.2 Growth method

CZTS thin films were grown by a two-step process. The first step is a vacuum deposition by electron beam evaporation of stacked precursors composed by multiple layers of ZnS, Cu and Sn. This step is followed by a heat treatment of precursors in a sulphur atmosphere (sulphurization), necessary to convert in initial stack into CZTS thin film. Soda lime glass (SLG) and molybdenum covered SLG were used as substrates, thus allowing characterization of the final materials both as isolated films (on insulator and transparent substrate) and as absorber layers in solar cells. The substrates are kept at 150°c during evaporation process, to allow a first interdiffusion of the metals into the starting stacks.

3.2.1 Precursor deposition by e-beam evaporation

Stacked layer precursors were deposited by using a Balzers BAK640 electron beam evaporator with a planetary sample holder. A picture of the vacuum chamber is reported in Figure 8.

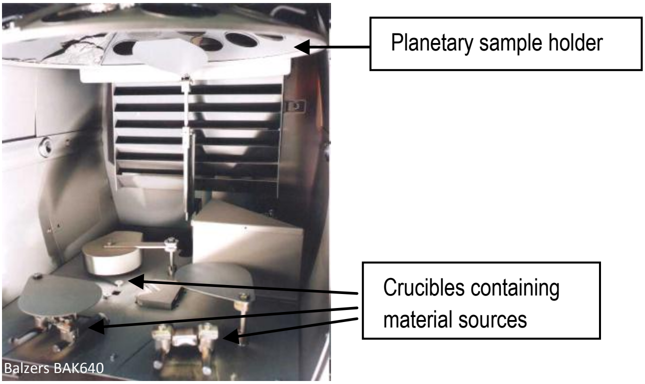

Figure 8: Balzers BAK640 electron-beam evaporator used for deposition of stacked layer precursors.

The system is equipped with a quartz balance, placed at the centre of the planetary, which allow controlling the amount of deposited material. However, the software which controls the system does not provide a direct measure of the deposited mass (m^b), but provides the thickness (d) of the evaporated film, obtained from the theoretical value of the material density (ρ, Table 6) and the value of the sensitive area (A) of the balance (i.e. the area of the balance surface exposed to the evaporation): $\mathrm{d} = \mathrm{m^b}/(\mathrm{A} \cdot \rho)$. In these systems, the thickness value is usually automatically corrected by using proper tooling factors (TF), which take into account possible difference between the thicknesses of the films deposited on the balance and on the substrate, mainly due to system geometry and sticking coefficient:

$$\mathrm{d} = \mathrm{TF} \cdot \mathrm{m^b}/(\rho \cdot \mathrm{A}) = \mathrm{TF} \cdot \mathrm{m_S^b}/\rho,$$

where $\mathrm{m_S^b}$ is the mass deposited on the quartz balance per unit area.

However, for a proper mass control, the real density of the evaporated material must be taken into account. Indeed, depending on the porosity of the evaporated film, its density could be different from the theoretical value expected for the corresponding bulk material, thus introducing an error in the mass to thickness conversion and therefore in the estimate of the amount of the evaporated material. Another source of error could be a possible temperature difference between substrate and balance.

In order to improve the accuracy in the mass control, we calibrated our deposition by using proper correction factor (F), obtained from the direct measure of the real mass evaporated on the substrate. To obtain the calibration factors, each layer was deposited by setting a nominal thickness (d), by simply fixing TF=1 and using the theoretical value for ρ. The real mass evaporated on the substrate per unit area $\left(\mathrm{m_S^{exp}}\right)$ in these conditions was then measured by a high precision balance (with accuracy of 10^{-6} g) and the calibration factor F was obtained by the simple equation:

$$\mathrm{d} \cdot \mathrm{F} = \mathrm{m_S^{exp}}$$

The molar mass (M, see Table 6) of each element was then used to convert the nominal thickness into the number of evaporated mol.

$$\mathrm{d} \cdot \bar{\mathrm{F}} = \frac{\mathrm{m_S^{exp}}}{\mathrm{M}}$$

To take into account the correct sticking coefficient, the calibration of each material was performed using the proper substrate, according to the structure chosen for the precursor stack. The typical stack order used in this work is SLG/ZnS/Sn/Cu and therefore a SLG was used to obtain calibration factor for ZnS, a ZnS covered SLG was used for the calibration of Sn and a Sn covered SLG was used to calibrate the Cu amount.

Multiple depositions were performed for each material, and each sample was weighed several times. In this way, calibration factors were obtained by a statistical analysis based on Gaussian distribution. The results are reported in Table 6, with the corresponding errors.

Table 6: Theoretical density, molar mass and calibration factors ($\bar{\mathbf{F}}$ and $\mathbf{F}$) for ZnS, Sn and Cu.

Material	Density (g/cm^3)	M (g/mol)	$\bar{\mathrm{F}}$ (nmol cm^{-2} nm^{-1})	F (µg cm^{-2} nm^{-1})
ZnS	4.09	97.47	2.42 ± 0.07	0.236 ± 0.007
Sn	7.31	118.71	4.25 ± 0.13	0.505 ± 0.015
Cu	8.94	63.55	8.98 ± 0.27	0.571 ± 0.017

3.2.2 Deposition of precursors with different compositions

Calibration factors obtained with the procedure described before were used to properly set the nominal thicknesses of the different layers into the starting stacks, in order to obtain precursors with the desired [Cu]:[Zn]:[Sn] metal proportions.

In this work, precursor composition was varied within the Cu-poor and Zn-rich stoichiometry region, which is known to give CZTS samples with the best performances as absorber layer [71].

All the precursors were prepared keeping fixed the copper amount, and the metal proportions were varied by changing the thicknesses of both ZnS and Sn layers into the starting stacks.

First experiments were performed by changing the zinc amount, varying the [Cu]:[Zn] ratio from 2:1 to 2:1:48, while keeping fixed at 2:1.18 the nominal [Cu]:[Sn] ratio (see Table 7). The total nominal thickness of ZnS, Sn and Cu in these precursors is reported in Table 7, where an integer number, increasing from 1 to 4, is used to indicate the increasing Zn content.

Table 7: Total nominal thicknesses of ZnS, Sn and Cu and corresponding metal ratios in precursors with increasing zinc content (labelled with increasing integer numbers).

Composition Type	ZnS (nm)	Sn(nm)	Cu(nm)	[Cu]:[Zn]:[Sn]
#1	440	300	240	2 : 1.00 : 1.18
#2	500	300	240	2 : 1.12 : 1.18
#3	560	300	240	2 : 1.26 : 1.18
#4	660	300	240	2 : 1.48 : 1.18

CZTS samples obtained from these materials were characterized both as isolated films and as absorber layer in the final devices. Despite the large excess of zinc content, CZTS thin films produced from #4-type precursors showed the best performances as absorber layers.

For this reason, additional samples were prepared keeping fixed at 2:1.48 the [Cu]:[Zn] nominal ratio (corresponding to #4-type precursors), and changing the nominal Sn amount from [Cu]:[Sn] = 2:1.06 to [Cu]:[Sn] = 2:1.31. The total nominal thicknesses of ZnS, Sn and Cu in these precursors are reported in Table 2, where the labels #4(-), #4(0) and #4(+) are used to indicate the increasing tin content.

Table 8: Total nominal thicknesses of ZnS, Sn and Cu and corresponding metal ratios in #4-type precursors, with increasing Sn content (labelled as #4(-), #4(0), #4(+)).

Composition Type	ZnS (nm)	Sn(nm)	Cu(nm)	[Cu]:[Zn]:[Sn]
#4(-)	660	268	240	2 : 1.48 : 1.06
#4(0)	660	300	240	2 : 1.48 : 1.18
#4(+)	660	332	240	2 : 1.48 : 1.31

3.2.3 Conversion of precursors into CZTS by sulphurization treatment in tubular furnace

Stacked precursors were converted into CZTS thin films by a heat treatment in sulphur atmosphere. Sulphurization treatment is performed at 550°C in a tubular furnace fluxed with nitrogen, using a small not-sealed glass sulphurization chamber (with volume of about 50 cm^3) where precursors are placed together with a stoichiometric excess of sulphur powder (180 mg). Temperature (controlled by a thermocouple, labelled as tc in Figure 9) is raised with a heating ramp of 20°C/min from room temperature to 550°C and maintained at this temperature for 1 hour, as shown by the temperature profile in Figure 10. The heaters are then turned off and samples naturally cool down to room temperature under nitrogen flux. A scheme of the sulphurization system is depicted in Figure 9.

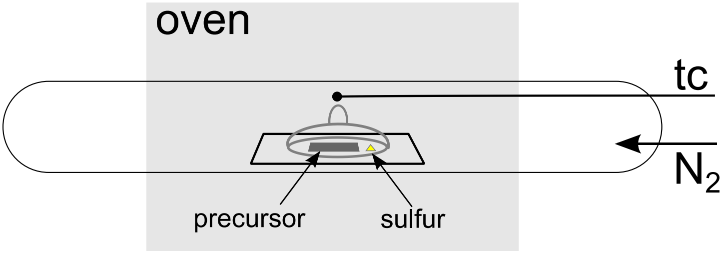

Figure 9: Scheme of tubular furnace and sulphurization chamber used for precursors conversion into CZTS thin films.

Experiments performed without using the closed glass reaction chamber, i.e. putting both precursors and sulphur directly into the N_2 flux ("open-volume"), were found to give highly conductive samples, with a high optical absorption in the infrared region. These properties are typical of Cu-rich CZTS films containing copper sulphides spurious phases (Cu_xS_y or Cu_2SnS_3) and suggest a non-controlled stoichiometry, likely due to spurious phase evaporation. Losses of Zn and Sn during the heat treatment are a widely reported problem in the literature [69, 163, 118] and may explain the results obtained by using sulphurization treatments in "open-volume" condition.

The use of small closed reaction chamber was found to prevent these losses, allowing a good control of sample stoichiometry, with better results in terms of reproducibility. Closed-volume sulphurization treatment was therefore chosen as the standard process in this work to convert precursors into CZTS films.

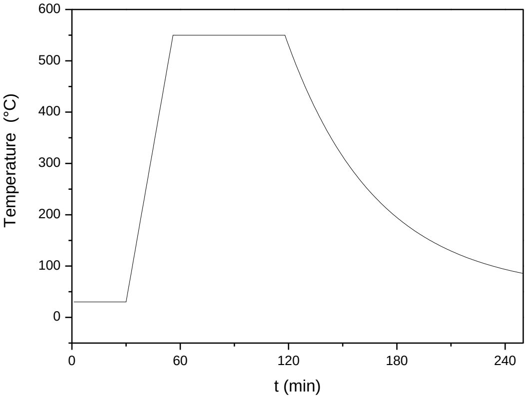

Figure 10: Temperature profile used for sulphurization treatment in tubular furnace.

3.3 Precursor structure

Precursors used in this work are multilayer structures made of ZnS, Cu and Sn. The choice of ZnS instead of metallic zinc was firstly forced by the high vapour pressure of the pure element, which makes it very difficult to be handled in high vacuum system. Secondly, the use of ZnS may have the advantage that a certain amount of sulphur is already present the staring stack and this may help the formation reaction of CZTS film during the sulphurization treatment. Moreover, the volume increase of material during precursor transformation into kesterite phase is smaller when part of the sulphur is incorporated into the starting stack. It was reported [69] that this fact could reduce possible stress effects resulting from film expansion, with better results in terms of film adhesion properties.

ZnS was deposited as the first layer of the stack. Tin and copper were then sequentially evaporated in two adjacent layers. This allows enhancing the metal interdiffusion into the starting stack, as Cu and Sn, at 150°C, can easily react to form Cu_xSn_y alloys.

XRD spectrum of a typical ZnS/Sn/Cu stack, reported in **Figure 11**, confirms the formation of Cu-Sn compounds, detected as Cu_6Sn_5 and Cu_3Sn, during precursor deposition.

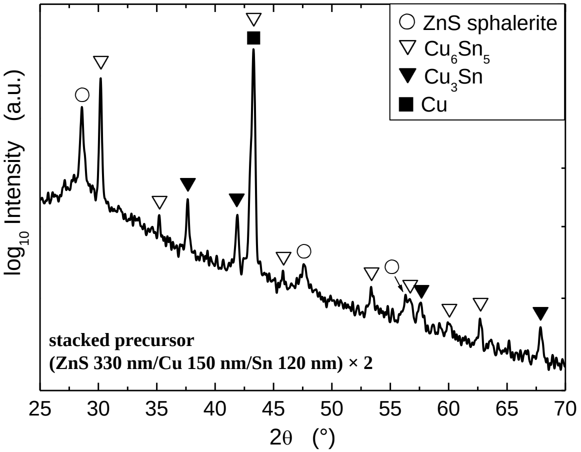

Figure 11: XRD spectrum (measured in θ-2θ configuration) of a typical precursor made by multiple repetition of the stack ZnS/Sn/Cu.

Some preliminary tests were performed by changing the order and the repetition of the different layers into the starting stacks, to improve the morphology and the chemical homogeneity of the final CZTS films. As also reported in the literature, the morphology of ZnS/Cu/Sn precursors was found to be improved respect to ZnS/Sn/Cu stack, obtained by simply changing the order of Cu and Sn into the starting stack. However, no significant morphological variation was revealed in the final materials (upon sulphurization). The ZnS/Sn/Cu stack order was finally preferred to prevent possible Sn losses [163, 118] and to avoid the formation of possible voids due to Cu migration to top-surface during the sulphurization treatment, as a result of the high Cu mobility respect to the other metals [35].

Multi-period structures are desirable to improve the metal mixing in the starting precursors [69]. The first experiments were therefore performed using precursors with the structure SLG/ZnS/Sn/Cu/ZnS/Sn/Cu, that is referred to as B-type structure. However, investigation by Secondary Ions Mass Spectroscopy (SIMS) on CZTS films produced from these stacks revealed a very poor homogeneity of the final materials.

The Zn-depth profile measured on a typical Zn-rich CZTS sample obtained from B-type precursors is reported in Figure 12. The large excess of Zn detected at the bottom of the film suggests a residual un-reacted ZnS phase at the glass interface, also visible in the SEM cross section shown in the inset of the same figure.

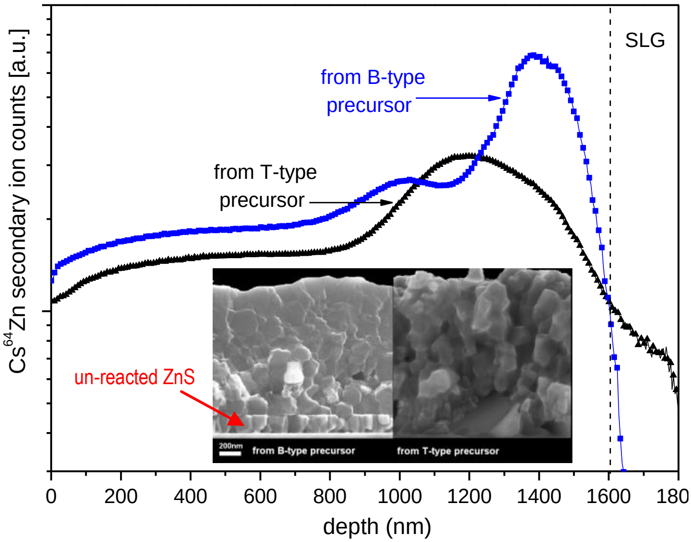

Figure 12: Zn depth profiles measured by SIMS in two CZTS samples grown from B-type and T-type precursors with the same nominal (Zn-rich) composition. The corresponding cross sections are reported in the inset. A residual un-reacted ZnS layer can be detected at the bottom of CZTS film obtained from the B-type stack.

In order to improve the film homogeneity, precursors were produced according to a new structure, that we named T-type, in which the first ZnS layer is only 100nm thick and the remaining ZnS amount is distributed in other two layers: ZnS(100nm)/Sn/Cu/ZnS/Sn/Cu/ZnS (see Table 9). A scheme of the layer distribution into the B- and T-type stacks is reported in Figure 13.

Table 9: Distribution of ZnS, Sn and Cu layers in stacked precursors with different structures, named as B- and T-type.

Precursor Type	Structure
B-type	Substrate/ZnS/Sn/Cu/ZnS/Sn/Cu
T-type	Substrate/ZnS(100nm)/Sn/Cu/ZnS/Sn/Cu/ZnS

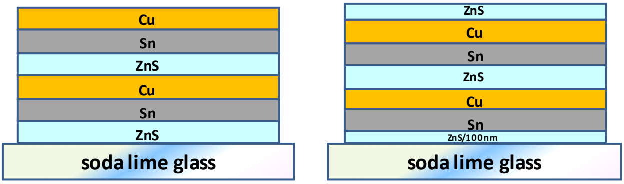

Figure 13: Distribution of ZnS, Sn and Cu layer into B-type (left) and T-type (right) stacks.

The Zn depth profiles measured by SIMS in two CZTS films obtained from a B-type and T-type precursors with the same nominal (Zn-rich) composition are compared in Figure 12. The Zn excess detected at the bottom of CZTS film obtained from the T-type precursor is lower compared to the sample grown from B-type stack, thus revealing a better metal mixing in samples obtained from T-type precursors.
After these analyses, CZTS samples were grown using T-type structures and the work presented here refers to materials produced after this optimization of precursor.

Concerning the sample inhomogeneity discussed before, it has to be pointed out that the ZnS segregation is due to the intentional Zn-rich composition of the starting precursors. The depth profiles shown in Figure 14 show that the Zn-enrichment can be controlled (and reduced) by lowering the ZnS amount in the starting stack.

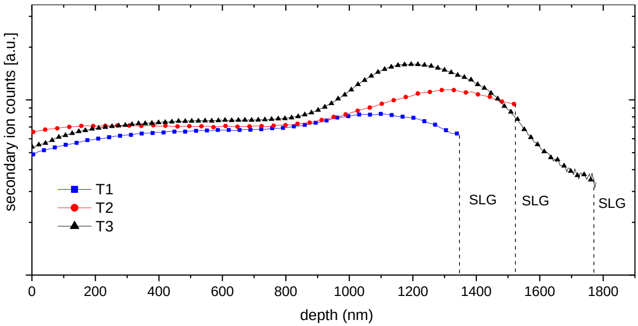

Figure 14: SIMS depth profiles measured in CZTS thin films, obtained from T-type precursors with decreasing Zn content (composition type #1, #2, #3 of Table 7).

However, despite the sample inhomogeneity, CZTS films with higher zinc content showed better performances as absorber layer. Therefore, as discussed in paragraph 3.2.2, part of the investigation on our materials were intentionally performed using Zn-rich sample (see Table 2).

3.4 Stoichiometry effect on CZTS optical properties and microstructure

To investigate the effect of different stoichiometries on CZTS basic physical properties, two series of samples were prepared by varying the composition of the starting precursors. A first set of samples (A-series) was prepared keeping fixed the total amount of copper and zinc ([Cu]:[Zn] = 2:1.48), while the total amount of evaporated tin was varied from [Cu]:[Sn] = 2:1.06 to [Cu]:[Sn] = 2:1.31 (see Table 10). A second set of samples (B-series) was instead prepared by changing the nominal zinc content from [Cu]:[Zn] = 2:1 to [Cu]:[Zn] = 2:1.48 (see Table 11), while keeping fixed the total amount of both copper and tin ([Cu]:[Sn] = 2:1.18). All the CZTS samples were prepared using precursors with T-type structure, by varying the total amount of the evaporated species (ZnS, Sn and Cu) as reported in Table 7 and Table 2.

Table 10: Nominal metal proportions in the precursors of A-series samples and CZTS composition measured by EDX (normalized to total metal amount equal to 4). Values of E04 (energy at which $\alpha=10^4 cm^{-1}$) and CZTS film thickness, d (with a standard deviation of about 70 nm), are also reported.

A sample series	Precursors [Cu]:[Zn]:[Sn]	CZTS [Cu]:[Zn]:[Sn]:[S]	E04 (eV)	d (nm)
K241a	2 : 1.48 : 1.06	1.59:1.57:0.84:4	1.48	1580
K252a2	2 : 1.48 : 1.06	1.63:1.47:0.90:4	1.49	1650
K253a	2 : 1.48 : 1.06	1.63:1.47:0.90:4	1.48	1610
K258a2	2 : 1.48 : 1.06	1.61:1.51:0.88:4	1.48	1590
K256a	2 : 1.48 : 1.18	1.74:1.26:0.99:4	1.63	1675
K255a2	2 : 1.48 : 1.18	1.76:1.24:1.00:4	1.60	1660
K250a2	2 : 1.48 : 1.18	1.71:1.31:0.98:4	1.63	1680
K250a	2 : 1.48 : 1.18	1.73:1.27:1.00:4	1.63	1670
K251a	2 : 1.48 : 1.31	1.79:1.18:1.03:4	1.63	1770
K251a2	2 : 1.48 : 1.31	1.75:1.21:1.03:4	1.62	1795

Table 11: Nominal metal proportions in the precursors of the B-series samples, with different zinc content. Values of E04 (energy at which $\alpha=10^4 cm^{-1}$) and CZTS film thickness, d (with a standard deviation of about 70 nm), are also reported.

B sample series	Precursors [Cu]:[Zn]:[Sn]	E04 (eV)	d (nm)
K239a	2 : 1.00 : 1.18	1.616	1400
K237a	2 : 1.12 : 1.18	1.605	1450
K237a2	2 : 1.12 : 1.18	1.605	1450
K235a	2 : 1.26 : 1.18	1.610	1550
K235a2	2 : 1.26 : 1.18	1.607	1560
K234a	2 : 1.48 : 1.18	1.608	1650
K234a2	2 : 1.48 : 1.18	1.613	1650

3.4.1 Samples characterization techniques

Chemical analysis of CZTS films obtained after the precursor sulphurization was performed using Energy Dispersive X-Ray spectroscopy (EDX) and X-Ray Photoelectron Spectroscopy (XPS), used to evaluate the element distribution along the film thickness. XPS data were acquired in an ultra-high vacuum system equipped with a VG Al Kα monochromatized X-ray source and a CLAM2 hemispherical analyser. The depth profiling was performed using a mild sputtering with 1 keV Ar ion energy [124]. Element concentrations were calculated from the area of the background-subtracted core level peaks, taking into account three different corrections: the CLAM2 analyzer transmission function [121], the Scofield cross-section [19] [129] (corrected for the angular asymmetry [119]) and the electron mean free path [135].

Microstructural characterization was performed using both micro-Raman and XRD diffraction measurements. Raman spectra were acquired in back scattering configuration, using a custom system based on a 0.75 m Acton single monochromator (Princeton Instruments) with a 1200 grooves/mm grating and an objective 50(Olympus). A Nd:vanadate laser (Verdi, Coherent) with a wavelength of 532 nm was used as excitation source.
XRD data were collected by using both Cu-Kα (with a high-resolution Rigaku PMH-VH diffractometer in Bragg-Brentano configuration) and Synchrotron Radiation measurements (SRXRD), performed at the MCX beamline at the Italian Synchrotron ELETTRA-Trieste with a 15 keV radiation energy. In the latter, flat-plate configuration was used, after a careful optimization of the optical set-up to produce a narrow and symmetrical instrumental line profile, thus extending the limits of line profile analysis

with respect to the conventional laboratory measurements. XRD profiles were analyzed using both Rietveld [13] and Whole Powder Pattern Modelling (WPPM) [80] approach, in order to extract as much information as possible from the performed measurements. The former is used in order to estimate the amount of spurious phases (mainly detected as Sn_xS_y) as well as for the estimation of the Sn-site occupancy in the CZTS phase. This parameter is very useful because it is only related to the CZTS phase microstructure and it is not affected by possible spurious phases or sample inhomogeneity, which, instead, can affect the EDX chemical results (see paragraph 3.4.2). Furthermore, WPPM provides a detailed understanding of the sample microstructure through a data analysis entirely based on physical models of the present phases (instead of using, arbitrary, a-priori chosen profile function as in Rietveld analysis), thus allowing the determination of microstructural parameters such as the crystalline domain size distribution.

Optical properties were investigated by transmittance measurements in the 250–2500 nm wavelength range, using a spectrophotometer Perkin Elmer Lambda9, equipped with an integrating sphere. Photothermal Deflection Spectroscopy (PDS) was used to obtain more accurate absorption data in the subgap region. The measurements were performed using a TESTCEL automated spectrometer equipped with a Xe and an Ha lamp, thus covering a wide wavelength range (250–1770 nm). CCl_4 was used as deflecting medium.

3.4.2 Chemical characterization

The results of the EDX measurements performed on the samples of the A-series are reported in Table 10. The measured tin content shows a fairly good linear correlation with the nominal tin amount in the starting precursor. This correlation is shown in Figure 15, where the deviation of the tin stoichiometric coefficient (defined as x_{Sn}= 4[Sn]/([Cu]+[Sn]+[Zn])) evaluated by EDX in the CZTS films is plotted against the same nominal quantity expected in the precursors. A similar dependence was found for the sample thicknesses, which vary from about 1400 to 1800 nm according to the Sn and ZnS thickness used for the corresponding precursors, thus demonstrating a good control of the growth process.

Figure 16 depicts that, as the tin content increases, the zinc concentration exhibits an exaggerated decrease and the copper concentration even shows an anomalous increase.

This behaviour is not representative of the real compositional changes, but can be explained looking at the results of XPS analysis showed in Figure 17. Depth profiles reveal the presence of a Zn-rich layer at the bottom of the films, likely due to ZnS segregations at the CZTS/substrate interface, which probably are also related to the small-grain-size interfacial region visible in the sample SEM cross section (see Figure 18).

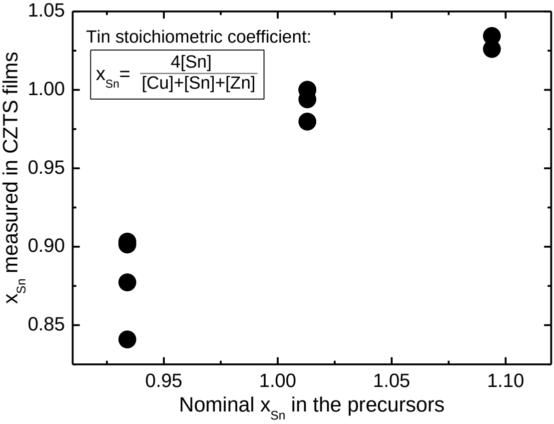

Figure 15: Correlation between the nominal tin stoichiometric coefficient (xSn) in the precursors and the same quantity measured by EDX in the A-series samples. The scattering of the data is related to the reproducibility of the evaporation process and to experimental errors of the microanalysis.

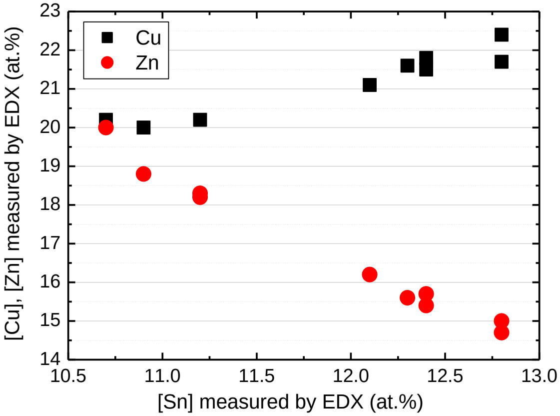

Figure 16: Results of EDX measurements on the A-series CZTS samples.

This ZnS segregation can affect the EDX results. Indeed, in an EDX measurement, the excitation rate induced by the electron beam steeply decays below the sample surface; therefore the measured Zn concentration decreases as the film thickness increases, thus resulting in a fictitious increase of the other elements.

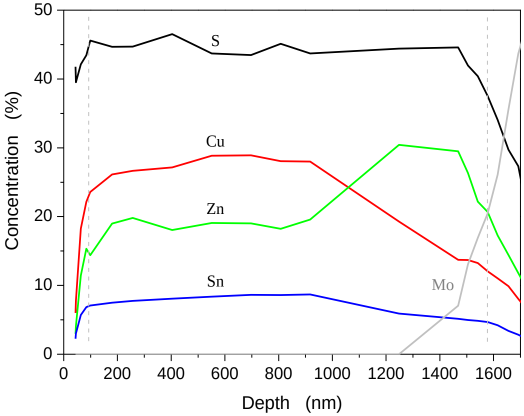

Figure 17: Element depth profiles obtained from XPS measurements.

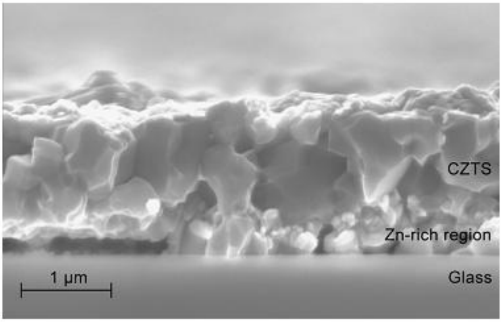

Figure 18: SEM micrograph of a CZTS film grown from stacked evaporated precursor. The interfacial region with small-grain-size is likely related to a ZnS phase-segregation.

This explanation is also confirmed by EDX Monte Carlo simulations, performed with the software Casino [28]. For the simulations, a CZTS/ZnS/glass structure was considered and a stoichiometric concentration was assumed for the CZTS phase. The ZnS thickness was fixed at 500 nm, while the thickness of CZTS was varied from 500 to 2500 nm. These parameters were chosen to amplify the effect of the inhomogeneity in our samples. The obtained trend of the cation concentrations is reported in Figure 19. The results of simulations show that, as expected, for sufficiently thick CZTS samples, the EDX measurements are not affected by the presence of the ZnS layer and provide the correct stoichiometric composition. On the contrary, as the CZTS thickness is reduced, the EDX absolute values are altered by the ZnS segregation and the metal concentrations show a fictitious variation, in agreement with the experimental data reported in Figure 16.

However, as [Sn] and [Cu] are altered in a similar way, their ratio is a reliable quantity to express the stoichiometry variation in our samples.

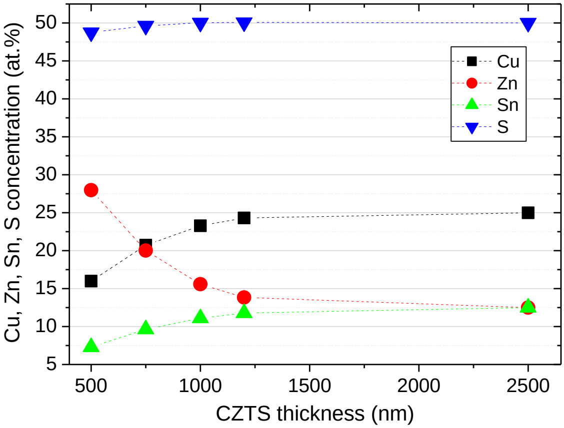

Figure 19: Simulation of EDX compositional variation which would be obtained in samples with structure (stoichiometric-CZTS/ ZnS/glass) for different CZTS thicknesses. The ZnS film thickness used in the simulations is fixed at 500 nm.

Detailed characterization of CZTS films by EDX was performed only on the A-series samples. Indeed, as shown in the next sections, the tin content is the most interesting parameter in terms of optical properties variability. On the contrary, the Zn content seems not to be a critical parameter and therefore B-series samples were qualitatively analyzed, taking into account only the nominal metal proportions in the starting precursors.

3.4.3 Control of CZTS phase stability by Raman spectroscopy and XRD measurements

Structural characterization was performed on both A and B-series samples using Raman Spectroscopy and XRD measurements with Cu2Kα radiation.

In Figure 20 a typical Raman spectrum of a CZTS film (sample K255a as an example) is reported. With the 532 nm laser excitation source, only the first hundred nanometers can be explored (the penetration depth can be roughly estimated as $1/(2\alpha)$). The measurements reveal a good quality of the surface region of the material, as no evident signals of other spurious phases (such as $Cu_{2-x}S$, $Cu_xSn_yS_z$ and Sn_xS_y) are detected. It is worth noting that, with the 532 nm excitation source, the ZnS phase cannot be easily detected with Raman Spectroscopy [41, 40] and even the XRD is not able to distinguish this phase from the CZTS one. However, because of the Zn-rich composition of the precursors, a ZnS phase segregation is expected and confirmed by XPS measurements reported before (Figure 17). This phase could be compatible with the small shoulder visible at about 350cm^{-1}, as a Raman shift of 348 cm^{-1} is expected from ZnS [34].

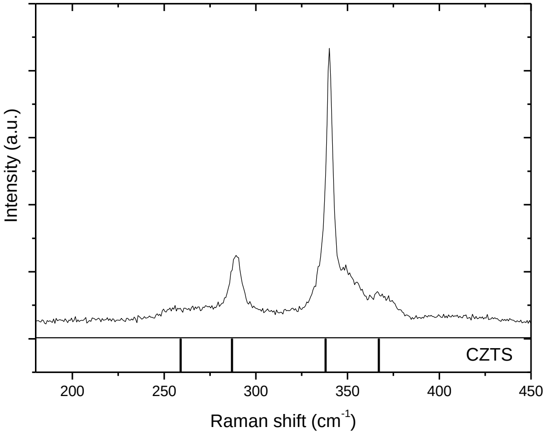

Figure 20: Raman spectrum of the sample K255a and reference peaks [4, 34].

Three typical XRD profiles measured on CZTS films with different Sn content (A samples) are reported in Figure 21. As the tin content increases, the corresponding XRD pattern shows peaks of Sn_xS_y secondary phases.

Although the strong preferred orientation of the tin sulphides phases gives quite intense reflections, the Quantitative Phase Analysis (QPA), performed with the

Rietveld approach [13], shows that the total amount of spurious phases is less than 1% (except for the most Sn-rich sample, where it reaches 2.5%).

XRD patterns of the B-series samples (not shown here) reveals a quite pure CZTS phase, with only traces of SnS_2 (about 0.5% or less), most likely as a consequence of the slightly Sn-rich composition of the precursors (see Table 11).

This result is in accordance with Raman spectra which confirmed CZTS as the main phase in the films, giving no evidence of other detectable spurious compounds [40]. Details of the fit procedure used to model the XRD profiles are described in paragraph 3.4.7, where Rietveld approach is used for a detailed study of microstructural properties of CZTS thin films with different tin content.

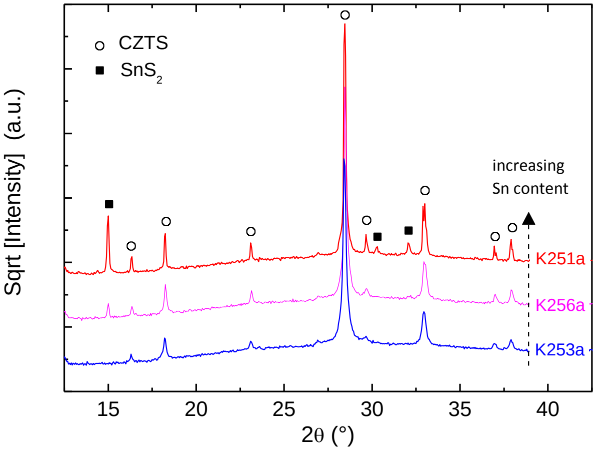

Figure 21: XRD spectra of three CZTS films with different Sn content.

Optical properties

3.4.4 Stoichiometry effect on the band gap energy

The optical properties of the samples were investigated by spectrophotometric measurements. The transmittance spectra of B-series samples did not show any relevant difference with the increase of Zn concentration. On the contrary, the transmittance of the films obtained by changing the Sn content (A-series) shows a shift toward lower wavelengths as the Sn content increases. This behaviour is shown in Figure 22. Taking into account multiple reflections inside the film and neglecting, as a first-order approximation, those inside the glass substrate, it is possible to calculate the absorption coefficient (α) starting from the transmittance data, using the equation:

$$T_f = \frac{(1 - R_{fa})\,(1 - R_{fs})x}{1 - R_{fs}R_{fa}x^2} \tag{1}$$

where $x = e^{-\alpha d}$, *d* is the thickness of the film and R_{fa} and R_{fs} are the reflectivity of the film/air and film/substrate interface respectively, calculated as:

$$R_{fa} = \left|\frac{n_{air} - n_{CZTS}}{n_{air} + n_{CZTS}}\right|^2 \ ; \ R_{fs} = \left|\frac{n_{SLG} - n_{CZTS}}{n_{SLG} + n_{CZTS}}\right|^2$$

assuming constant refractive indexes: n(SLG) = 1.5, n(air) = 1, n(CZTS) = 2.4. The value of the CZTS refractive index can be obtained by the Swanepoel approach [146], when interference fringes are clearly visible. The analysis provides a refractive index weakly dependent on λ in the subgap energy region, with an average value of 2.4. Since in many cases the fringes are not visible, as a first approximation we used n=2.4 for all the samples.

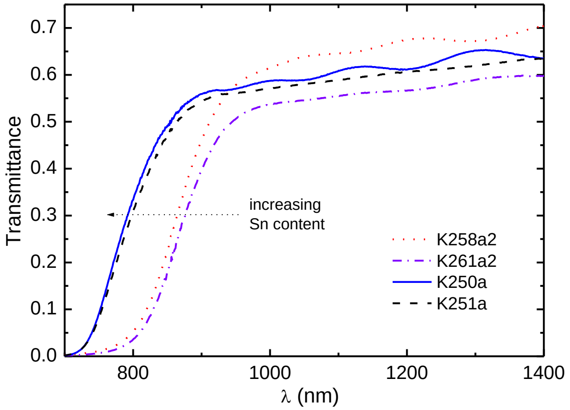

Figure 22: Transmittance spectra of CZTS samples with different Sn content.

The results are plotted in Figure 23a and Figure 23b (for the samples of A- and B-series, respectively) as $(\alpha E)^2$ versus E. This is the typical way to represent α(E) for direct-band semiconductors, since the value of the energy gap should be obtained from a linear fit of these curves. However, Figure 23 clearly shows that in polycrystalline thin films, because of the combined effects of interference and sub-gap absorption, an energy region with a clear linear dependence cannot be identified. Therefore, the Eg value strongly depends on the region chosen for the fit. To avoid any possible subjectivity in the band-gap value determination we decided to use E04 (i.e. the photon energy at which $\alpha=10^4 cm^{-1}$) as a more representative parameter than the value of Eg estimated by the graphical method.

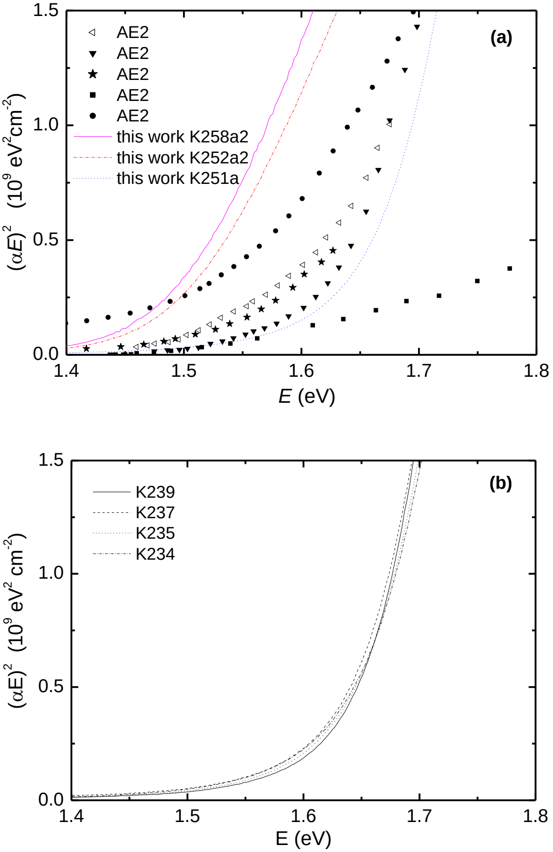

Figure 23: $(aE)^2$ versus E for different CZTS films with different Sn content (A series, panel a) and different Zn content (B series, panel b). In the panel a, some literature data are also reported for comparison.

The values of E04 obtained for the A and B series are listed in Table 10 and Table 11, respectively. In samples produced by changing the Sn amount in the starting precursor (A series), the energy gap varies of about 150 meV, from 1.48 to 1.63 eV, in accordance with the literature. In Figure 24, this variation is expressed as a function of the [Sn]/[Cu] ratio resulting from EDX measurements, since this is the experimental quantity less affected by ZnS segregation effects (see paragraph 3.4.2). The E04 shows a clear dependence on the [Sn]/[Cu] ratio, increasing steeply from the low to the high Eg value in response to a variation of few percent of [Sn]/[Cu]. Conversely, in the samples of B-series, an almost constant value of about 1.61 eV is found. This result can be reasonably explained by looking at the [Sn]/[Cu] ratio used for the precursors, which corresponds to the high E04 region in Figure 24.

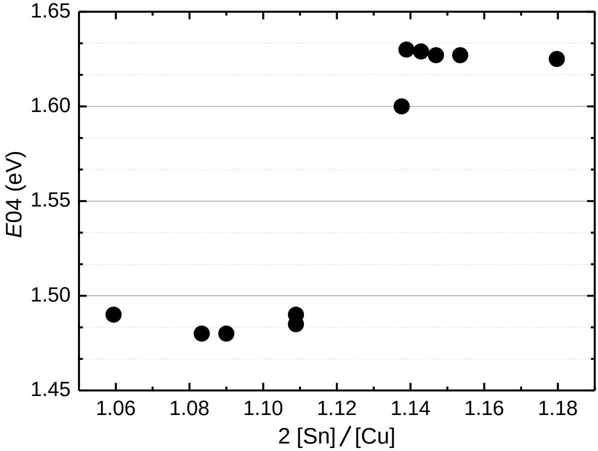

Figure 24: Variation of the E04 of CZTS films with increasing Sn content.

3.4.5 Defect induced bandgap shrinkage?

Different hypotheses can be put forward to explain the variability of the optical properties of CZTS thin films presented in this chapter.

- *Hypothesis of polymorphic transformation*

A first speculation advanced in the literature [131] is that the E_g variation could be attributed to stannite/kesterite polymorphic transformations. Indeed, theoretical works [114] predict a bandgap difference of about 140 meV between these two polymorphs (1.56 and 1.42 eV for kesterite and stannite respectively), in fairly good agreement with the E_g variability observed in these experiments. So far this hypothesis could not be proved, as with the most common experimental techniques (such as XRD) it is quite difficult to distinguish the different polymorphic structures. However, it is not clear how such a polymorphic transformation could be connected to the tin content variation. Moreover, we want to point out that, despite the difficulty to distinguish between kesterite polymorphic phases, the analisys of XRD peaks relative intensities performed on our samples gave no evidence for the formation of the stannite phase.

- *Hypothesis of solid solutions*

Another mechanism often proposed in the literature to explain the Eg variation is the existence of solid solutions between CZTS and secondary phases. In the case of CZTSe, CZTSe/ZnSe mixing was proposed as a possible explanation for the E_g increase [3]. However, the experiments performed in this work on the B-series samples show that the optical properties variability observed in CZTS cannot be imputed to the presence of a ZnS phase.

On the contrary, tin-rich spurious phases could be taken into account. In accordance with the XRD results, a first candidate could be SnS_2, which has an energy gap of about 2.2 eV. However, the formation of a CZTS/SnS_2 solid solution has to be excluded because of their completely different lattice structures. A solid solution with SnS (which has an Eg of 1.3 eV) would give rise to a E_g decrease, contrary to the experiments. Another possible Sn-rich spurious phase is $Cu_2ZnSn_3S_8$ [109]. It was proposed [131] that it could form a solid solution with CZTS changing the E_g of the material. Unfortunately, the current lack of both optical and structural information on $Cu_2ZnSn_3S_8$ does not allow proving this hypothesis. Finally, we want to point out that any mechanism based on the formation of solid solutions would not be able to explain the step-like behavior of the E_g, since a more gradual energy gap variation would be expected.

- *Hypothesis of defect-induced band gap shrinkage*

A mechanism, which instead could easily account for the step-like behavior of the E_g, is a defect-induced band gap shrinkage. Indeed, a reduced tin content could introduce a large density of acceptor defects (such as V_{Sn}, Cu_{Sn} and Zn_{Sn} anti-sites), thus changing the absorption edge of the material. In this case, the gap of stoichiometric kesterite should be about 1.62 eV and it would be apparently reduced by the formation of an acceptor band near the valence band. The amount of the E_g reduction would be therefore directly related to the acceptor band energy position.

Ab-initio calculations [17] suggest that V_{Sn}, Cu_{Sn} and Zn_{Sn} introduce shallow acceptor levels (at less than 0.2 eV from the VBM) which could explain the change in the absorption edge of the material. In addition to simple point defects, other defect complexes could be involved in the band gap shrinkage. Theoretical works [18] predict a band gap decrease due to the complex $2Cu_{Zn}$ + Sn_{Zn}, while the similar Cu_{Zn} + Sn_{Zn} complex introduces a donor level only. The variation of the [Cu]/[Sn] ratio explored in this work could influence the relative concentration of these two complexes, thus changing the energy gap. This theoretical model nicely fits with both the E_g shrinkage and the less evident increase of defect density at low Zn concentration (see Figure 25b, later on).
The experiments performed in this work do not allow identifying the nature of the involved defects. Nonetheless, the same calculations [18, 17]show that the formation energy of these defects depend on the material stoichiometry, but for Zn-rich material it is less than 0.6 eV, except for V_{Sn} which has an higher value (1.8 eV). According to these calculations, the involvement of this last defect is therefore less likely.

3.4.6 Stoichiometry effect on sub-gap optical absorption: investigation on intrinsic defect density

To investigate a possible correlation between bandgap energy and intrinsic defect density, Photothermal Deflection Spectroscopy measurements have been performed to obtain further information on the absorption coefficient at energies below Eg.
Actually the data obtained using this technique ($APDS$) are proportional to the sample absorptance (A) and must be rescaled to the absolute absorptance obtained from the spectrophotometric data. Within the same assumption used for the Eq.(1), the absolute absorptance A can be calculated using the equation:

$$A = 1 - R_f - \frac{(1-R_{fl})x}{1-R_{fl}R_{fs}x^2}\left[(1-R_{fl})R_{fs}x + 1 - R_{fs}\right],$$

where $x = e^{-\alpha d}$ and R_{fs} and R_{fl} are the reflectivity of the film/glass and film/liquid (CCl4 in our experiment) interfaces, respectively (with n(CCl_4) = 1.46). $APDS$ is then rescaled to match A in the energy region around Eg and $\alpha(E)$ is calculated from:

$$e^{-\alpha d} = \frac{-(1-R_{fl})(1-R_{fs}) + \sqrt{(1-R_{fl})^2(1-R_{fs})^2 - 4R_{fs}(1-R_{fl}-APDS\cdot R_{fs})(APDS+R_{fl}-1)}}{2R_{fs}(1-R_{fl}-APDS\cdot R_{fs})}.$$

The resulting absorption coefficients are reported in Figure 25. A clear increase of the sub-gap absorption coefficient is observed in the A-series samples, with a variation up to two orders of magnitude (from about 10 to 10^3 cm^{-1}) as the tin content is decreased. This result suggests a higher defect density in CZTS film with lower tin content, in accordance with the defect-based mechanism proposed before to explain the Eg variability. On the contrary, the increase in the Zn concentration causes only a slight reduction of α in the same energy region.

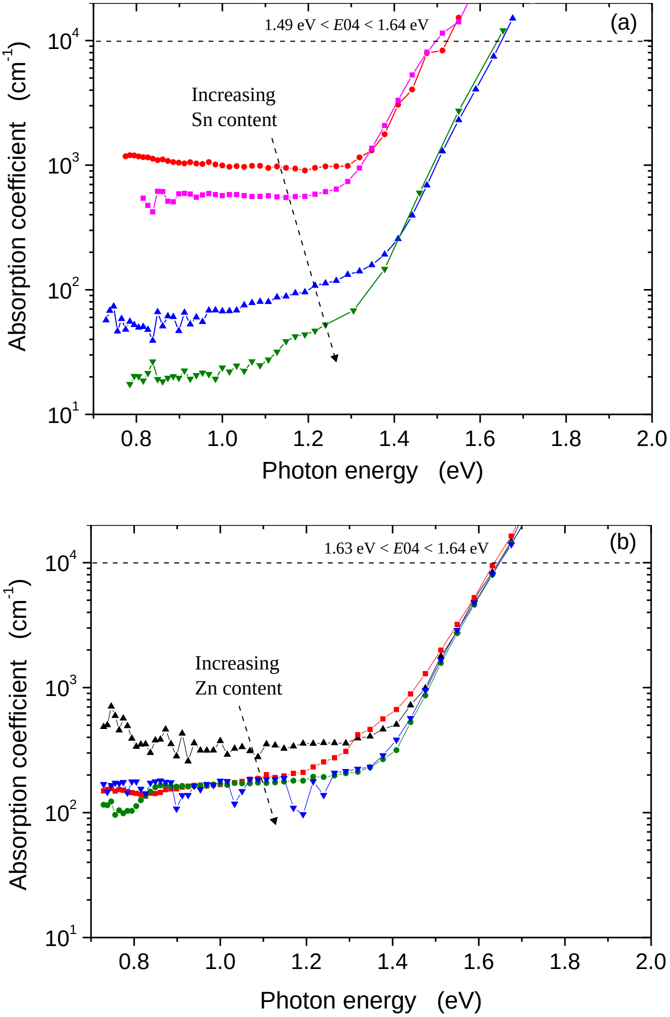

Figure 25: Absorption coefficient obtained from PDS measurements on CZTS samples with increasing content of tin (top) and zinc (bottom).

To exclude the possibility that the general trends shown by the PDS measurements are influenced by light scattering effects (evidenced by the absence of interference fringes), the scattering properties of the analyzed films have been investigated. We measured both the total (T) and diffuse (T_{diff}) transmittance of the films.

The Haze ratio, defined as T_{diff}/T, shows only small variations, completely uncorrelated with the value of the absorption coefficient. As an example, we show in Figure 26 the Haze ratio of two samples with high and low values of the sub-gap absorption. The sample with higher α shows a lower Haze ratio, thus confirming that the trend found from PDS is a real effect due to defect absorption. Anyway, because of the scattering effects, the absolute value of the absorption coefficient could be slightly overestimated.

Finally, the absorption spectra show an exponential tail (Urbach's tail) just below the energy gap. Its characteristic energy is about 70 meV in samples with large Eg and about 80 meV in sample with lower Eg.

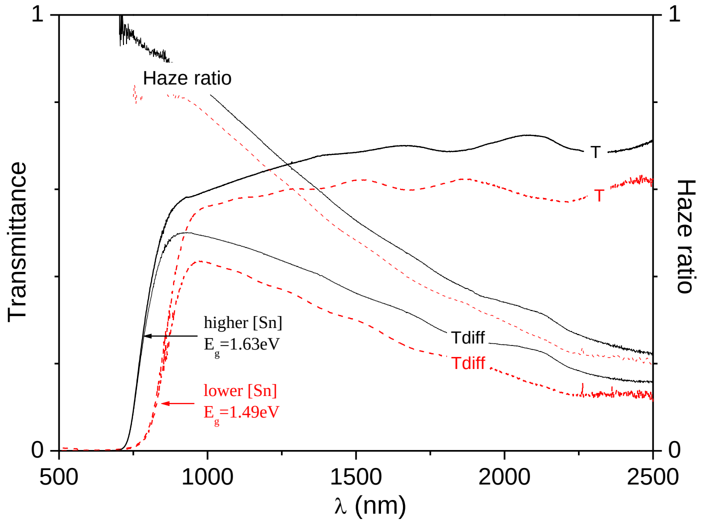

Figure 26: Haze ratios of two CZTS films with different Sn content, calculated from the total (T) and diffused (T_{diff}) transmittance spectra, also shown in the graph.

3.4.6.1 Photoluminescence in sample with different bandgap energy

Photoluminescence measurements have been performed on CZTS samples grown with different tin content and showing different band-gap energy. Two typical spectra are reported in Figure 27 and refer to two CZTS films with E04 values of 1.48 and 1.61 eV. A single large peak at about 1.3 – 1.4 eV arises from all the samples, in accordance with the typical spectra of policrystalline CZTS thin films [60].

However, the peak intensity of small-E04 samples was found to be lower of about a factor 1000 than that of samples with higher-E04. This severe intensity reduction is in accordance with the hypothesis of an increased defect density in samples with small Eg, as these additional defects, induced by the tin content reduction, can enhance the probability for non-radiative recombination mechanisms of photogenerated electron-hole pairs, thus reducing the PL signal.

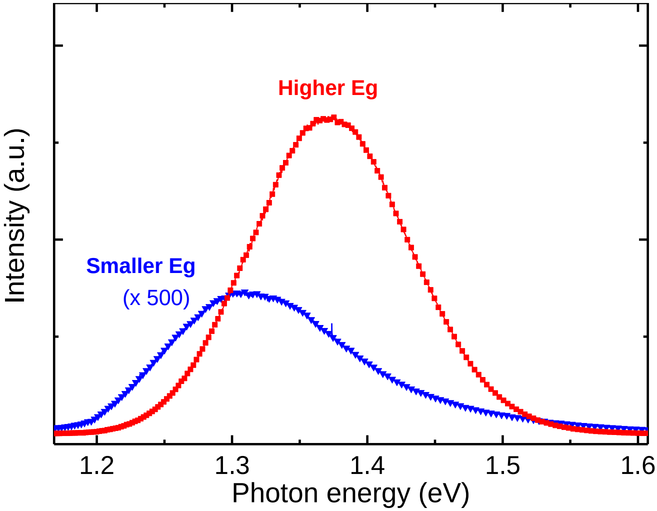

Figure 27: PL spectra of two CZTS thin films with different tin content and different energy gap: E04 = 1.48 eV (blue line) and E04=1.61 eV (red line).

Microstructrural properties

3.4.7 Influence of the tin content on CZTS microstructural properties

The results shown in previous section showed that the tin content strongly influences the optical absorption properties of CZTS thin films. For this reason, detailed microstructural investigations were made on samples prepared by varying the tin amount in the starting precursors. For this study, we used the A-series samples analyzed in the previous sections and additional CZTS films prepared with other Sn amounts, using the same growth process. A list of samples used in this work is reported in Table 12, together with the results of EDX and the energy gap values (expressed as E04).

Table 12: Sample's composition measured by EDX (normalized to total metal amount equal to 4). Values of E04 are also reported.

Sample	CZTS [Cu]:[Zn]:[Sn]:[S]	E04 (eV)
K265a	1.76 : 1.33 : 0.90 : 4	1.47
K264a2	1.76 : 1.29 : 0.94 : 4	1.47
K253a	1.63 : 1.47 : 0.90 : 4	1.48
K258a2	1.61 : 1.51 : 0.88 : 4	1.48
K241a	1.59 : 1.57 : 0.84 : 4	1.48
K261a	1.73 : 1.33 : 0.94 : 4	1.48
K252a2	1.63 : 1.47 : 0.90 : 4	1.49
K241a3	1.62 : 1.52 : 0.86 : 4	1.49
K255a2	1.76 : 1.24 : 1.00 : 4	1.60
K275a2	1.79 : 1.23 : 0.97 : 4	1.62
K256a2	1.77 : 1.24 : 0.99 : 4	1.62
K251a2	1.75 : 1.21 : 1.03 : 4	1.62
K256a	1.75 : 1.26 : 0.99 : 4	1.63
K250a	1.73 : 1.27 : 1.00 : 4	1.63
K250a2	1.71 : 1.31 : 0.98 : 4	1.63
K251a	1.79 : 1.18 : 1.03 : 4	1.63
K254a	1.77 : 1.29 : 0.94 : 4	1.64

3.4.8 Sn-site occupancy from Rietveld analysis

Rietveld analysis was used for the identification and/or quantification of spurious phases as well as for structural characterization. It is well known that this approach is based on the modeling of XRD patterns taking into account the structure factor of each present phase for the determination of the relative intensities of single reflections while peak shape depends on the instrumental contribution and on the chosen profile function [16]. To have a better understanding of the real influence of Sn-site occupancy variations on the XRD patterns, it is useful to examine the structure factor, as the measured intensity for a given reflection is proportional to its square modulus. The general expression for the structure factor can be written as:

$$F_{hkl} = \sum_{s=1}^{N_s} \left[(A_s + i\, B_s) \sum_{a=1}^{N_a^s} \left(f_{0,a} + f_a' + i\, f_a'' \right) O_a^s \right]$$

where N_s is the number of sites in the unit cell and N_a^s is the number of atoms residing in the s-site (therefore allowing the modeling of cation disorder); A_s and B_s are the cosine and sine summations for a given s-site (both depending on the Miller indexes hkl), while $f_{0,a}$ is the atomic scattering factor and f_a' and f_a'' the anomalous dispersion coefficients for the atom a. The term O_a^s corresponds to the occupancy of the a specie in the given s-site.

Using CuKα radiation, the atomic scattering factors of Cu and Zn are similar while Sn has significantly higher values. XRD peak intensities are therefore sensitive to variations of Sn content and distribution and the effect is different for different hkl reflections, as a result of compensations in the phase term of the structure factor. Figure 28 shows the intensity variation of several hkl reflections normalized to their maximum intensity upon O_{Sn}^{2b} variation (where $2b$ labels the crystallographic site of tin atoms in kesterite structure). This effect can be easily understood looking at Figure 29, which shows different crystallographic planes with high, intermediate and low tin contribution, depending on the number of tin atoms laying on the planes.

Nevertheless, it is worth noting that even if large differences on the relative intensities are obtained upon tin content variation (up to 80% for some reflections moving from site occupancy of 0.8 to full occupancy), the actual effect on the measured XRD pattern is reduced. The main problem is that actually the most influenced reflections (i.e 002 and 101) are weak peaks (less than 6% of relative intensity); while the most intense peaks remain almost unchanged with a strong variation of the tin content. Therefore, high-quality measurements, as well as careful analysis are mandatory in order to obtain a good estimation of the Sn-site occupancy.

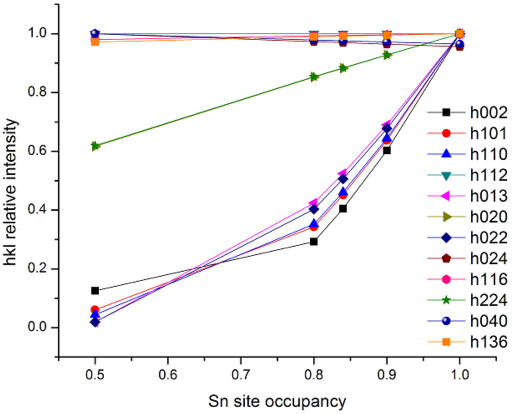

Figure 28: Variation of the relative intensities for several CZTS reflection in terms of the Sn-site occupancy.

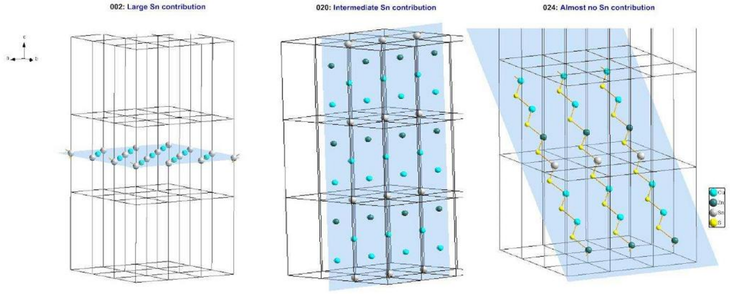

Figure 29: Atoms contained in different hkl planes: (a) (002) having large Sn contribution; (b) (020) with an intermediate concentration and (c) (024) plane having almost no Sn contribution.

In the present work, XRD patterns were acquired with a high resolution diffractometer, carefully aligned and calibrated. Instrumental profile was properly modeled with a standard NIST LaB6 sample, while several factors that directly influences measured intensities were taken into account in the fitting procedure (such as roughness, porosity [115] and thin film thickness correction). Moreover, according to the results of XPS depth profile analysis, a ZnS phase was also included as a segregated layer at the CZTS-glass interface. The X-ray absorption correction was therefore modified having considered a CZTS/ZnS/glass multilayer structure. Temperature factors were fixed to literature values [127]. As stated before, several structural parameters are obtained from the Rietveld analysis. The kesterite structure was modelled fitting lattice parameters and Sn-site occupancy, whereas the remaining sites were fixed to full occupancy.

Figure 30 shows an example of the fitting quality (GoF = 1.808) of one of the analyzed samples corresponding to the low Sn-occupancy group, where it is possible to note the good match between the proposed model and experimental data.

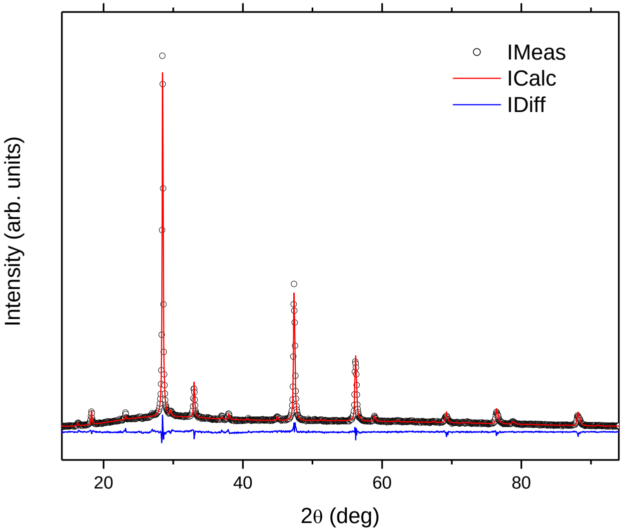

Figure 30: Rietveld analysis (CuKα radiation) of a sample with low tin content.

Results of QPA revealed a good quality of CZTS samples, with only a small amount of Sn_xS_y spurious phases, which is about 1% with exception of the most Sn-rich samples where the tin sulphides content is about 2.5%.

Furthermore, no strong variation was found in the lattice parameters *a* and *c*, having an almost constant value of about 5.432 and 10.835 Å respectively, with a *c*=2*a* ratio of about 0.997, thus suggesting the absence of phase transformations (such as kesterite/stannite transition) within this set of samples. Theoretical works are quite controversial in terms of lattice parameter ratio in CZTS polymorphic structures [112, 114], so that the polymorphic phase in our sample cannot be assessed on the basis of the c/2a ratio only. However, even though it is not easy to distinguish between the two polymorphs, the analysis of XRD peaks relative intensities gave no evidence for the formation of the stannite phase.

Sn-site occupancies resulting from Rietveld analysis are reported in Figure 31, where it is possible to note a good agreement with the tin content measured by EDX. These results were obtained using a simple model in which only O_{Sn}^{2b} was refined. However, since using CuKα radiation the Sn vacancies (V_{Sn}) cannot be distinguished from different kinds of defects (such as Zn_{Sn} or Cu_{Sn} anti-sites), different models can be taken into account for the XRD spectra analysis.

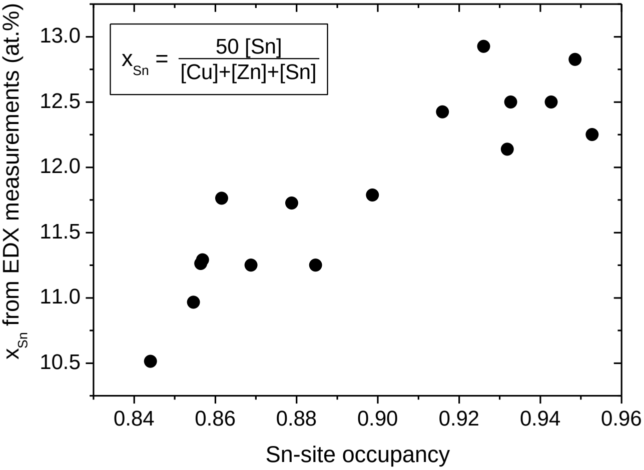

Figure 31: Correlation between the normalized tin content (xSn) measured by EDX and the Sn-site occupancy obtained by quantitative analysis of XRD spectra.

The XRD patterns can be equally well modelled using a slightly different fitting procedure, by refining both tin and zinc site-occupancies and introducing the possibility for the formation of Zn_{Sn} and Sn_{Zn} antisites (instead of V_{Sn}). This refinement tends to fill completely the Zn-site with zinc, giving no evidence for the formation of the Sn_{Zn} anti-site. An increasing Zn_{Sn} concentration (higher than the V_{Sn} predicted by the first approach) is found as the sample's tin content is lowered, but the correlation between the Sn occupancy and the Sn content is the same found before and showed in Figure 31.

3.4.9 Correlation between Eg and Sn-site occupancy

Optical measurements performed on the wide set of CZTS samples used in this work (Table 12) confirmed the trend of the bandgap energy already found for the previous analysed films (A-series samples, Table 10) and also reported in Figure 32a. The increase of the Eg with the tin content (described in functions of the [Sn]/[Cu] ratio in section 3.4.4) can be now described using the Sn-site occupancy resulting from Rietveld analysis. This parameter is a very useful quantity to describe the tin amount in different films, being referred to CZTS phase only and therefore not affected by the presence of spurious phases (which in contrast can alter the EDX results). The correlation between Eg and Sn-site occupancy is shown in Figure 32b and confirms the trend previously found using EDX analysis (Figure 24).

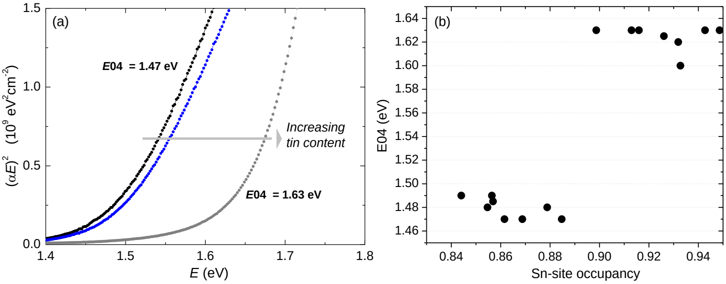

Figure 32: Variation of the optical properties (absorption spectra, panel a, and E04, panel b) in CZTS thin films with different Sn content.

3.4.10 Investigation by SRXRD: WPPM

Additional investigations on microstructural properties were made using the Whole Powder Pattern Modeling (WPPM) [80]. The term “Powder” in this case is directly related to the polycrystallinity of the present samples (i.e. absence of crystalline texture) and not to the measurement of the powder itself. Following this approach crystalline domain size can be estimated in terms of probabilistic distribution functions instead of the standard mean values (obtained from the profile peak width). To this scope, synchrotron radiation measurements (SRXRD) were performed, in order to provide a sharp instrumental profile, and therefore to allow a proper determination of the microstructural properties of the deposited films. A set of six samples (sampling from low to high tin content) was selected to this purpose. Figure 33 shows an example of the fitting quality of the measured profiles (GoF = 1.196), whereas Figure 34 shows the size distributions obtained from the WPPM analysis. As the tin content increases, three groups of distributions (labeled with A, B, C) are progressively found (see Table II): (i) samples with small average crystalline domain size ($\langle D \rangle$) with a narrow distribution (i.e. a small standard deviation); (ii) an intermediate group with also small $\langle D \rangle$ values but with a larger standard deviation and (iii) another group showing large crystalline domains having a large distribution width. Sphere-like crystalline domains are assumed and the analysis of the set of samples having small $\langle D \rangle$ (A and B groups in Figure 34) was performed with a lognormal distribution, while a gamma distribution was used for the last group (C). The expression used in this work for the two distributions are reported in the Appendix III.A, whereas the obtained size distribution function parameters (μ and σ) are reported in Table 13.

Obtained distributions were used to study the evolution of the crystalline domain size in terms of tin content. To this scope the area-weighted average was chosen ($\langle D_A \rangle = \langle D^3 \rangle / \langle D^2 \rangle$)[78]. Figure 35 depicts the variation of $\langle D_A \rangle$ in samples with different Sn-site occupancy, showing an improvement of film crystallinity with increasing tin content.

These results are in agreement with SEM cross sections of samples with different stoichiometry, revealing a large increase of average grain size with the increase of tin content. An example is shown in Figure 36.

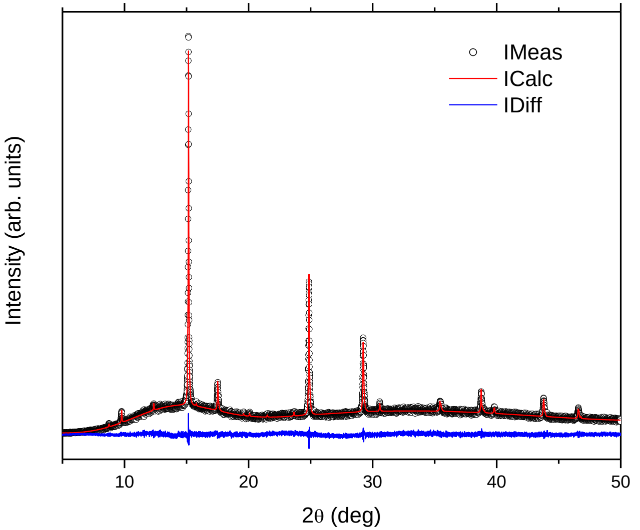

Figure 33: WPPM on SRXRD pattern (E = 15 keV) of a sample with low tin content

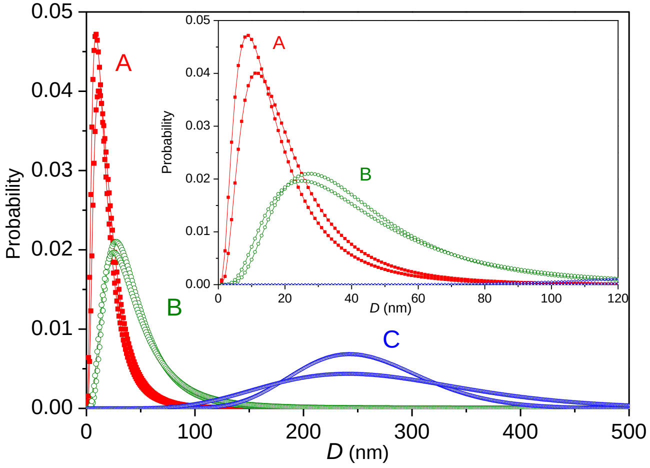

Figure 34: Domain size distribution for different CZTS thin films with different Sn content (increasing from A to C).The inset shows the first two distributions on a different scale

The influence of tin content on crystalline domain size and grain growth is not easy to understand. Although significant variations of the grain size depending on CZTS thin film stoichiometry are reported in the literature [29, 149, 151], a clear trend is difficult to be established, as opposite results were found, likely depending on the growth process. According to the precursor stoichiometry and sulphurization conditions, different phase evolutions can occur during the film growth, thus leading to different morphology. In situ XRD measurements should be used to investigate on the formation of possible growth-flux phases in our samples.

Table 13: WPPM results: size distribution function parameters μ and σ (see Appendix III.A for further details) and corresponding crystallite effective surface density η_0 (see section 3.4.11). The E04 values are also reported.

Sample	μ	σ	η_0 (cm^{-1})	E04 (eV)
K264a2	2.71	0.73	$5.2 \cdot 10^6$	1.47
K265a	2.91	0.68	$4.1 \cdot 10^6$	1.47
K256a	3.65	0.65	$1.9 \cdot 10^6$	1.63
K254a	3.61	0.58	$1.9 \cdot 10^6$	1.64
K255a2*	256.22	18.45	$2.5 \cdot 10^5$	1.60
K275a2*	274.68	8.10	$2.5 \cdot 10^5$	1.62

* Samples where Gamma distribution was used

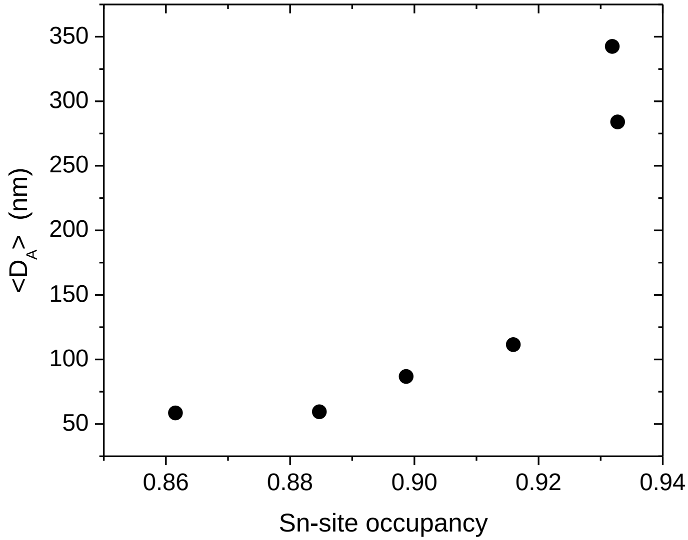

Figure 35: Correlation between ⟨D_A⟩ and Sn-site Occupancy

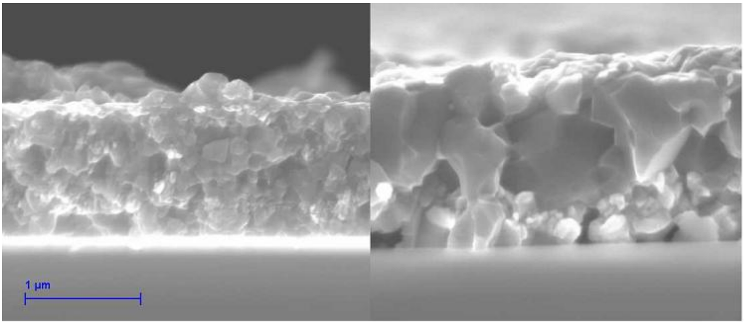

Figure 36: SEM images of the cross section of two CZTS thin films with higher (larger grains) and lower (smaller grains) tin content

3.4.11 Possible role of GBs in the energy gap variability

As result of the crystalline domain size variation revealed by microstructural analysis in samples with different tin content, different concentrations of surface defects (located, for example, at grain boundaries or at lattice dislocations) are expected in CZTS thin films depending on their composition.

These defects (hereafter simply referred to as grain boundaries, GBs) may play a role in the variability of CZTS optical properties discussed in this chapter and it can be therefore interesting to evaluate their contribution in the sub-gap absorption coefficient. This contribution can be written as:

$$\alpha_{GBs} = N_{GB}\ \eta_{GB}\sigma^{opt}\ ,$$

where N_{GB} is the defect surface density at the grain boundaries, σ^{opt} is the defect absorption cross section and η_{GB} is the surface density of the GBs (i.e. the surface of the GBs per unit volume). As a rough approximation, η_{GB} can be estimated with the crystallite effective surface density, η_0, here defined as the effective surface introduced by the crystallites per unit volume. Using the probability distribution functions, this quantity can be calculated as the average value of $S\ (D)/V\ (D)$, which is the ratio between the surface and the volume of a single spherical crystallite with diameter D:

$$\eta_0 = \int_0^\infty \frac{S(D)}{V(D)} g(D)d(D) = \int_0^\infty \frac{6}{D} g(D)d(D)$$

The results are reported in Table 13 and show an increase of η_0 from 2.5·10^5 to 5.2·10^6 cm^{-1} as the tin content (and therefore the $E04$ value) is reduced.

These values could explain the variation of the sub-gap absorption of more than one order of magnitude (see Figure 25a), but it is quite difficult to estimate the absolute value of GBs, since both N_{GB} and σ^{opt} should be known. We note that, using σ^{opt} typical values of about 10^{16}÷10^{17}cm^2, in order to explain a value of the sub-gap absorption of about 10^3 cm^{-1}, the defect surface density at the grain boundaries should be about 10^{12} ÷ 10^{13} cm^2. This value is compatible with the typical defect density observed in chalcopyrite GBs [55, 122] which is around 10^{12} cm^2. In addition to possible bulk defects which can account for the optical properties variability observed in CZTS thin films, the role of GBs cannot be excluded. Further investigations are necessary to clarify both the nature and the location of the intrinsic defects resulting from different material stoichiometry.

3.5 Appendix III.A
Lognormal and Gamma distributions

Lognormal and gamma distributions used in this work:

$$g^{Lognormal}(D) = \frac{1}{\sqrt{2\pi}D\sigma} exp\left[-\frac{1}{2}\left(\frac{lnD-\mu}{\sigma}\right)^2\right]$$

$$g^{\Gamma}(D) = \frac{\sigma}{\mu\Gamma(\sigma)}\left(\frac{\sigma D}{\mu}\right)^{\sigma-1} exp\left(-\frac{\sigma D}{\mu}\right)$$

where D corresponds to the crystalline domain size (sphere diameter), for the lognormal distribution, μ and σ are the lognormal mean and the lognormal variance respectively, whereas for the gamma distribution they correspond to the mean (first moment) and to the ratio between square of the mean and variance [14].

The second and the third moments of the two distributions are:

$$\langle D^2\rangle^{Lognormal} = exp[2(\mu+\sigma^2)]$$

$$\langle D^2\rangle^{\Gamma} = \frac{\mu^2}{\sigma}(1+\sigma)$$

.

$$\langle D^3\rangle^{\mathrm{Lognormal}} = exp\left[3\left(\mu+\frac{3}{2}\sigma^2\right)\right]$$

$$\langle D^3\rangle^{\Gamma} = \left(\frac{\mu}{\sigma}\right)^3\frac{\Gamma(3+\sigma)}{\Gamma(\sigma)}$$

Chapter IV

CZTS thin films from co-sputtered precursors

Part of this chapter has been published in:

M. Valentini, C. Malerba, F. Biccari, E. Salza, A. Santoni, C. L. Azanza Ricardo, P. Scardi, A. Mittiga

“Study of CZTS solar cells obtained from two different types of precursors”,
Proceeding of 28th EUPVSEC, (2013) pages 2459-2462
.

4.1 Introduction

One of the most important limiting factors for efficiency of CZTS solar cells is the insufficient control of the material quality [116]. Large grain size, proper thickness and appropriate nature and density of intrinsic defects are desirable properties to obtain high efficiency devices and are strongly influenced by the film composition. An accurate control of CZTS stoichiometry is therefore a very important issue for a proper optimization of the material as absorber layer.

Co-deposition of precursors has been found to be a very promising technique in terms of stoichiometry control and is currently the growth method giving the best results in terms of device efficiency [160, 72]. A uniform incorporation of Cu, Zn, Sn and S, due to the short required diffusion length, allows for fast and homogeneous CZTS phase formation during precursor annealing, thus reducing the possibility of secondary phase formation and tin loss [67, 163]. This approach was already tried by several groups and different methods (such as co-evaporation [160], co-sputtering [66, 72], reactive-sputtering [84, 32], hybrid sputtering [150]) have been reported for the precursor deposition. The sputtering deposition of CZTS from a single quaternary target was attempted by different groups [62, 67, 136], but this procedure presents some problems related to stoichiometry control, as compositional

differences between target and sputtered film are usually found [67]. Co-sputtering deposition from three different sources is a better strategy to control the stoichiometry of the final material, as the sputtering power applied to each target can be controlled separately. This approach was firstly explored by the Katagiri group [66], which used elemental Cu, ZnS and SnS compounds as sputtering sources, and other works have been then published based on similar growth processes [72, 44].
The approach used in this work is slightly different, as the starting precursors are grown by co-sputtering deposition of CuS, SnS and ZnS. The use of the three binary sulphides is not a widely explored route and could be a better technique, as both metals and sulphur can be incorporated in the correct proportion into the starting precursor. A similar approach has been reported only in few recent works [67, 59], in which Cu_2S, SnS_2 and ZnS targets were used as sputtering sources.

This chapter focuses on the description of the co-sputtering process used in this work and on the characterization of the final materials as isolated films. Chemical, microstructural and optical characterization of both precursors and CZTS films, obtained after the sulphurization treatment, is presented and compared with materials obtained from stacked evaporated precursors. The performances of these materials as absorber layers in solar cells were also evaluated and will be discussed in Chapter V.

4.2 Deposition of precursors by co-sputtering process

The precursor was grown in an Oerlikon- UNIVEX 450B system equipped with three 4 inches magnetron cathodes in confocal configuration. A picture of the sputtering system and a detail of the vacuum chamber are reported in Figure 37. The three targets (CuS, SnS and ZnS) are installed in the base plate of the chamber in sputter-up configuration and the substrates (above) are mounted on a rotating plate, which ensures uniform deposition on a 10x10 cm^2 area. SnS and ZnS are powered with two RF generators while CuS with a DC supply. The sputtering chamber is pumped by a turbo molecular pump and a base pressure lower than 10^{-6} mbar is reached before the sputtering process.

Soda lime glass (SLG) substrates were used to characterize materials as isolated film, in order to investigate their optical and microstructural properties, whereas molybdenum covered SLGs were used for films characterization as absorber layers into solar cell stack. No intentional heating of the substrate was performed during co-sputtering process.

Figure 37: Sputtering system Oerlikon Leybold Univex 450B.

The deposition process has to be optimized by choosing the appropriate Ar pressure and sputtering power of each target, in order to obtain precursors with the desired composition and good adhesion properties.

Two different sputtering pressures were chosen for precursors deposition: the lower is $3.0 \cdot 10^{-3}$ mbar and was chosen taking into account that the mean sputtering pressure reported in the literature for similar processes [66] is about $5.0 \cdot 10^{-3}$ mbar. This value was slightly reduced to compensate the greater target-substrate distance in our system (which is about 15 cm).

Some tests were also performed increasing the sputtering pressure to 10^{-2} mbar, with the aim to reduce possible mechanical stress in sputtered materials. These experiments allow studying the effect of a reduced kinetic energy of the incident specie on the film-substrate adhesion properties. Experiments at this higher pressure are still ongoing and the main results presented in this work are mainly related to material deposited at the lowest pressure.

Optimization of precursor stoichiometry has proved to be quite difficult since the growth rate of the global (quaternary) precursor is not equal to the sum of the growth rates of the single sulphides. Therefore, after a first instrumental calibration, the experimental conditions have been empirically corrected to obtain materials with optimized stoichiometry.

4.2.1 Power-rate calibration curves for co-sputtering deposition

An instrumental calibration is necessary to find a correlation between the deposition conditions (such as sputtering pressure, sputtering power and deposition time) and the amount of sputtered material.

For this purpose, each single metal sulphide was sputtered at constant pressure and constant deposition time (20 min), only changing the sputtering power applied to the target. The thickness of the films obtained with different sputtering power was then measured by using a profilometer, thus obtaining a power-thickness calibration curves. The growth rate of each material (expressed in mol/cm^2 min) was then calculated using the molar volume of the three sulphides (Vm_{ZnS}=23.83 cm^{3}mol^{-1}, Vm_{CuS}=20.09 cm^{3}mol^{-1}, Vm_{SnS}=28.88 cm^{3}mol^{-1}).

This calibration procedure was performed at two different sputtering pressures, 3.0·10^{-3} and 1.0·10^{-2} mbar, corresponding to the pressure conditions used for precursors' deposition. The obtained power-thickness and power-rate calibration curves are plotted in Figure 38.

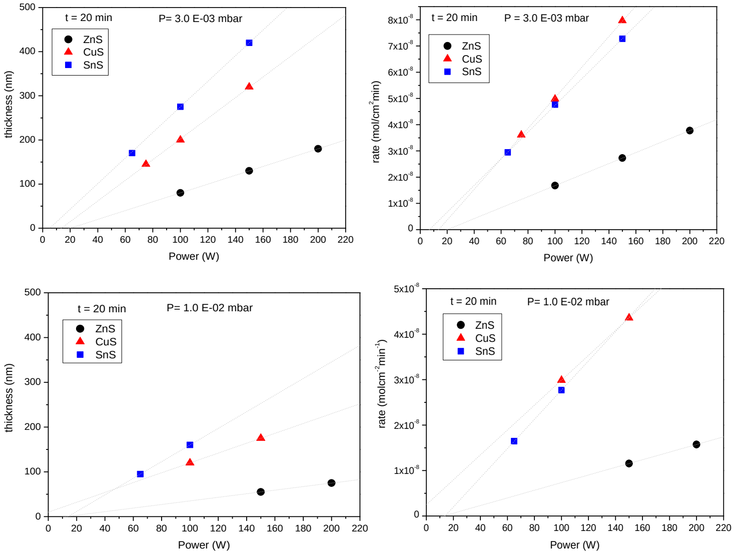

Figure 38: Power-thickness and power-rate calibration curves obtained at 3.0·10^{-3} mbar (top) and 10^{-2} mbar (bottom) sputtering pressure.

As a first approximation, assuming that the growth rate of the co-sputtered material is equal to the sum of the three binary compounds, it is possible to set the nominal precursor stoichiometry by choosing the rate of the three sulphides corresponding to the desired metal proportion and setting the sputtering powers according to the calibration curves.

In this approximation, and assuming that the growth rate of each single sulphide remains constant for different deposition time, it is possible to estimate the deposition time *t* required to obtain a precursor with a thickness *d* using the simple equation:

$$t = \frac{d}{\mathrm{rate}_{\mathrm{ZnS}} \cdot \mathrm{Vm}_{\mathrm{ZnS}} + \mathrm{rate}_{\mathrm{CuS}} \cdot \mathrm{Vm}_{\mathrm{CuS}} + \mathrm{rate}_{\mathrm{SnS}} \cdot \mathrm{Vm}_{\mathrm{SnS}}}$$

The deposition conditions chosen following this procedure will require additional optimization to take into account that:

1. The growth rate of the quaternary compound during co-sputtering of the three target can be different from the one calculated using the growth rate of the single sulphides.
2. The growth rates of single sulphides have been calculated using the film thickness and theoretical molar volume. However, the effective deposited mass could be different from what expected from these calculation due to possible morphological and chemical difference between the sputtered films and the corresponding ideal bulk materials.

4.2.2 Post-calibration corrections: empirical optimization of precursor composition

The calibration procedure described in the previous section was only used to obtain a first setting of the deposition conditions, which were then experimentally adjusted to correct the discrepancy between the nominal and the real material composition.

Indeed, calibration curves were obtained from sputtering deposition of the single sulphides on soda lime glass substrates, but the growth rates are expected to be different when the three sulphides are sputtered simultaneously.

A first reason could be a different sticking coefficient of sputtered species on single metal sulphides or on the co-sputtered quaternary compound. Moreover, in the co-sputtering process, the deposition conditions could be altered by possible interference phenomena among the electric fields of the three targets, used simultaneously.

Another reason for the discrepancy between the nominal and the real composition of the sputtered materials could be a possible difference between the film and the bulk density, arising, for instance, from possible porosity of the sputtered film or from a different stoichiometry between the target and the deposited material.

This possibility was confirmed by some thickness and mass measurements performed on the single binary sulphides and on the co-sputtered quaternary compound, deposited at 10^{-2} mbar with the same sputtering power. The results reported in Table 14 show a difference between the density found for the sputtered films (ρ_{exp}) and the theoretical value reported for the bulk materials (ρ_{teo}). These data can be used to estimate the material porosity, defined as the ratio between the voids and the total volume $\left(V_p / V_T\right)$. Its value varies from 0 (for the ideal bulk material) to 1 (the upper limit for porous material) and can be simply calculated using the expression:

$$porosity = \frac{(V_{exp} - V_{teo})}{V_{exp}} = 1 - \frac{V_{teo}}{V_{exp}} = 1 - \frac{\rho_{exp}}{\rho_{teo}},$$

where V_{exp} is the measured total volume (V_T) and V_{teo} is the teoretical value expected for a material with the measured mass and teoretical density ρ_{teo}.

These calculations show a very low porosity for the sputtered ZnS, whereas higher porosity is found for SnS film, which can result in an overestimated growth rate for this specie. The results obtained for CuS film cannot be explained in terms of porosity, since a negative value was found. A possible explanation is instead a different nature of the sputtered film with respect to the target: the formation of a Cu_2S phase, with higher density (5.6 g/cm^2) than CuS, could account for the higher value of ρ_{exp} compared to the theoretical density expected for a copper(II) sulphide film. These measurements should be repeated for different powers (and for both pressure conditions, $3x10^{-3}$ and $1x10^{-2}$ mbar) and could be used to correct the power-rate calibration curves using the corrected growth rate resulting from the effective measured mass (instead of the measured thickness and theoretical molar volume).

Table 14: Results of thickness and mass measurements on single binary sulphides and quaternary co-sputtered compound, deposited at 10^{-2} mbar. Theoretical and experimental density and porosity are also reported for each material.

Material	SnS	ZnS	CuS	Cosputtered film
$mass_{exp}$ (mg/cm^2)	0.1429	0.1238	0.2033	0.5339
$thickness_{exp}$ (nm)	347	310	375	1280
ρ_{exp} (g/cm^3)	4.12	3.99	5.42	4.17
ρ_{teo} (g/cm^3)	5.22	4.09	4.76	4.56
Porosity	0.21	0.03	-0.14	0.08

However, this procedure would be quite long and, even using the corrected calibration curve for each sulphide, the precursor composition could not be anyhow predicted *a priori* because of the aforementioned problems arising during co-sputtering deposition (such as different sticking coefficients and electric field interference).

For this reason, chosen the initial nominal composition and thickness, the deposition conditions (sputtering powers and deposition time) were firstly fixed according to the calibration curves reported in Figure 38 and adjusted *a posteriori*, using thickness and compositional measurements on the final materials.

Examples of the experimental procedure are reported below.

Sputtering power and deposition time were firstly set in order to obtain a 1.2 µm thick precursor with a Zn-rich and Cu-poor nominal composition, close to Cu:Zn:Sn:S= 1.80:1.20:1.00:4. These metal ratios were chosen taking into account the stoichiometry reported in the literature for CZTS thin film which gave the best results in terms of solar cell efficiency [160].

Using the calibration curves at $3 \cdot 10^{-3}$ mbar, the three sputtering powers were set at the values P_{DC}(CuS)=107 W, P_{RF}(ZnS)=200 W, P_{RF}(SnS)=66 W, corresponding to the nominal composition reported in Table 15 and the deposition time was fixed to 41 min (calculated from equation 1). However, EDX measurements on the precursor deposited in these conditions (sample SP20 in Table 15) show a discrepancy between the actual and the expected composition. EDX measurements were therefore used to correct the sputtering powers and a precursor with the desired metal proportion (close to the nominal composition) has been obtained (see SP04, Table 15).

This result reveals the co-sputtering deposition as a powerful method, allowing a good control of material stoichiometry, which can be varied as requested by properly set the sputtering conditions.

Table 15: Sputtering powers, deposition time, thickness and EDX results (with the total metal amount normalized to 50 at.%) of some selected samples deposited at $3 \cdot 10^{-3}$ mbar. Nominal composition and thickness of an ideal precursor (Nom.) and the corresponding sputtering conditions (powers and deposition time) predicted by calibration curves are also reported for comparison.

prec.	P_{DC} CuS (W)	P_{RF} ZnS (W)	P_{RF} SnS (W)	t (min)	D (nm)	Cu (at.%)	Zn (at.%)	Sn (at.%)	Cu:Zn:Sn
Nom.	107	200	66	41	1.20	22.62	15.13	12.25	1.81 : 1.21 : 0.98
SP20	107	200	66	41	1.35	20.27	17.32	12.42	1.62 : 1.39 : 0.99
SP04	109	200	70	41	1.37	21.94	15.77	12.30	1.75 : 1.26 : 0.98
SP19	116	200	63	41	1.38	21.65	17.61	10.74	1.73 : 1.41 : 0.86

The deposition conditions of the starting precursors were further empirically optimized taking into account the performances of the final CZTS films (obtained upon precursor sulphurization) as absorber layer in solar cells. The best precursor obtained in this first stage of the process optimization is the sample SP19 (see Table 15): despite the large excess of the zinc content, the CZTS thin film produced from this precursor gave a device with efficiency over 4%. Details and characterization of CZTS devices are deferred to Chapter V.

Besides the optimization of the sputtering powers, further process optimization concerns the deposition time. Indeed, to further improve solar cell performances, precursor deposition time was shortened to reduce the CZTS film thickness, thus resulting in a smaller device series resistance.

As discussed before, stoichiometry variations are expected according to different deposition time, due to possible variation of the growth rate. An example is reported in Table 16, where we report the EDX results of different precursors obtained from decreasing deposition time, using the same power conditions of SP19.

Table 16: Sputtering process conditions, thickness and composition of three precursors deposited at $3 \cdot 10^{-3}$ mbar, with the same sputtering power. The last sample is the current record material, obtained after empirical correction of the sputtering powers.

Prec.	P_{DC} CuS (W)	P_{RF} ZnS (W)	P_{RF} SnS (W)	t_{dep} (min)	d (um)	EDX – Precursor			
						Cu	Zn	Sn	Cu:Zn:Sn:S
SP19	116	200	63	41	1.38	21.65	17.61	10.74	1.73:1.41:0.86
SP33	116	200	63	30	1.08	20.73	18.14	11.13	1.66:1.45:0.89
SP29	116	200	63	21	0.75	20.90	18.26	10.83	1.67:1.46:0.87
SP36	107	200	66	20	0.70	20.07	19.66	10.27	1.61:1.57:0.82

EDX results could suggest a slight decrease in the copper content and a slight increase in the zinc concentration as deposition time is reduced. However, taking into account typical error of EDX analysis (about ±1 at.%), a clear trend between deposition conditions and precursor stoichiometry is difficult to established.

Therefore, once fixed the deposition time, the sputtering powers have to be further corrected taking into accounting the EDX chemical analysis of the final materials and the correlation with the device efficiency. The best materials are currently obtained using the deposition conditions corresponding to the sample SP36 (Table 16). These studies are still ongoing, but the current optimized process already allows obtaining devices with over 5%, thus fulfilling the goal set for this work.

4.2.3 Adhesion of precursors

Co-sputtered precursors usually show a good adhesion on molybdenum substrate, but adhesion problems often arise from deposition on SLG. Delamination of CZTS films during the heat treatment of co-sputtered precursors deposited on SLG substrates has been already reported in the literature [133]. In our work, buckling of precursors is occasionally observed and suggests a high compressive stress in as-deposited materials.

A picture of a typical failed precursor, observed at optical microscope, is shown in Figure 39.

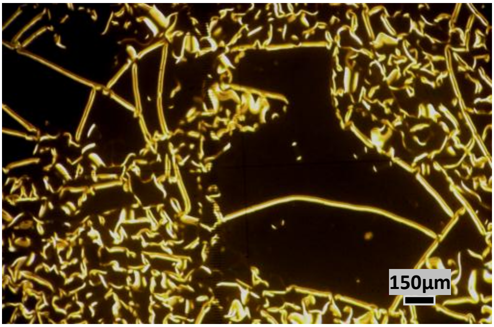

Figure 39: Picture from optical microscope of a typical failed precursor, buckling under compressive stress.

Further investigations are required to explain the origin of this problem. Indeed, in addition to the nature of the substrate, film stoichiometry also seems to influence the adhesion properties, which is worst in Cu-rich and Sn-poor samples, whereas is improved for high zinc content.

Higher sputtering pressure could improve the adhesion on the substrate, as lower kinetic energy of the sputtered specie could reduce possible mechanical stress responsible for the film detachment. Sputtering deposition process at 10^{-2} mbar seems to give precursors with better adhesion even on SLG substrates, but, at this pressure, the optimization of the sputtering powers to obtain material with optimized composition have still to be concluded.

4.3 Sulphurization treatment for conversion of co-sputtered precursors into CZTS thin films

Co-sputtered precursors could require simpler heat treatment with respect to the stacked structures, since in the latter the zinc sulphide and metals (Cu, Sn) must react with sulphur and interdiffuse, whereas in the former the three sulphides are already homogeneously mixed and already contain the proper sulphur amount. Simple heat treatments in a pure nitrogen atmosphere and with short dwell time (of the order of few minutes) should be sufficient, in principle, for the conversion of precursors into CZTS phase and for a good recrystallization of the film [133].

Preliminary experiments were therefore performed by using both annealing in pure nitrogen flux and heat treatment in sulphur atmosphere. Both the processes were performed at 550°C (reached with a heating ramp of 20°C/min) in tubular furnace, putting the precursors into a closed (but not sealed) glass reaction chamber, (see Figure III - 2). In case of heat treatment in sulphur atmosphere, sulphur powder is placed into the reaction chamber, close to precursors.

First experiments were performed using short annealing time (15 min) and no additional sulphur (or with a very small amount, about 20 mg). The same precursors were also treated using the standard sulphurization process already used for stacked layer precursors, using a stoichiometric excess of sulphur (180 mg) and a dwell time at 550°C of 1 hour. The cross sections of the CZTS samples resulting from these two treatments are compared in Figure 40.

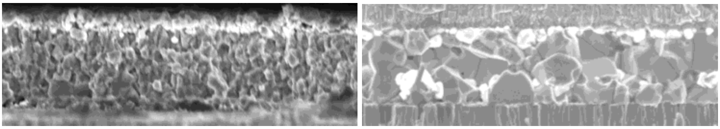

Figure 40: Comparison of two cross sections of CZTS thin films obtained from the same precursor after a sulphurization treatment with: (left) 30mg of sulphur and 15 min dwell time at 550°C and (right) 180mg of sulphur and dwell time 60min.

The latter sulphurization process gave materials with larger grains and with better performances as absorber layer in solar cells. Despite the not-still optimized stoichiometry of precursors used for the first experiments, additional test performed in the course of our studies confirm that improvement of the material quality in terms of both morphology and PV performances is obtained by using longer sulphurization treatment with a large excess of sulphur in the reaction chamber.

.

Figure 41 shows a comparison between two CZTS films obtained from the same (optimized) precursor, treated with 180 mg of sulphur by changing the dwell time at 550°C: 15 min (left side) and 60 min (right side) long processes were used for the selected samples.

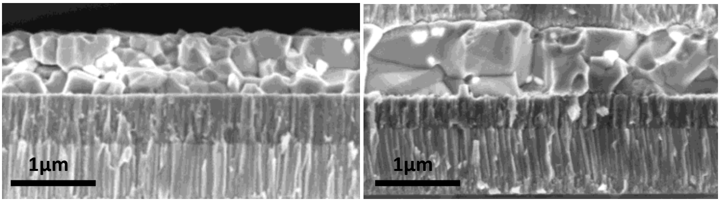

Figure 41: Cross sections of two CZTS thin films obtained from sulphurization of co-sputtered precursors with 180 mg of sulphur, using a dwell time at 550°C of 15 min (on the left) and 60 min (on the right).

Other experiments were performed using one hour long processes by changing the sulphur amount from 20 to 180 mg. The cross sections (on the same scale) of three CZTS films grown from the same precursors, treated with 20, 90 and 180 mg of sulphur, are compared in Figure 42, showing comparable grain dimensions. This result shows that, for sufficiently long annealing time, a good recrystallization of the final material can be obtained even using a reduced tin amount in the reaction chamber.

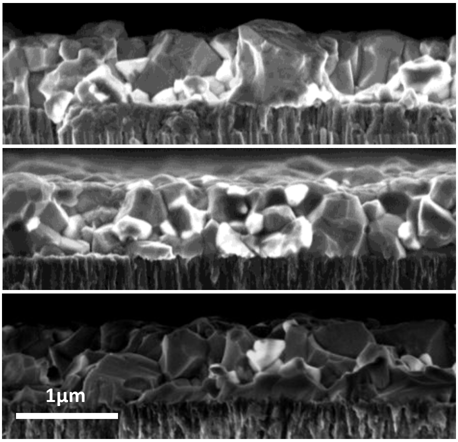

Figure 42: Cross sections of three CZTS films obtained from the same precursor, using 60 min long sulphurization treatment, with different amount of sulphur: 20mg (top), 90mg, and 180mg (bottom).

However, the samples produced with the largest amount of sulphur showed better performances as absorber layer. Some examples are reported in Table 16, where the efficiency of two pairs of solar cells produced from CZTS films grown from the same precursors treated with 90 and 180 mg of sulphur are compared. The cross sections of two of devices are also shown in Figure 43.

Table 17: Efficiency of CZTS solar cells obtained from sulphurization of precursors with different sulphur amount (S).

Prec.	device	S (mg)	t (min)	P_{DC} CuS (W)	P_{RF} ZnS (W)	P_{RF} SnS (W)	Eff. (%)
SP41	KC208	180	60	107	200	66	3.44
SP41	KC209	90	60	107	200	66	1.90
SP42	KC203	180	60	107	180	66	3.27
SP42	KC210	90	60	107	180	66	1.22

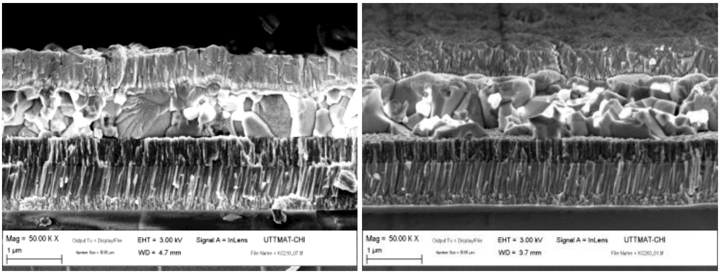

Figure 43: Cross sections of the devices KC210 (eff. 1.22%) and KC203 (eff. 3.27%), produced from the same precursor (SP42), treated with 90 and 180 mg of sulphur.

The reason of these results is still unclear and requires further investigation: no significant variation of chemical composition have been indeed revealed by EDX measurements on samples produced by the same precursor, changing the sulphur amount in the reaction chamber, and even microstructural analysis performed by XRD and Raman spectroscopy reveal that sample showing CZTS as the main phase, with no evident signal from other detectable spurious compounds, can be obtained even by using short annealing time or reduced sulphur content.

Additional experiments are necessary to understand the correlation between the sulphurization conditions and the device performances, in order to optimize a new growth process to obtaining good quality CZTS absorber layers by fast annealing processing. Investigations on this issue are still on-going, but some difficulties arise from the fact that, in addition to the different quality of materials produced by different heat treatments, collateral effects (arising, for instance, from different extent of the back-contact sulphurization) have to be also taken into account.

On the basis of the results of our preliminary sulphurization tests, to achieve a fast improvement of the device performances, CZTS thin films have been produced by using 1 hour long annealing with a sulphur amount fixed at 180 mg and the following work focused on the optimization of the final material by changing the stoichiometry of the starting precursors. The sulphurization treatment used for co-sputtered precursors is the same previously adopted for stacked layer precursors, so that a simple comparison of materials grown from the two different precursors' type is allowed.

4.4 Characterization of optimized co-sputtered precursors and CZTS thin films

A typical cross section of a co-sputtered precursor is reported in Figure 44. XPS depth profiles, reported in the same figure, reveal a very good homogeneity in as deposited materials, with a uniform metals distribution and with sulphur content close to the stoichiometric value. The same characterizations performed on the final material (Figure 45) show that a good recristallization is obtained upon sulphurization treatment and a quite good homogeneity is also preserved in the final CZTS film.

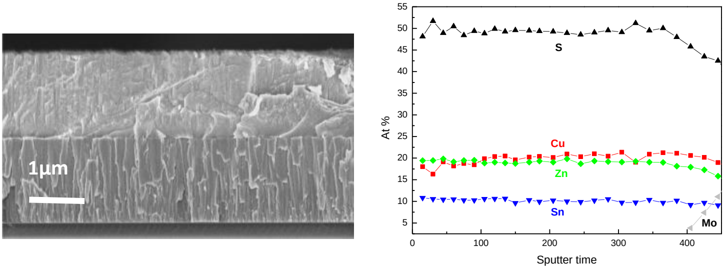

Figure 44: SEM cross section of a co-sputtered precursor (left) and corresponding depth profiles measured by XPS.

EDX measurements don't show significant changes of samples' stoichiometry upon precursor sulphurization: some examples are reported in Table 18, where we report the composition of two co-sputtered precursors (SP19, SP36) and the corresponding CZTS films. The results show very similar compositions, with variation below the typical error of EDX (about 1%).

The large excess of zinc revealed by EDX is related to the not still optimized stoichiometry of our precursors. Even though a Zn-rich compositions is desired to improve the material quality as absorber layer [70], our best materials still show a too high zinc content. Despite this large deviation from the perfect stoichiometry, solar cells with efficiency exceeding 5% have been obtained with the current materials. Precursors with lower zinc content have been recently produced. The results obtained from these materials are discussed in section 4.5.

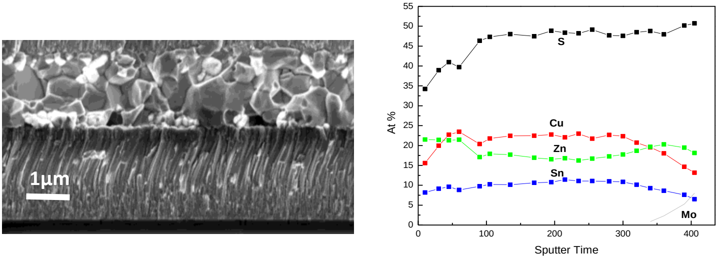

Figure 45: SEM cross section of a CZTS thin films and corresponding depth profiles measured by XPS.

Table 18: Chemical composition from EDX (with the total metal amount normalized to 50%) of co-sputtered precursors and the corresponding CZTS films obtained upon their sulphurization.

Sample		Cu	Zn	Sn	Cu:Zn:Sn
Precursor:	**SP19**	21.65	17.61	10.74	1.73:1.41:0.86
CZTS from SP19:	**K394**	21.71	17.33	10.96	1.74:1.39:0.88
Precursor:	**SP36**	20.09	19.63	10.28	1.61:1.57:0.82
CZTS from SP36:	**K422**	20.68	18.83	10.49	1.65:1.51:0.84

The XRD spectra of a typical co-sputtered precursor and the corresponding CZTS film are reported in Figure 46. Precursor's pattern shows only the main diffraction peaks expected from a zincblende structure, with no reflection related to low symmetry phases such as kesterite or Cu-Sn-S compounds. As observed by other authors in the literature [133], also in our co-sputtered material an additional peak at about 2Θ=27° is detected. This peak (marked with * in Figure 46 and Figure 47) is probably due to a small amount of hexagonal ZnS phase, since it matches its (100) reflection and it is also found in pure ZnS films produced in our sputtering system: in Figure 47, the grazing incidence XRD spectra of two sputtered ZnS films (deposited with a sputtering power of 100 and 200W) are reported. These patterns match with a polycrystalline hexagonal ZnS phase (wurzite 8H-PDF#39-1363). The difference with the cubic structure (sphalerite, PDF#05-0566) consists mainly in the contribution at about 27°, while the other peaks are almost the same for the two structures. As suggested in [133], precursor spectra could be compatible with a cation disordered CZTS phase. The broad shape of the diffraction peaks reveals a small grain size of the as-deposited materials, which instead show an improved crystallinity upon sulphurization. XRD diffraction pattern of the final material shows narrow peaks, matching all the reflections expected from the kesterite CZTS phase, with no detectable signals of other spurious phases. In some cases, a weak peak at 27° is also observed in the final CZTS films, suggesting the presence of small hexagonal ZnS domains. It has to be noted that the same peak has been also reported in [90], where it is instead attributed to the presence of stacking-faults.

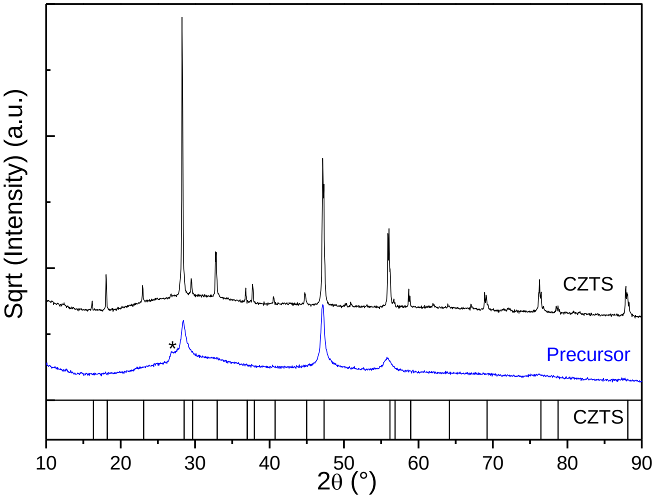

Figure 46: XRD spectra of a co-sputtered precursor and the final CZTS film obtained upon sulphurization. Literature peak positions for CZTS phase (XRD card #26-0575) are also marked.

Raman spectra of a typical precursor and of the corresponding CZTS film are reported in Figure 48. Co-sputtered precursor shows the presence of the main vibrational mode peak of kesterite phase at 335 cm^{-1} (close to the reference value of 338 cm^{-1} [4]). The broadening of this band and its low intensity is due to a small phonon correlation length, related to the small grain dimension of the precursor. A second broad band is also visible at around 300 cm^{-1} and could be imputed to a nanocrystalline CTS phase [39]. In some cases, a small signal at about 190 cm^{-1} is also detected, revealing the presence of a SnS_2 phase. Upon sulphurization, the spectrum sharpens and kesterite characteristic peaks become more evident, while signals related to spurious phases usually disappear (in some cases a small signal from SnS_2 phase is detected also in the final materials).

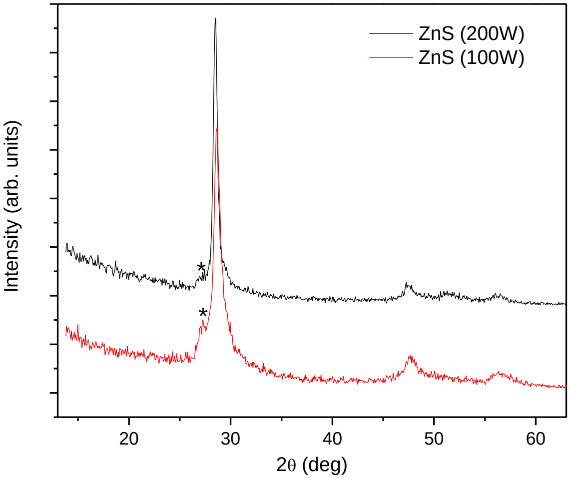

Figure 47: Grazing incidence XRD spectra of two single layers of pure ZnS deposited with our co-sputtering system, using a sputtering power of 100W and 200W. These patterns match with a polycrystalline hexagonal ZnS phase (wurzite 8H-card #39-1363).

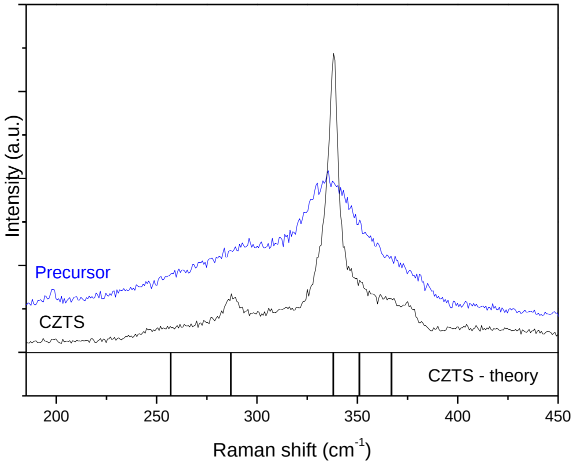

Figure 48: Raman spectra of a co-sputtered precursor and the corresponding CZTS film. Literature peak positions for CZTS phase [4, 34] are also marked.

In Figure 49 the transmittance spectra of a co-sputtered precursor and the corresponding CZTS film are reported. The latter was used to obtain the absorption coefficient (α) of the final materials (see Chapter III, eq. 1) and the energy gap was estimated by using the E04, defined as the energy value at $\alpha=10^4 cm^{-1}$ (for the sample reported in figure the resulting value of E04 is 1.54 eV). The absorption edge of the precursor is at higher wavelength respect to that of the final CZTS film, thus revealing smaller bandgap energy of the as-deposited materials. This can be consistent both with a strongly disordered CZTS (with wide band tails), or with the presence of secondary phases with a band gap energy smaller than CZTS, such as Cu_2SnS_3 (Eg~1.35 eV) or SnS (Eg~1.30 eV).

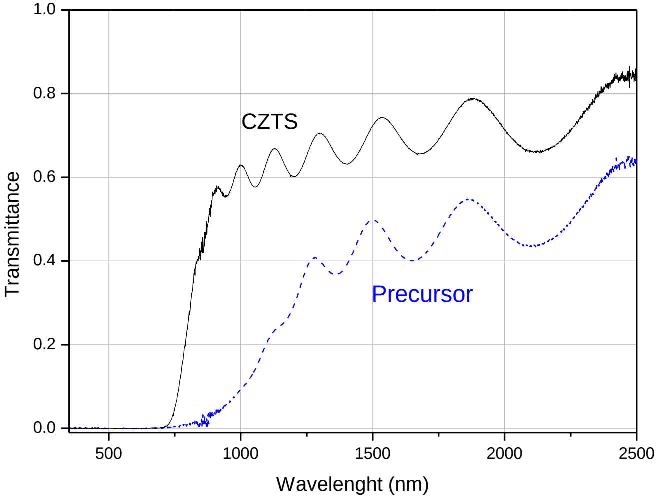

Figure 49: Transmittance spectra of a co-sputtered precursor and the final CZTS sample.

The absorption spectra of two CZTS thin films with different stoichiometry are compared in Figure 50. The values of the E04 are reported in Table 19, together with the EDX data measured on the corresponding precursors. The larger energy gap of the CZTS film with higher [Sn]/[Cu] ratio is in accordance with the trend of the E04 found for stacked layer precursors (see Figure17). However, further experiments should be necessary to confirm this result, but the adhesion problems of co-sputtered materials on SLG substrates make additional investigations very difficult.

Table 19: Metal ratio (2Sn/Cu and Zn/Sn), measured by EDX, of co-sputtered precursors with different composition and E04 of the two corresponding CZTS films.

CZTS	**Prec.**	2Sn/Cu	Zn/Sn	E04 (eV)
K342	**SP03**	1.20	1.26	1.60
K372	**SP18**	1.08	1.39	1.50

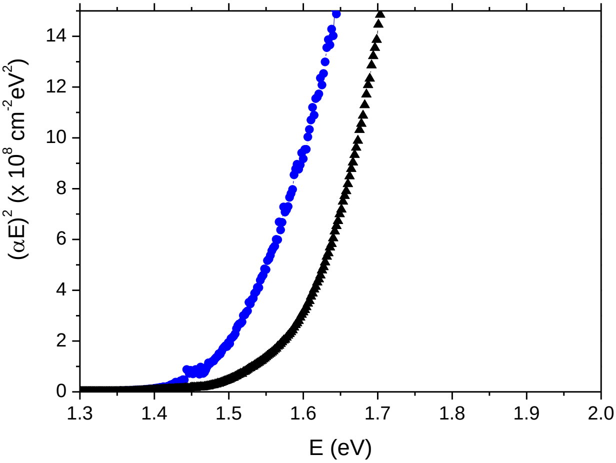

Figure 50: Transmittance spectra of CZTS thin films grown from co-sputtered precursors (SP03, blue data, and SP18, black data) with different stoichiometry (see Table 19).

4.4.1 Comparison between CZTS samples obtained from stacked evaporated and co-sputtered precursors

In Figure 51 and Figure 52, XRD patterns and Raman spectra of two optimized CZTS samples obtained from co-sputtered and stacked evaporated precursors are compared. After a proper optimization of the two processes, both techniques allowed obtaining high quality CZTS films in term of morphology and microstructure: XRD and Raman spectra show only the main peaks related to CZTS phase, with none of the signals expected from detectable secondary phases (such as tin and copper binary sulphides and Cu-Sn-S ternary phases). The peak width is also comparable and reveals a good material recrystallization upon annealing, as also confirmed by SEM characterization (see Figure 53).

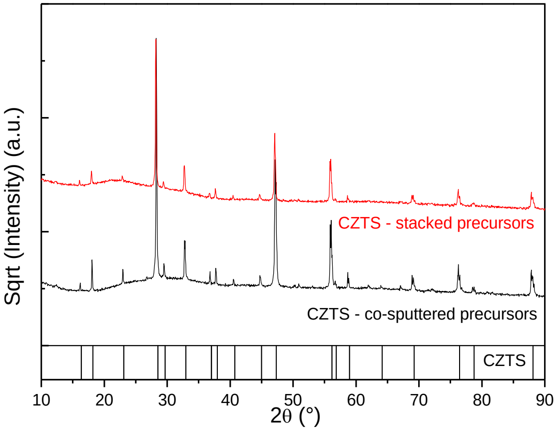

Figure 51: Comparison of XRD spectra of two CZTS thin films obtained from co-sputtered and staked evaporated precursors. CZTS reference peaks are also marked (XRD card #26-0575).

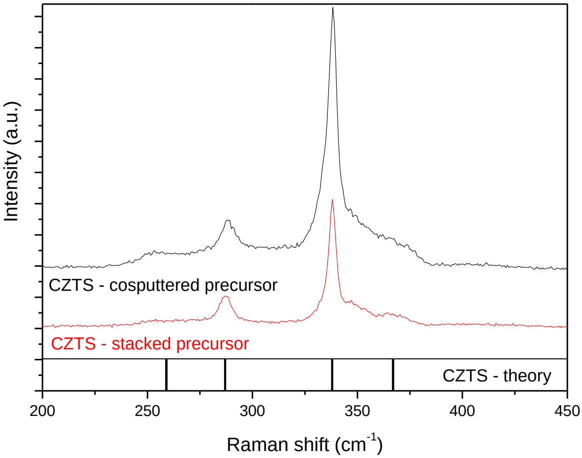

Figure 52: Comparison of Raman spectra of two CZTS thin films obtained from co-sputtered and staked evaporated precursors. Reference peaks are also marked [4, 34].

However, co-sputtering deposition technique was found to be a better strategy in terms of both homogeneity and control of chemical composition. XPS depth profiles of CZTS films obtained from the two growth techniques have been already shown in the previous sections (Figure 45 and Figure 17); for simplicity of comparison, the results are also reported in Figure 54.

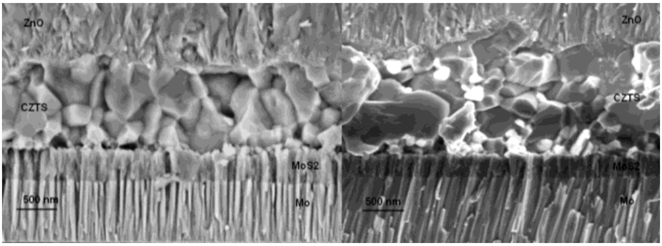

Figure 53: Cross section of two typical CZTS thin films grown from stacked evaporated and co-sputtered precursors.

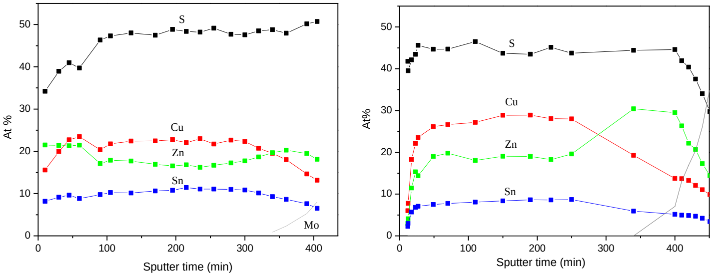

Figure 54: XPS depth profiles of the elements in a two CZTS thin films obtained from co-sputtered (left) and stacked layer precursors (right).

The Zn-rich stoichiometry usually adopted for CZTS samples give rise to ZnS spurious phase segregation in materials grown from stacked precursors, thus making difficult to control and check the material chemical composition. On the contrary, even in case of off-stoichiometry composition, a very good homogeneity is found in as deposited co-sputtered precursors (see Figure 44) and a quite good uniformity is also preserved in the final samples.

Due to material chemical homogeneity, together with the possibility for an accurate control of the film stoichiometry by properly setting the sputtering powers, co-sputtering method is a promising strategy to properly optimize CZTS thin films as absorber layers in solar cells.

4.5 Blistering effect in CZTS thin films

As discussed in the previous sections, our best solar cells suffer from absorber layers which still show an exaggerate zinc content. The current work is therefore addressed to reduce the zinc amount in the starting precursor.

Materials with different zinc content have been recently produced by varying the sputtering power applied to the ZnS target. A list of three selected samples are reported in Table 20. The precursors have been grown using deposition conditions similar to those of the current record material (SP36, see Table 16), but decreasing the ZnS target power supply from 200W to 160W. The deposition time was slightly modified to obtain samples with the same thickness (about 700 nm).

CZTS films grown from these materials have shown a great improvement in morphology. An example is shown in Figure 55, where two cross sections of CZTS films produced from the precursor SP41 (P(ZnS)=200W) and SP43 (P(ZnS)=160W) are compared. Even if a distribution of grain dimension is present, several grains spanning all the sample thickness can be found in the CZTS film with lower zinc content.

Table 20: Sputtering process conditions, thickness and composition of three precursors deposited at $3\cdot10^{-3}$ mbar, with the same sputtering power. EDX data are normalized with total metal amount of 50%. The last sample has been grown by adding 2min of sputtering from single ZnS target.

Prec.	P_{DC} CuS (W)	P_{RF} ZnS (W)	P_{RF} SnS (W)	t_{dep} (min)	Cu (at.%)	Zn (at.%)	Sn (at.%)
SP41	116	200	63	20	19.05	19.07	11.88
SP42	116	180	63	21	20.23	17.56	12.21
SP43	116	160	63	22	20.79	16.14	13.07
SP44	116	160	63	22+2	21.24	16.58	12.18

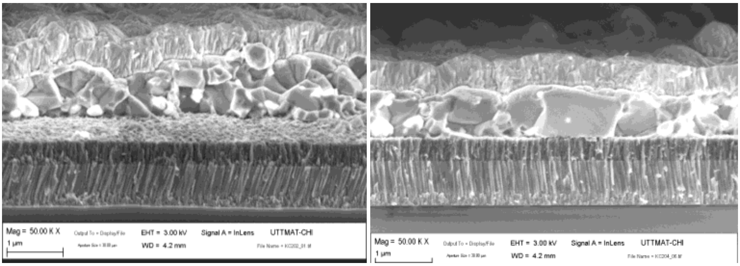

Figure 55: Cross sections of two CZTS films produced from precursors SP41 (P(ZnS)=200W, left side) and SP43 (P(ZnS)=160W, right side)

However, these samples show severe adhesion problems on molybdenum substrates: an example is shown by the SEM images in Figure 56 and Figure 57, showing a clear blistering effect in CZTS film with reduced zinc content.

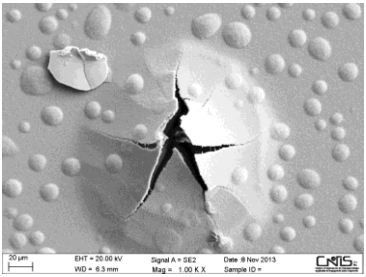

Figure 56: SEM image of the surface of a typical CZTS sample showing blistering effect.

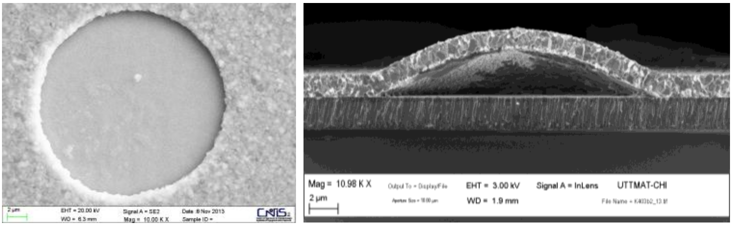

Figure 57: Details of the surfaceand cross section of a CZTS sample showing blistering effect.

Similar blistering phenomena in other materials have been reported in the literature and have been imputed to high compressive stress state [31]. Other works suggest that blistering is due to the formation of gaseous phases at the film/substrate interface, in material showing tensile stress [155].

According to[31], the intrinsic stress ($|\sigma|$) of a thin film showing blistering effect can be calculated by using the ratio between the blister height (h) and diameter (c) with the equation:

$$|\sigma| = 4.88 \cdot E \left[k \left(\frac{h}{c}\right)^2 - \left(\frac{t}{c}\right)^2 \right],$$

where E is the Young modulus, *t* is the film thickness and $k$is given by

$$k = 0.2473 \left[(1+\nu) + 0.2331(1-\nu^2) \right],$$

where ν is the Poisson ratio of the film. Elastic constants of CZTS have been obtained from ab-initio calculation by He et al. [56], which predict a Poisson ratio of $\nu = 0.308$ (corresponding to $k = 0.3756$) and a Young Modulus $E = 77.8$ GPa. From SEM characterization, the typical diameter of blisters in our materials is about 20 µm. The height can be estimated by looking at the SEM cross sections, even if some error could arise from the fact that the fracture of the film and the blister centre could not correspond. From the detail of the sample shown in Figure 57 (right side), we can estimate *c*, *h* and *t* with 19 µm, 3.3 µm and 1.6 µm respectively, thus obtaining $|\sigma| = 1.6$ GPa. In a thinner sample (not shown here), with t=0.8um, we found $c \approx 19$ µm and $h \approx 4.4$ µm, thus obtaining $|\sigma| \approx 7$ GPa.

Some calculations have been performed to evaluate possible contribution from thermal stress (σ^{th}) , arising from the heat treatment of our samples.

The thermal stress can be obtained by the product of the biassial strain (ε) and the biaxial modulus $[E/(1-\nu)]$. For a film grown at temperature T_1 and heated at temperature T_2, the biaxial strain is given by:

$$\varepsilon = -\left(\alpha_{film} - \alpha_{sub}\right)(T_2 - T_1),$$

where α_{film} and α_{sub} are the thermal expansion coefficients of the film and the substrate respectively. According to experimental works [90, 125], the thermal expansion coefficient of CZTS is about $13 \cdot 10^{-6}$ K^{-1}. The glass substrate used in our work is a corning soda lime (Corning product #2947) with a thermal expansion coefficient of $9.3 \cdot 10^{-6}$ K^{-1}. During the sulphurization treatment, our samples are heated from room temperature to 550°C, so that the temperature variation is about 525°C. From these values, and using $\alpha_{CZTS} = 13 \cdot 10^{-6}$ K^{-1}, we obtain $\varepsilon = 2.1 \cdot 10^{-3}$. With $\nu = 0.308$ and $E = 77.8$ GPa, the biaxial modulus is about 112 GPa and therefore the resulting thermal stress is $\sigma^{th} = 0.24$ GPa.
These calculations suggest that the mechanical stress in our sample cannot be imputed to thermal expansion effects, which can give only a small contribution.

Further investigations are necessary to clarify the origin of the observed blistering phenomenon. It could be partially due to a high compressive stress state of the CZTS films, resulting from the co-sputtering deposition conditions. However, it was also observed that blisters formation can be prevented by adding a sufficiently thick buffer layer of ZnS between molybdenum and CZTS. In Table 20, the precursor SP44 has been grown using the same conditions of SP43, but adding 2 min long sputtering deposition from the single ZnS target. CZTS thin films obtained from SP44 showed good adhesion, with no blistering effect. Formation of blisters has been then observed again by reducing the ZnS-buffer thickness, by reducing the buffer deposition time from 2 to 1 min.

These results show a role of the substrate nature in the blistering effect observed in our sample, suggesting a detrimental reaction between CZTS and Mo substrate: some gas evolution at the CZTS/MoS_2 interface or a reduced adhesion of CZTS on MoS_2 could be involved in the blisters formation.

Chapter V

Solar cells based on Cu_2ZnSnS_4 absorber layer: fabrication and characterization

Part of this chapter has been published in:

F. Biccari, R. Chierchia, M. Valentini, P. Mangiapane, E. Salza, C. Malerba, C.L. Azanza Ricardo, L. Mannarino, P. Scardi and A. Mittiga

“Fabrication of Cu_2ZnSnS_4 solar cells by sulphurization of evaporated precursors”
Physics Procedia 00 (2011) 1–5

A. Santoni, F. Biccari, C. Malerba, M. Valentini, R. Chierchia and A. Mittiga

“Valence band offset at the CdS/Cu_2ZnSnS_4 interface probed by x-ray photoelectron spectroscopy”
J. Phys. D: Appl. Phys. 46 (2013) 175101- 175105

M. Valentini, C. Malerba, E. Salza, M. de Luca, M. Capizzi and A. Mittiga

“Combinatorial study of co-sputtered Cu_2ZnSnS_4 thin-film stoichiometry for photovoltaic devices”,
Proceeding of 40th IEEE (2014) – Denver, Colorado

5.1 Introduction

In this chapter the main results concerning the development of CZTS solar cells produced in this work are presented.

CZTS samples were produced by sulphurization of both stacked evaporated and co-sputtered precursors. Details on the growth processes and characterization of these materials as isolated films have been presented in Chapter III and IV. The present chapter focuses on the performances of these samples as absorber layers in solar cells and it is organized in three main parts.

The first part concerns the device fabrication: the experimental set-up and the growth techniques used for the back contact, buffer and window layer deposition are described and a characterization of each material is also reported. In this part, the standard techniques used in this work for device characterization are also described.

The obtained devices were used to investigate some important issues related to CZTS technology. The front and the back interfaces were analysed to investigate possible detrimental effects limiting the device performances. The results of these studies are described in the second part of the chapter.

After these investigations, the work mainly focused on the optimization of the absorber layer. The third part of this chapter concerns the development of CZTS solar cells resulting from progressive optimization of both stacked and co-sputtered precursors. The higher control and reproducibility of the co-sputtering deposition allowed a fast optimization of the absorber layer and a rapid increase of the device efficiency has been obtained.

Part I:
Device fabrication and characterization techniques

5.2 Solar cells fabrication

Solar cells were produced according to the typical structure reported in the literature for CZTS-based devices. A pictorial scheme is shown in Figure 1.

The back contact was made by sputtering deposition of Mo thin film on a soda lime glass substrate.

CZTS absorbers were produce by two step processes in vacuum, using two different types of precursors: stacked evaporated precursors, made of ZnS, Sn and Cu, and co-sputtered precursors, obtained from simultaneous deposition of the binary sulphides (ZnS, SnS and CuS). For solar cell fabrication, CZTS precursors were deposited directly onto the Mo covered soda lime glass substrates, and placed into a small closed glass reaction chamber, with a stoichiometric excess of sulphur in powder. The chamber is then placed in a tube oven where the sulphurization takes place. Temperature is raised at 550°C with a heating ramp of 20°C/min under N_2 flux. After one hour, the system is naturally cooled down to room temperature. The sulphurization process is the same for both stacked evaporated and co-sputtered precursors.

An n-type CdS buffer layer is grown on the absorber front surface by chemical bath deposition. The cell is then completed by the sputtering deposition of the window layer (emitter), made of a double layer of intrinsic ZnO (i:ZnO, 100 nm) and Al-doped ZnO (AZO, 450 nm). The cell active area is then defined by mechanical scribing.

For the best solar cells, an aluminium metal contact grid and an anti-reflection coating (110 nm thick MgF_2) are also evaporated onto the n-contact, to improve the charge collection, while reducing light reflection losses.

5.2.1 Sputtering systems for back contact and window layer deposition

Different sputtering systems have been employed during this research activity, thus requiring different process optimization. During the first years the Oerlikon confocal sputtering system (see Figure 58) was equipped with only one RF power generator, which was used for sputtering deposition of both Mo back contact and the i:ZnO and Al:ZnO window layers. The confocal configuration was found to give good results in terms of thickness homogeneity and, with a proper optimization of deposition conditions, also allowed obtaining Mo layer with optimal electronic properties. However, the large target-substrate distance imposed by confocal configuration results is a slow deposition rate, which does not allow obtaining ZnO layer with optimal properties, since the film conductivity was always found to be lower than the typical values reported in the literature. After an upgrade of the sputtering system with other two power generator, the Oerlikon instruments was employed for co-99sputtering deposition of CZTS precursors and all the layers necessary for device fabrication were deposited with a different sputtering system, provided by Kenosistec and properly designed to have optimized conditions for the deposition of the materials under interest (metals and oxide materials).

The new sputtering system has a planar geometry, with targets faced to the substrate in sputter-down configuration (see Figure 59). The target-substrate distance can be tuned and can be as small as few cm, thus allowing high deposition rate.

Figure 58: Sputtering Oerlikon Leybold Univex 450B.

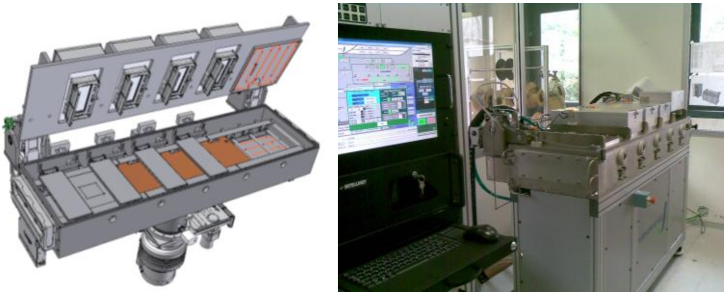

Figure 59: Kenosistec sputtering system with sputter-down planar configuration.

The system is equipped with a mechanism for substrate holder linear translation, which ensures a uniform deposition on a squared area of 6 inch x 6 inch, a substrate heater and three 8 inches long cathodes, with two power generators, one in RF and one in DC.

For sufficiently conductive materials, such as molybdenum and Al-doped ZnO, DC deposition is preferable respect to RF processes because of the higher deposition rate and the best industrial throughput. However, RF deposition is necessary for sputtering deposition of non-conductive materials, such i:ZnO, as target charging effects are prevented.

5.2.2 Mo back contact by sputtering deposition

Molybdenum layers were deposited by both RF and DC sputtering processes on soda lime glass substrates. Deposition conditions were optimized to obtain a molybdenum layer with the lowest possible sheet resistance (in order to minimize the back contact contribution to the device series resistance). At the same time, the back contact must be optimized in terms of adhesion properties both on glass substrates and with CZTS absorber layer.

It is known from the literature [130] that films deposited at low sputtering pressure show low resistivity, close to the bulk values at room temperature ($\rho_b = 5.4 \times 10^{-6}\ \Omega$ cm), whereas Mo films deposited at high sputtering pressure show higher resistivity, up to 100 times the bulk value. This correlation between deposition conditions and electrical properties is due to different film morphology, resulting from the different sputtering pressure: porous film, showing high resistivity, are indeed obtained at high pressure, as a result of multiple collisions and low kinetic energy of the sputtered species, whereas materials with more packed morphology (with low resistivity) are obtained for decreasing sputtering pressure. However, in the same work [130] it is also reported that the latter condition gives Mo films with bad adhesion on glass substrates, thus a molybdenum double layer (with a thin layer on bottom, deposited at higher pressure, and a second thicker layer deposited at lower pressure) is the typical solution adopted to optimize the back contact in terms of both electrical and adhesion properties.

Our RF sputtering process was optimized using a three step deposition. The first step is a 20min long deposition at $P \sim 2 \cdot 10^{-2}$ mbar, followed by a second step of 35min at $P \sim 2 \cdot 10^{-3}$ mbar. According to the literature results, this double layer shows a good adhesion with the glass substrate and good electrical properties, but adhesion with the CZTS films was found to be not satisfactory.

For this reason, a third deposition at $2 \cdot 10^{-2}$ mbar for 10 min was added to obtain a porous surface layer, which improves the adhesion between the back contact and the absorber layer.

A sputtering power of 300W was used and maintained constant during all the three deposition steps, which were performed with no intentional heating of the substrate.

The thickness of the final material is about 0.5 μm (corresponding to an average deposition rate of 10nm/min), with typical sheet resistance values of about 0.5 Ω/sq.

Molybdenum thin films grown by DC sputtering process were produced according to the typical bilayer structure reported in the literature, thus performing two sequential depositions at higher and lower sputtering pressure in the order. DC power was firstly fixed at 400W and different pressure conditions were testes: $1 \cdot 10^{-2}$ and $5 \cdot 10^{-2}$ mbar for the bottom layer and $1 \cdot 10^{-3}$ and $5 \cdot 10^{-3}$ mbar for the second one. The adhesion with CZTS film was found to be a critical issue, and even introducing a third porous layer (as for the previous RF processes), precursor delamination from the back contact was observed upon sulphurization.

Additional investigation showed that CZTS/Mo adhesion is very much improved when a ZnS layer is present at the interface. This could explain the better adhesion of CZTS film grown from stacked precursors, where a ZnS phase is present as a segregated layer at the bottom of the film. For homogeneous co-sputtered materials, a good adhesion was more difficult to achieve and Mo optimization was a critical issue. In addition to mechanical and microstructural properties of the back contact, the adhesion was also found to depend on CZTS composition. This problem required a more careful investigation on Mo thin films deposited with different sputtering conditions, by controlling both pressure and sputtering current.

A complete investigation on physical properties of Mo sputtered thin films is out of the aim of present work. The studies presented here only concern microstructural and electrical characterization of different samples (produced with a limited number of sputtering pressures) and were used as a guide-line to properly choose the process conditions to obtain a back contact with the required characteristics. The choice of the final deposition conditions was then based on empirically observations, to obtain satisfactory adhesion of both Mo on SLG and of CZTS on the Mo layer. Further optimization would require additional studies, based on stress measurements and adhesion tests, and a wider range of process parameters (in particular sputtering pressure) would be explored.

Electrical and microstructural properties of material obtained with different deposition conditions were investigated by resistivity measurements, SEM and XRD. Measurements in θ-2θ configuration have been used to check and identify possible preferred orientations of the Mo thin films, while texture analysis has been used for a detailed study of the microstructure, through the analysis of the pole figures (PF), measured at fixed θ/2θ by varying both φ and ψ angles (a 360° scan in φ is performed for each ψ, see Figure 60).

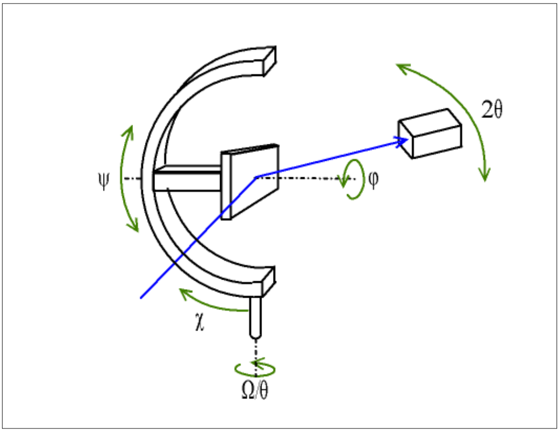

Figure 60: Scheme of the system geometry used for PFs measurements.

Ideally, an infinite number of pole figures should be used in order to reconstruct the whole orientation distribution function (ODF), i.e. the probability density of finding a crystallite with a given orientation. However, a much reduced number of pole figures can be experimentally measured. Since each pole figure is a projection of the ODF in a given direction (scattering vector direction), they can be viewed as a representative display of preferred orientation distribution. All the measurements have been performed with a Philips MRD X'Pert Diffractometer, using the CuKα radiation with a pseudoparallel beam and a polycapillary optics. This is the most indicated for the texture analysis, since this measurement set-up provides a favourable sample illumination conditions even at low 2θ and high ψ angles.

For all deposition conditions, XRD spectra acquired in θ -2θ configuration revealed a [110] preferred orientation. The (110) pole figure has been therefore chosen as the most representative for a texture characterization of our samples.

The (110) PFs of three Mo layers deposited at $5\cdot10^{-2}$ mbar using different sputtering current are compared in Figure 61. The maximum at $\psi=0$ (central pole) is in accordance with the [110] preferred orientation already identified by the θ -2θ patterns. The missing of single poles in φ (i.e. the presence of a uniform distribution in φ) in samples produced using higher sputtering current (1.6 A, panel a and 1.25 A, panel b) suggest a fibre texture, with a random distribution of the grains in the film plane. When the current is reduced to 1 A (panel c), four single poles in φ corresponding to the [110] orientation became visible, thus suggesting a stronger texture of the film produced in this condition.

Thickness, growth rate, sheet resistance and resistivity of these materials are reported in Table 21.

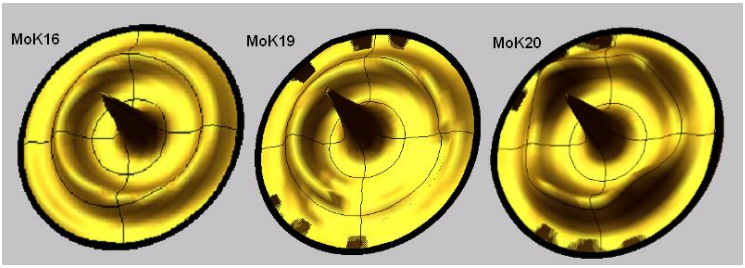

Figure 61: Comparison of the (110) Pole Figures of three Mo films produced at a constant pressure of 5 10^{-2} mbar with different sputtering current :1.63, 1.25, and 1.00 A from the left to the right side.

Table 21: Deposition conditions (power, pressure, current and deposition time) of three Mo films grown at 5.0 10^{-2} mbar, . Thickness, growth rate and resistivity are also reported.

Sample	PW (W)	P (mbar)	I (A)	Time (min)	d (nm)	Rate (nm/min)	ρ_{sh} Ω/□	ρ μΩ·cm
MoK 16	400	5.0 10^{-2}	1.63	12	1430	119	0.65	92.95
MoK 19	298	5.0 10^{-2}	1.25	12	1300	108	1.80	234
MoK 20	279	5.0 10^{-2}	1.00	12	930	78	0.49	45.57

As expected from the literature, molybdenum thin films deposited at this high pressure show too high resistivity values to give a good electrical contact.

More conductive samples were produced decreasing the sputtering pressure to $1{\cdot}10^{-2}$ mbar and $5{\cdot}10^{-3}$ mbar. The former pressure gave samples with the typical cracked-surface morphology of materials exhibiting a very high tensile stress, while a better morphology was obtained in the latter condition. The resistivity values are similar for both pressure conditions and seem mainly depend on the sputtering current. A list of samples produced at $5{\cdot}10^{-3}$ mbar is reported in Table 22.

For sufficiently high current (higher than 1.25 A), a sensible reduction of resistivity is obtained with respect to the samples produced at higher pressure (Table 21).

Mo single layers produced at low sputtering pressure were initially used as conductive substrates for precursors' deposition, in order to test CZTS adhesion after sulphurization treatment. The adhesion of the absorber layer was found to be unsatisfactory, whereas that of the back contact on SLG was found to be less critical.

Table 22: Deposition condition (power, pressure, current and deposition time) of three Mo films grown at 5.0 10^{-3} mbar. Thickness, growth rate and resistivity are also reported.

Sample	PW (W)	P (mbar)	I (A)	Time (min)	d (nm)	Rate (nm/min)	ρ_{sh} Ω/□	ρ μΩ·cm
MoK 28	509	5.0 10^{-3}	1.60	12	1450	121	0.13	18.85
MoK 30	458	5.0 10^{-3}	1.45	12	1300	108	0.12	15.6
MoK 14	400	5.0 10^{-3}	1.26	12	1190	99	0.2	23.8
MoK 24	305	5.0 10^{-3}	1.00	12	880	73	0.7	61.6

Better results were obtained using a bilayer structure. After some experiments, the back contact was optimized by growing a first Mo layer using the same conditions of the sample MoK20 ($P=5{\cdot}10^{-2}$ mbar; I= 1 A), which was used as a seed to grow a second layer at P $=5{\cdot}10^{-3}$ mbar and I= 1 A, corresponding to the deposition condition of the most conductive sample (MoK30).

The final film shows a resistivity of about 13 μΩcm and good adhesion properties with both SLG and CZTS. The (110) PF of the final bilayer, reported in Figure 62, reveals a [110] preferred orientation, with a similar but less strong texture respect to the seed (MoK20), as revealed by less visible poles in φ.

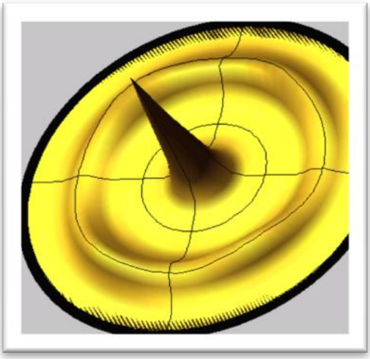

Figure 62: (110) PF of a Mo bilayer deposited using the sputtering conditions described in the text.

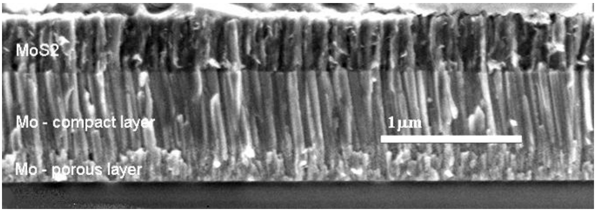

Figure 63: Cross section of a Mo bilayer grown by the DC sputtering process described in the text.

In the cross section of the same bilayer (Figure 63), the two different morphologies depending on the deposition conditions can be identified: a porous structure is visible at the Mo/SLG interface, while a more compact structure is found for the second and thicker layer. The thin surface layer visible on top has been identified as MoS_2, resulting from Mo partial sulphurization during the precursor sulphurization treatment. Investigation on back contact sulphurization and possible effects on CZTS/MoS_2 adhesion properties and band alignment are discussed in section 5.4.

5.2.3 CdS buffer layer by CBD

Cadmium sulphide is a n-type semiconductor with a direct gap of 2.42 eV [30] at room temperature and electron affinity 4.5 eV [147]. This material is commonly used as buffer layer for CIGS and CdTe solar cells and its use was also extended to CZTS

device technology. CdS has several roles: 1) optimization of band alignment between CZTS and ZnO window layer [43]; 2) reduction of surface defect density at the interface [152], which also implies a 3) longer lifetime of charge carriers [94]; 4) protection of absorber layer surface during the sputtering deposition of ZnO [43].
Among the possible deposition techniques, chemical bath deposition (CBD) is the most used, being not expensive and giving CdS films with the best results in terms of device efficiency. CBD of CdS is a process based on thiourea ($SC(NH_2)_2$) hydrolysis in an aqueous alkaline solution containing a cadmium salt. Ammonium hydroxide (NH_3) is generally used as complexing agent, added to the bath in order to control the concentration of Cd^{2+} free ions (according to the complex ion dissociation equilibrium constant), thus obtaining a controlled precipitation of cadmium sulphide.
CdS forms as result of the following chemical reactions:

1. $\mathrm{Cd^{2+} + NH_3 \rightarrow [Cd(NH_3)_4\,]^{2+}}$

2. $\mathrm{SC(NH_2)_2 + OH^- \rightarrow SH^- + H_2O + CH_2N_2}$
$\mathrm{SH^- + OH^- \rightarrow S^{2-} + H_2O}$

3 $\mathrm{[Cd(NH_3)_4\,]^{2+} + S^{2-} \rightarrow CdS + 4\,NH_3}$

The formation of complex ions (1) prevents $\mathrm{Cd(OH)_2}$ to precipitate.
CdS nucleation start as the ion density product $[Cd^{2+}][S^{2-}]$ exceeds the CdS solubility product ($Ksp^{(CdS)} = 10^{-25}$ [25]). Depending on whether $[Cd^{2+}][S^{2-}]$ product is only slightly or much larger than $Ksp^{(CdS)}$ value, CdS nucleation takes place at the substrate surface (heterogeneous reaction), forming a continuous film, or in the bulk of the solution (homogeneous reaction), with formation of colloids giving a porous material.

CdS physical properties (morphology, optical and electrical properties) are strongly influenced by the deposition conditions, such as composition, temperature and pH of the solution. A careful control of these process parameters is therefore important to obtain a good reproducibility.
Different processes are reported in the literature for CBD of CdS [72, 71, 100, 91], mainly differing for the nature of Cd source ($CdSO_4$, CdI_2, $Cd(CH_3COO)_2$) and for reagents' concentration.

In our work, CdS thin films were deposited by chemical method trying different procedures reported in the literature [72, 91]. The process was optimized using a bath with a composition similar to that reported in [91] (in which thiourea and ammonia concentrations are lower than those used in other tested procedure [72]) and was found to give slow nucleation reaction resulting in compact and homogeneous CdS films.

Ammonium hydroxide (25%, 27.6ml) and CdI_2 (30mM) aqueous solution (10ml) are added to 150 ml of water, pre-heated at 55°C (10°C lower than the reference work [91]). Substrates are immersed vertically using a holder, thus reaching thermal equilibrium with the solution, which is continuously stirred during all the process. Thiourea (1.09 g) is added to the bath, together with additional water to get the solution to 200 ml. Using the molar masses $M(CdI_2)$=366.22 g/mol, $M(CH_4N_2S)$=76.12 g/mol and $M(NH_3)$=17.00 g/mol (which corresponds to 13.29 mol/l in a 25% aqueous solution), the reagents' concentration in the final solution (200ml) are: $M(CdI_2) = 1.5$ mM, $M(CH_4N_2S) = 71.6$ mM, $M(NH_3) = 1.83$ M. Soon after the introduction of thiourea, the reaction starts and the initial transparent solution becomes progressively light (in 2 min), bright and dark yellow (after 20 min). For higher temperature, nucleation reaction proceeds too quickly and a turbid solution is obtained in few minutes, thus giving poor quality porous films. After 20 minutes of deposition, the samples are extracted from the bath, rinsed in water and ultrasonically treated in a NH_3 water solution (with volume concentration 1:10). The samples are then washed in water and dried in air under N_2 flux.

CdS samples grown with the described method are bright yellow compact films, with a good adhesion on both CZTS substrates and soda lime glass. Film thickness resulting from profilometer measurements and SEM observations (Figure 64) is about 70 – 100 nm, which is the typical value reported in the literature for CdS buffer layers.

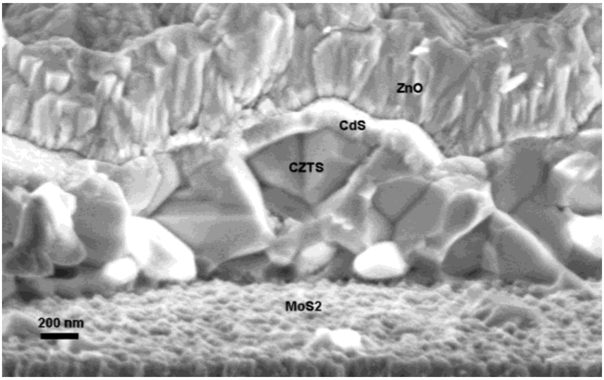

Figure 64: SEM cross section of a CZTS solar cell. A CdS buffer layer of about 70 - 100 nm can be identified.

Taking into account the band gap energy value (2.4 eV), thicker CdS films have to be avoided to reduce as much as possible the absorption in the violet-ultraviolet region of the solar spectrum. At the same time, the buffer layer has to be sufficiently thick to allow a conformal coverage of the absorber layer.

The transmittance spectra of three CdS films with different thickness are reported in Figure 65: the thinner films (40 and 70 nm) were obtained using the method described in the text, with deposition times of 10 and 20 min, whereas the thicker sample (120 nm) was grown using the process reported in [72]. Despite the difference due to interference fringes effect, an increasing optical absorption is clearly visible in the sub-gap energy region (λ < 500 nm) as the film thickness increases.

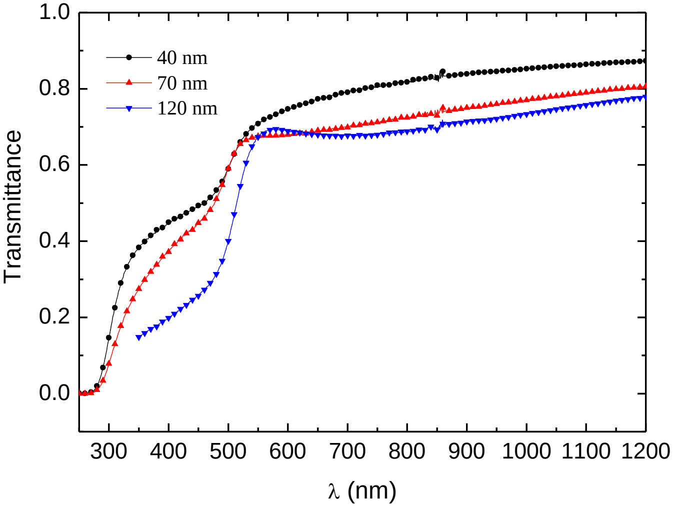

Figure 65: Transmittance spectra of three CdS samples: 40 and 70 nm thick films were deposited using the procedure described in the text with 10 and 20 min deposition times, whereas the thicker sample (120 nm) was grown using the procedure reported in [72].

CdS films were also characterized in terms of microstructure by means of grazing incidence XRD measurements with an incident angle of 0.8°. This configuration is convenient in case of very thin samples, as a larger area can be analyzed with respect to the standard θ -2θ geometry, thus enhancing the diffracted intensity.

CdS can exist in both hexagonal (wurzite) [45, 117] and cubic (zincblende) [110, 15] structure, depending on the growth technique and deposition conditions. For CBD, hexagonal, cubic or mixed structures [63, 79] are reported in the literature [92, 27, 83, 25], depending on the composition, temperature and pH of the bath. Figure 66 shows a typical XRD spectrum of one of ours CdS film; diffraction peak positions match the CdS face-centered cubic structure (XRD card #75-581).

The sheet resistance was found to be higher than the upper limit of the four probe instrument used for sheet resistance measurements (about 300 KΩ/sq). For a 70nm thick film, this corresponds to a resistivity higher than 2 Ωcm.

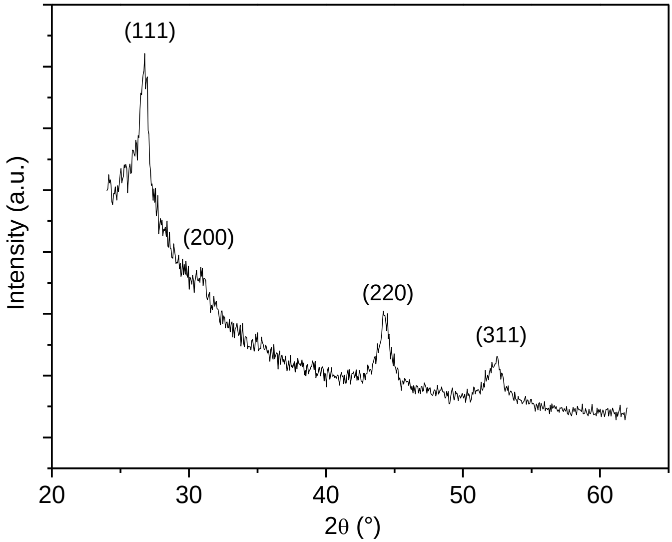

Figure 66: Grazing incidence (0.8°) XRD spectra of a typical CdS film. The diffraction peaks were identified according to the XRD card #75-581.

5.2.4 Window layer: i:ZnO and AZO

ZnO is a widely studied cheep and non toxic material, with a variety of technological applications. In the photovoltaic field, ZnO is widely used as transparent and conductive material, suitable for window layer in solar cells. It is a n-type semiconductor with a wide (3.4 eV) energy gap [65], which results in high transparency in all the visible range. The n-type conductivity has been imputed to oxygen vacancy (V_O) or interstitial Zn atom (Zn_i) intrinsic donor defects, even though some controversies on the nature of the defects responsible for the n-type conductivity arise from recent works and calculations [65, 64, 85].

ZnO films with high conductivity can be obtained upon n-doping using third group elements replacing Zn^{2+} ions. Aluminum is the most used dopant, with typical concentration of 2 wt.%. Al doped ZnO (AZO) with resistivity values as low as $2\cdot10^{-4}$ Ωcm and good transparency (with transmittance higher than 85%) are reported in the literature [171].

The typical ZnO crystal structure is the hexagonal wurzite. The film usually grow with a (001) preferred orientation, with the c-axis perpendicular to the substrate surface. Among the several possible techniques which can be used to grown ZnO films, sputtering deposition is the most commonly used because of its advantages in terms of control of crystalline orientation, high packing density, homogeneity and good adhesion of the grown material [111].These properties can be controlled by varying the sputtering power and pressure (influencing the deposition rate) and the substrate temperature, which can be raised to improve the grain growth and the doping efficiency in case of doped materials.

In our work the window layer was deposited by using sputtering deposition processes, according to the widely reported double structure i:ZnO/AZO.

The first intrinsic layer, in direct contact with CdS buffer, is usually employed in the literature to reduce possible shunt effects in solar cells. In the first stage of our research, both intrinsic and doped zinc oxide films were grown by RF magnetron sputtering using the Oerlikon UNIVEX450B sputtering system (with confocal geometry), equipped with an i:ZnO and an Al:ZnO (with 2 wt.% of Al_2O_3) targets.

A first thin layer (about 100 nm) of i:ZnO was deposited for 20 min with a RF power of 150 W at $1\cdot10^{-2}$ mbar, heating the substrate at 150°C.

The optimized deposition conditions for the AZO layer were the following: RF power 300 W, sputtering pressure $3 \cdot 10^{-3}$ mbar , substrate temperature 200 °C, deposition time 90 min. Higher temperatures allow further resistivity reduction, but, as observed in chalcopyrite and a:Si-H solar cells, they could be detrimental for device performances.

The films were about 1µm thick with a sheet resistance of 40 Ω/sq, corresponding to a resistivity of about $4 \cdot 10^{-3}$ Ω cm. Hall measurements revealed a mobility of about

10 cm^2/(V·s) while good transparency resulted from spectrophotometric measurements. A typical transmittance spectrum is reported in Figure 67, showing transmittance higher than 80% in the visible range. The transmittance decrease in the infrared region is due to free carrier optical absorption. The θ-2θ XRD spectra reveal a (001) preferred orientation, showing only the (002) reflection (at 2θ about 34.4°) of the wurzite hexagonal structure (PDF#36-1451).

These films show suitable properties for their use as window layers in heterojunction solar cells. However, it has to be pointed out that for anomalous target overheating, AZO deposition were typically performed lowering the sputtering power down to 200W, using doubled deposition time, the new conditions resulting in worse film conductivity compared to the optimal value.

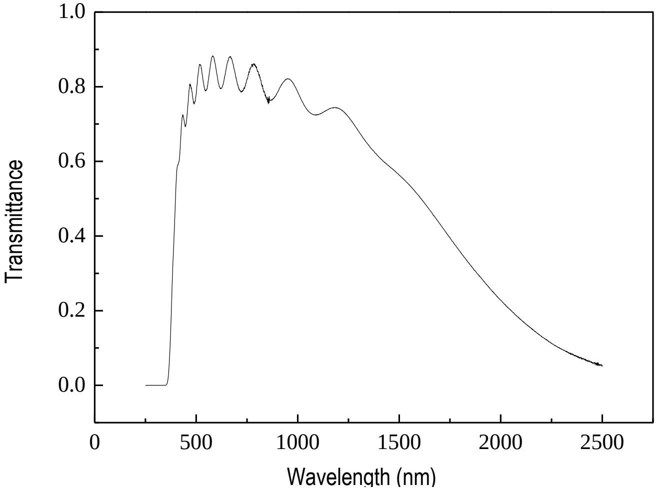

Figure 67: Transmittance spectrum of a typical AZO film deposited on soda lime glass.

Window layers with higher conductivity were obtained using the planar sputtering system provided by Kenosistec (target-substrate faced configuration).

The intrinsic ZnO layer is deposited by RF sputtering using a ZnO target whereas a DC sputtering process, with a ZnO target containing a 2 wt% of Al_2O_3, is used for AZO deposition.

Substrates are pre-heated in the heating chamber by setting the heating resistance temperature at 270°C, which corresponds to a substrate temperature of about 150°C. Further (not intentional) heating is expected under ion bombardment during the sputtering deposition.

The intrinsic layer was deposited with an argon sputtering pressure of $5 \cdot 10^{-3}$ mbar, using a RF power of 200 W.

AZO films were firstly deposited directly onto soda lime glass substrates. The deposition conditions were optimized by lowering the Ar sputtering pressure to $8 \cdot 10^{-4}$ mbar and varying the sputtering power from 350 to 600 W. As shown in Figure 68, except for the first point corresponding to 350 W, the AZO film resistivity shows a decreasing trend as the sputtering power increases from 400 to 600 W. To avoid target overheating and possible surface sample damage, DC power was fixed to 450 W, corresponding to a resistivity value of about $1.8 \cdot 10^{-3}$ Ωcm.

With these process conditions, i:ZnO/AZO bilayers with thickness of about 550 nm show a sheet resistance of about 30 Ω/sq, corresponding to a resistivity of $1.6 \cdot 10^{-3}$ Ωcm. The slight improvement of the conductivity in presence of the i:ZnO layer has to be likely imputed to a better AZO morphology when grown on a i:ZnO seed, deposited at low sputtering power.

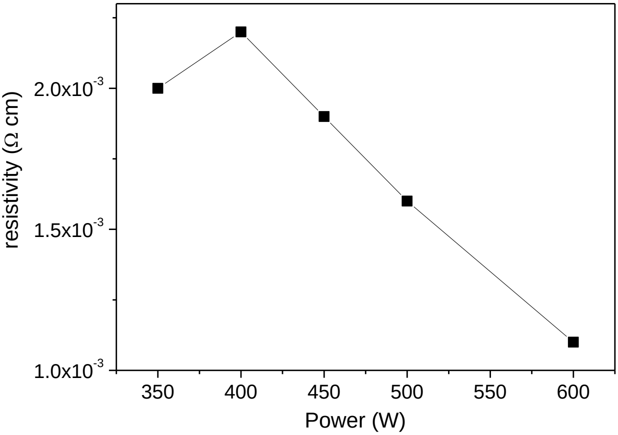

Figure 68: Resistivity variation of AZO thin films grown by DC sputtering on SLG at $8 \cdot 10^{-4}$ mbar with increasing sputtering power.

5.2.5 Assembled solar cell stack

Mo thin films, CdS and i:ZnO/AZO layers described in previous paragraphs were used as back contact, buffer and window layers, respectively, for CZTS solar cells fabbrication. In Figure 69, a picture of a typical device is reported. In the image, seven small solar cells (with area of 0.1, 0.2, 0.5 and 1 cm^2) are obtained from the same sample. The active area of each single cell is defined by mechanical scribing. The aluminum grid deposited by thermal evaporation on the top (n-) contact is also visible. The best devices were also covered by an MgF_2 anti-reflection coating, not visible in the picture.

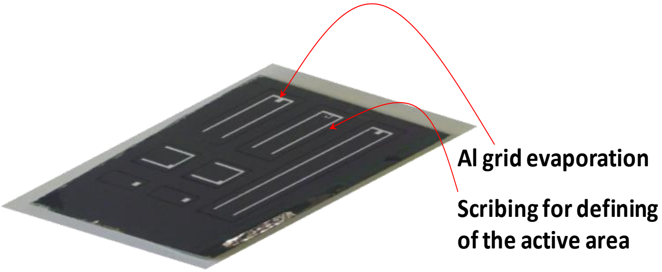

Figure 69: Picture of a CZTS solar cell produced in this work.

5.3 *Solar cells characterization techniques*

5.3.1 J-V characteristics under dark and light conditions

According to the standard diode equation, the current-voltage (I-V) characteristic of a single-junction solar cell under illumination can be written as the linear superposition of the dark characteristics of the cell and the photogenerated current [48]:

$$I(V) = I_0\left[exp\left(\frac{qV}{nkT}\right) - 1\right] - I_L, \tag{1}$$

where I_L is the photogenerated current, I_0 is the reverse saturation current, q is the elementary charge, k the Boltzmann constant, T the absolute temperature and n the ideality factor, which is 1 for ideal p-n junction (where the current is dominated by diffusion mechanism), whereas n=2 when the current is dominated by recombination phenomena in the space charge region.

Under dark conditions, there is no contribution from the photogenerated current and the resulting diode characteristic curve is reported in Figure 70.

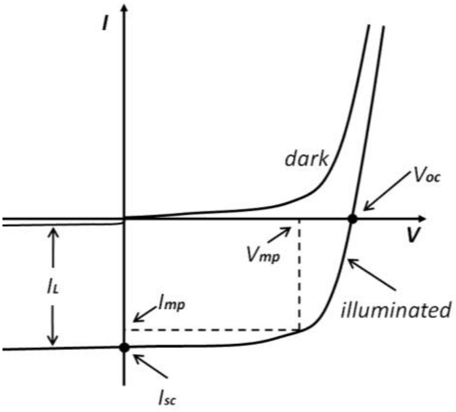

Figure 70: JV characteristic curves of a p-n solar cell under dark and light conditions [48].

The illuminated characteristic, reported in the same figure, is merely the dark curve shifted down by a current I_L. This gives a region in the fourth quadrant in which the power can be extracted from the cell.
Solar cell outputs are usually characterized using four main parameters:

- The short circuit current: I_{sc} , which is the current that can be reached under illumination when the device is short-circuited. Ideally, this parameter is equal to the light-generated current under illumination (I_L).

- the open-circuit voltage V_{oc} , which is the voltage established under illumination when the circuit is not closed. The V_{oc} can be deduced from eq. (1) with the condition $I = 0$:

$$qV_{oc} = nkT \;\; ln\left(\frac{I_L}{I_0} + 1\right) \tag{2}$$

  The reverse saturation current has to be as small as possible to maximize the Voc.

- the Fill Factor (FF), which is a measure of the “squareness” of the solar cell characteristic, and it is defined as:

$$FF = \frac{V_{mp} I_{mp}}{V_{oc} I_{sc}}, \tag{3}$$

where $\left(V_{mp}, I_{mp}\right)$ is a particular operating point, corresponding to the maximum power output, P_{mp} :

$$P_{mp} = V_{mp}\, I_{mp} = V_{oc}\, I_{sc}\, FF \tag{4}$$

Graphically, FF corresponds to the area of the dashed rectangle in Figure 70. The higher the FF, the higher the power that can be extracted from the cell.

- the energy conversion efficiency η is defined as

$$\eta = \frac{P_{mp}}{P_{in}} = \frac{V_{oc}\, I_{sc}\, FF}{P_{in}}, \tag{5}$$

where P_{in} is light incident power.

Actual devices are less efficient than ideal solar cells. Recombination of photogenerated electron-hole pairs in the bulk and at surfaces are responsible for both I_{sc} and V_{oc} losses, thus reducing the FF, too. These mechanisms are taken into account in eq. 1 by the introduction of the ideality factor n. Moreover, the resistance of both the semiconductor materials and metal contacts give rise to a parasitic series resistance (R_s) associated to the solar cell. In addition, leakage across p-n junction, due to the presence of crystal defects, impurities, precipitates, create current shunting paths, which can be described as a shunt resistance R_{sh}.
Actual solar cells can be therefore described using a simple equivalent circuit reported below (Figure 71).

Using this model, the current density – voltage (J-V) characteristic curve can be written as:

$$J(V) = J_0 \left[exp\left(\frac{q(V - JR_s)}{nkT} \right) - 1 \right] + \frac{V - JR_s}{R_{sh}} - J_L \tag{6}$$

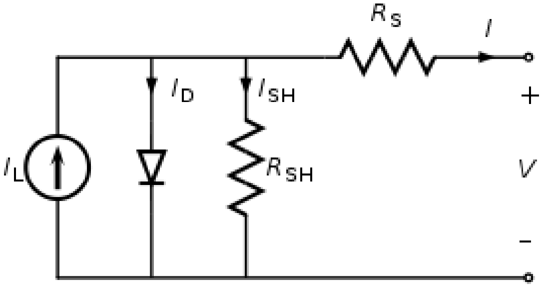

Figure 71: equivalent circuit of a solar cell.

This expression has been used in this work to fit the J-V characteristic curves measured under dark conditions (with $J_L = 0$) and the dark parameters J_0, R_s, R_{sh}, n has been obtained.

Light J-V measurements were performed under standard conditions T=25°C and AM1.5G illumination (100 mW/cm^2), using a class-A Wacom solar simulator.
The light parameters V_{oc}, J_{sc}, FF have been obtained from the J-V curves by numerical interpolation (see Figure 70).

5.3.2 External Quantum efficiency

External Quantum efficiency (EQE) is defined as the ratio of the number of charge carriers collected by solar cell to the number of incident photons of a given energy.

$$EQE = \frac{\#\, electrons/sec}{\#\, photons/sec} = \frac{current\ /electron\ charge}{light\ power/energy\ of\ 1\ photon}$$

Quantum efficiency therefore gives the response of a solar cell to the different wavelengths of the light shining on the device.
Ideally, if all the photons with energy higher than the semiconductor bandgap (Eg) are absorbed and all the photogenerated carriers are collected, then the EQE value is 1 and EQE becomes zero when the energy of the incident photon becomes smaller than Eg. The ideal curve is reported in Figure 72.
Because of both optical losses (such as transmission through the cell and reflection of light away from the cell) and recombination phenomena, in the actual devices EQE value is lower than 1 and shows a shape similar to that reported in Figure 72.
The deviation of the experimental curve compared to the ideal behaviour is related to different mechanisms: for example, low value of EQE in the highest energy region

(blue-region) can suggest recombination phenomena at the front interface or parasitic absorption from the upper layer of the device (such as buffer or window layer), whereas in the energy region where light absorption occurs deeper in the active material (typically the green-region), values of EQE lower than 1 suggest a low diffusion length of minority carriers, which recombine before they are collected. Low EQE in this region, therefore, suggests the presence of traps or recombination centres, thus revealing a poor quality of the absorber layer.

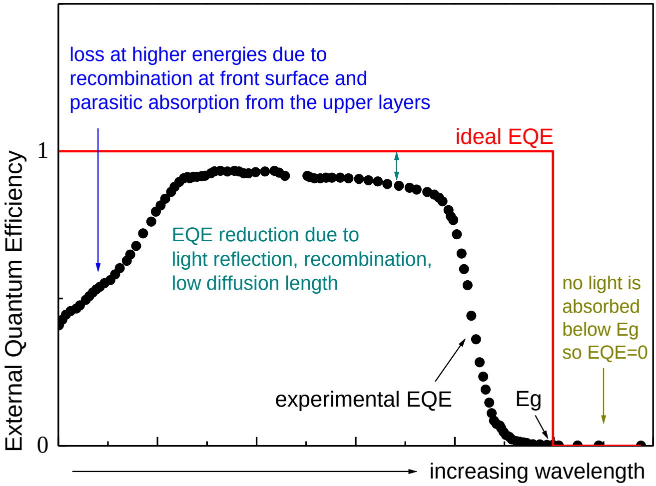

Figure 72: Typical EQE curves of a solar cell.

EQE measurements are therefore useful to identify the possible loss mechanisms in a real device and have been used in this work to evaluate the quality of our CZTS films as absorber layers.

EQE measurements have also been used to evaluate the short circuit current. Indeed, by definition of EQE, its integral over the whole incident light spectrum corresponds to the total current produced by the cell under illumination:

$$I_{sc} = q \int_{0}^{\infty} EQE(\lambda) \frac{\lambda}{hc} P_{in}(\lambda) d\lambda \qquad (7)$$

Part II: Investigation on the back and front interface

5.4 Back contact investigation

One of the most important issues for the development of CZTS solar cells is the optimization of the back contact.

In addition to electrical problems related to a possible formation of a Schottky barrier at CZTS/MoS_2 interface [160], the formation of a MoS_2 interfacial layer could also lead to adhesion problems, depending on its crystallographic orientation respect to the substrate plane. Indeed, MoS_2 is known to be a very good lubricant, due to its layered crystal structure, formed by stacking “sandwiches” consisting of a layer of transition metal (Mo) between two layers of chalcogen (S). There is strong covalent bonding within the sandwiches but weak (van der Waals’) bonding between them. The weak bonding between sandwich layers results in very low shear strengths (low friction) within the films in the direction of sliding [166].

When the basal planes are parallel with the plane of the contacting surface (corresponding to the c-axis perpendicular to the substrate plane), MoS_2 polycrystalline thin films exhibit lubricant properties, which may affect the adhesion of CZTS absorber layer on the back contact.

In our work, we investigated on the possible formation of a MoS_2 spurious phase at the CZTS/Mo interface in our devices.

Possible detrimental effects on the adhesion properties between CZTS absorber layer and the back-contact were investigated by XRD, looking at crystallographic orientation of the MoS_2 interfacial layer. The back contact electrical behaviour has been also investigated, looking at possible band-alignments at the back interface, depending on the conduction type (p- or n-type) of the MoS_2 phase.

5.4.1 Identification and characterization of MoS_2 interfacial layer at CZTS/Mo back interface

A first evidence of MoS_2 formation was obtained by XPS measurements on Mo substrates after the removal of the deposited CZTS film [67]. These measurements showed a Mo/S ratio equal to 1/2 on the surface.

In our work, the formation of a MoS_2 phase was checked by grazing incidence XRD measurements (with incidence angle = 1.6°) on completed cells and on the Mo substrate after stripping the cell using adhesive tape. The XRD spectra obtained before and after the cell removal are shown in Figure 73. In the case of the cell, the diffraction peaks of the MoS_2 are masked by the CZTS and CdS signals. After the cell removal the (100) reflection of the MoS_2 can be clearly seen (at 2θ ~ 33°) while the (110) peak cannot be easily observed since it is superimposed to the (200) peak of the Mo. The MoS_2 peaks corresponding to the planes perpendicular to c-axis are not detectable. This means that the MoS_2 layer grows with its c-axis parallel to the substrate surface. This orientation is not harmful for the absorber adhesion, as the direction of sliding is perpendicular to the CZTS/MoS_2 contact surface. This is also the orientation which gives the best results in CIGS cells and it is in agreement with previous work on the low temperature sulphurization of Mo [52].

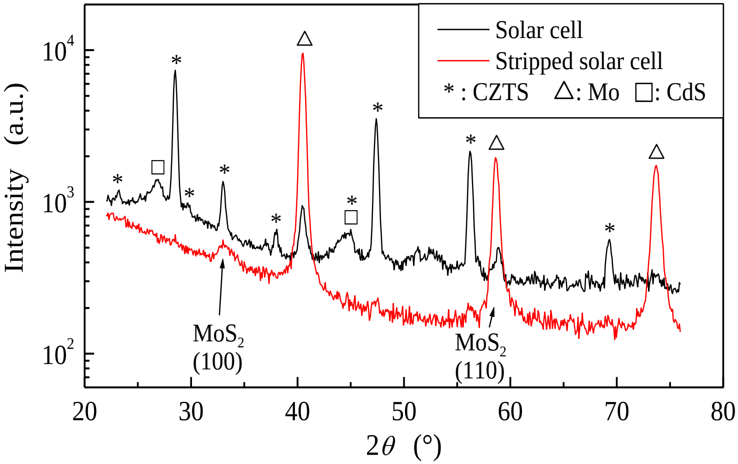

Figure 73: Grazing incidence XRD spectra of a CZRS solar cell and of ots Mo substrate after the cell removal.

5.4.2 Simulated band alignments at CZTS/MoS_2/Mo back contact

Since the Cu(In,Ga)Se2 solar cells have reached an efficiency of 20% using a Mo back contact, it is natural to make a comparison with CZTS. The comparison is facilitated by the fact that, according to ab-initio calculations [20], the CuInSe2 has the valence band maximum (VBM) only 70meV higher than CZTS. Therefore in both cases the VBM should lie around 5.5 eV below the vacuum level and this explains why a simple Mo contact with a work function of 4.6 eV is not able to give an ohmic contact while more noble metals (as platinum, gold and nickel) do [93]. It is also well known that, in the cells based on selenides, the Mo is able to give an ohmic contact due to the formation of a thin MoSe2 layer [1]. Using UPS, IPES and XPS it has been shown [7] that the valence bands of CIGSe and MoSe2 are well aligned: according to the authors this alignment explains the good properties of the contact. MoS_2 and $MoSe_2$ have very similar band parameters. Both have an indirect gap of similar values: Eg (MoS_2) = 1.17 eV and Eg (MoSe2) = 1.06 eV [75]. Their photo-threshold (i.e. the difference between the vacuum level and the VBM) are 5.6 eV and 5.5 eV for MoS_2 and MoSe2 respectively [138], quite similar to that of CIGSe and CZTS. Using the simple electron affinity rule, only a small valence band offset of 0.1 eV should be present at the CZTS/MoS_2 interface, in good agreement with measurements performed on CIG(S,Se) solar cells [7]. It seems likely that a good ohmic back contact can be obtained if a MoS_2 layer with suitable properties forms at the interface. This is supported by the fact that the cells based on CuInS2 have reached FF values up to 74%.

What happens in CZTS? We have to note that the mere formation of MoS_2 does not assure an ohmic contact. According to our simulations, the best situation is to have highly p-type MoS_2 which gives a band profile with a Schottky barrier at the Mo/MoS_2 interface as that shown in Figure 74(a) and in [160]. In the case of high doping, the barrier can be crossed by tunnelling. If instead the MoS_2 is n-type and considering that the work function of MoS_2 and Mo are in that case almost equal, the barrier is placed at the CZTS/MoS_2 interface as shown in Figure 74(b). This band profile is quite different from the one proposed in [7], due to a large difference in CZTS Fermi level used here and in the cited work.

Where is located the Fermi level in our samples? Transmission Line Measurements (TLM) have shown that the highest resistivity value (ρ) of our samples is about $2 \cdot 10^4$ Ωcm. From Hall effect measurements we found an upper limit for the hole mobility of $1 cm^2/(Vs)$. Using a hole effective mass of 0.48 *m_0* (where *m_0* is the free electron mass) for holes in the upper valence band [114], the corresponding density of state is given by:

$$N_V = 2\left(\frac{2\pi m_h K_B T}{h^2}\right)^{3/2} = 8.3 \cdot 10^{18}\ \mathrm{cm}^{-3}$$

Using the resistivity and mobility values reported before and using the simple equation:

$$p = N_v\, e^{-\left(\frac{E_F - E_V}{K_B T}\right)} < (q\mu\rho)^{-1},$$

we found that in our sample the Fermi level distance from the valence band is less than 265 meV. On the contrary, the CZTS Fermi level used in [7], is surprisingly far (0.9 eV) from the valence band.

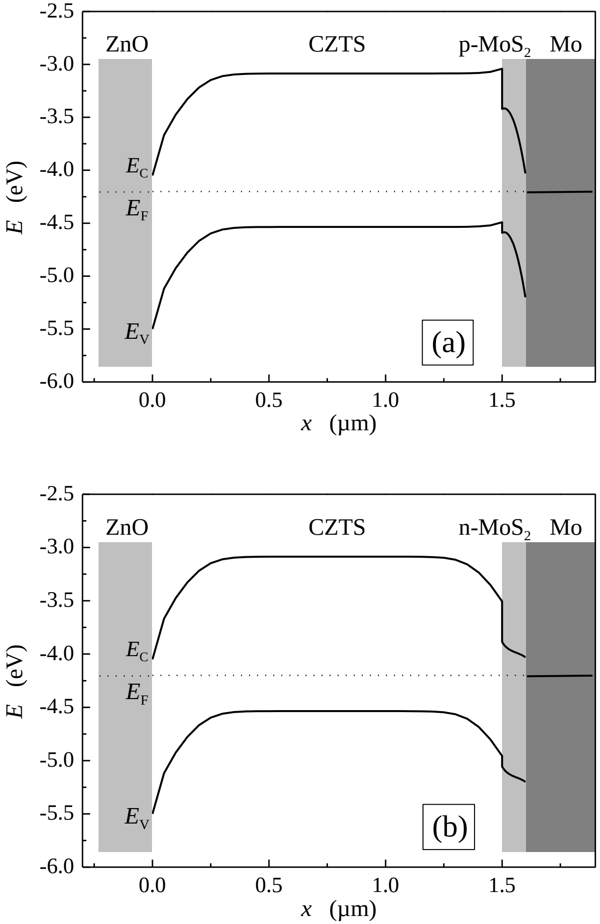

Figure 74: Simulated band profiles in a CZTS solar cell with a p-type (a) and n-type MoS_2 layer on the back interface.

5.5 *Valence band offset at the CdS/Cu_2ZnSnS_4 interface probed by x-ray photoelectron spectroscopy*

The determination of the band alignment at the CZTS/CdS interfaces is a crucial point for understanding and optimizing the cell properties.

In particular, an increased interface recombination, induced by a not-optimal cliff-like conduction band offset (CBO) at the front interface could be one of the reasons for the Voc limitation, typically found in CZTS solar cells.

With this band alignment, the conduction band minimum of the CdS buffer would be located below that of the CZTS and this is equivalent to an interface band gap reduction which favours the recombination processes. A spike-like CBO would be preferable [98]. To the best of our knowledge, only two experimental papers have addressed the band offset issue on CZTS so far. Bar et al [9] determined the valence band (VB) and the conduction band (CB) alignment at the CdS/CZTS interface by ultraviolet photoelectron spectroscopy (UPS) and inverse photoelectron spectroscopy (IPES). They find a 0.33 eV cliff-like CBO and a 1.19 eV valence band offset (VBO) for a non-etched absorber which is reduced to 0.91 eV upon KCN etching. On the other hand, Haight et al. [53] measured by femtosecond laser, pump–probe UPS, a 0.54 eV VBO value, thereby reporting a spike-like CBO. From the theoretical point of view, Chen et al [21] predicted by first-principles calculations a CdS/CZTS VBO of 1.01 eV with a negligible (0.09 eV) cliff-like CBO. Photoelectron emission spectroscopy with tunable synchrotron radiation and/or with fixed photon energy (x-ray photoelectron spectroscopy-XPS, UPS) has been proved to be a powerful technique to study band offsets in semiconductors [14].

In our work, we have studied the band alignment at the CdS/CZTS interface by XPS core-level spectroscopy and XPS VB spectroscopy. In particular, the VBO has been obtained directly from VB data analysis (direct method) and also indirectly using information from core-level data [77, 158, 11] (indirect method).

5.5.1 Experimental details

The sample was obtained by electron beam evaporation of a stacked precursors made of ZnS, Sn and Cu on a soda lime glass substrate, covered by an RF sputtered Mo thin films. The chemical composition of the precursor is Zn-rich because it is commonly accepted that this stoichiometry gives the best performances of final photovoltaic devices. The CZTS layer was successively synthesized by sulphurization of the precursor in a tube oven under a N_2 flux for one hour at 550°C. Finally, the CdS/CZTS interface was obtained by depositing a 70 nm thick CdS layer on CZTS by chemical bath deposition (see section 5.2.3). XRD and Raman spectra (not shown here) didn’t give any evidence of spurious phases. This does not exclude the possibility of some ZnS segregation since the ZnS XRD peaks are superimposed to those of CZTS and (with the 532 nm wavelength excitation source used for Raman measurements) the ZnS Raman signals are quite weak. A XPS quantitative analysis is performed to quantify the concentration of the different elements: it turns out that the film is stoichiometric for most of its thickness except a narrow region near the CZTS/Mo back contact where a Zn excess is detected (see Figure III-10). This behaviour is commonly reported in almost all papers on CZTS solar cells and it was confirmed also by glow discharge-optical emission spectroscopy (GD-OES) data. XPS data were acquired in an ultra-high vacuum system operating at 4×10 −8 Pa base pressure. It is equipped with a VGAlKα monochromatized x-ray source and a CLAM2 hemispherical analyser working at constant 20 eV pass energy mode and calibrated according to [5].

The total energy resolution resulted to be 0.7 eV as obtained from the fit of the Fermi edge of a clean Au sample. The VB binding energy (BE) was referred to the position of the Fermi level measured on a clean Ta strip in good electrical contact with the sample. In order to reach the CdS/CZTS interface, the samples were mildly sputtered with 1 keV Ar ion energy. A careful investigation of the behaviour of the main XPS core-level intensity ratios as a function of sputtering time has allowed us to exclude any preferential sputtering effects. No change in the Cd $3d_{5/2}$, S 2p, Cu $2p_{3/2}$, Zn $2p_{3/2}$, Sn $3d_{5/2}$ core-level lineshapes, relative intensities and BE positions was detected by XPS after sputtering cycles on the CdS and CZTS surfaces, indicating that Ar^+ bombardment did not induce any observable surface modifications.

5.5.2 Results and discussion

In the indirect method, according to [77], the VBO can be calculated by the formula

$$VBO = E^{b}{}_{VB} - E^{a}{}_{VB} + V_{bb}\,, \tag{8}$$

where $E^{a}{}_{VB}$ and $E^{b}{}_{VB}$ are the energy positions of the VB edges of species ‘a’ (CZTS) nd ‘b’ (CdS) while Vbb is the band bending which is calculated by the well-known formula

$$V_{bb} = \left(E^{a}{}_{CL} - E^{a}{}_{CL}(i)\right) + (E^{b}{}_{CL}(i) - E^{b}{}_{CL})\,, \tag{9}$$

where $E^{a}{}_{CL}$ and $E^{b}{}_{CL}$ are the core-level energies of two selected elements in the bulk of material ‘a’ and ‘b’ and $E^{a}{}_{CL}(i)$ and $E^{b}{}_{CL}(i)$ are the same core-level energies measured at the interface. In the present case, material ‘a’ can be chosen from Cu, Zn and Sn and material ‘b’ is Cd. The band bending is calculated assuming the BE below the Fermi edge negative.

According to the configuration used for our calculations (i.e. CZTS/CdS interface), VBO (CBO) results negative if the valence (conduction) band edge of CdS is lower than that of CZTS.

Figure 75 shows the band bending values calculated at different thicknesses of the CdS/CZTS interface using the core-level BEs of Cd 3d$_{5/2}$, Cu 2p$_{3/2}$, Zn 2p$_{3/2}$ and Sn 3d$_{5/2}$. While the values of $E^{a}{}_{CL}$and $E^{b}{}_{CL}$ are always the same, $E^{a}{}_{CL}(i)$ and $E^{b}{}_{CL}(i)$ are measured for each different thickness where both the CdS and CZTS signals are present.

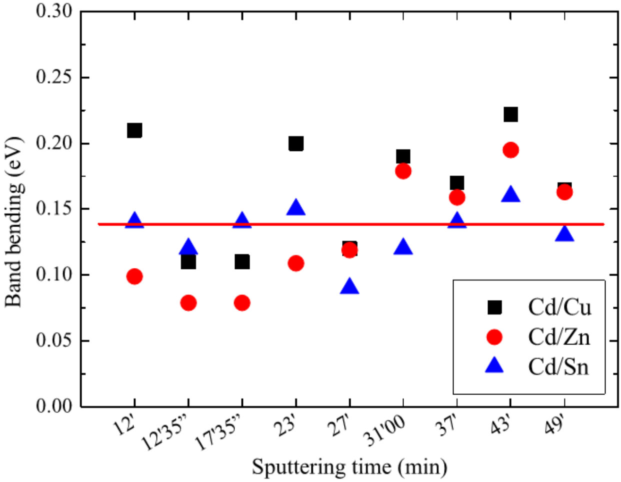

Figure 75: Band bending as a function of sputtering time. The band bending is shown for three data sets: Cd/Cu (filled squares), Cd/Zn (filled circles) and Cd/Sn (filled triangles). A sputtering time of 12 min corresponds to 14% CZTS, while a sputtering time of 23 min corresponds to 75% CZTS. The horizontal solid line indicates the total average of(0.14±0.10)eV. For further explanation see text.

The core-level BEs for the bulk and for each interface thickness are obtained by a least-square fitting procedure applied to the Shirley background-subtracted photoemission data using Voigt lineshapes. Using this procedure the error on the BEs can be estimated as±0.025 eV. The band bending values shown in Figure 75 are grouped in three sets corresponding to distinct core-level pairs: Cd/Cu (filled squares), Cd/Zn (filled circles) and Cd/Sn (filled triangles). Considering equation (9), the error on the band bending values is conservatively evaluated to be ±0.10 eV.

The band bending averages for each set resulted to be (0.17±0.10) eV, (0.13±0.10) eV and (0.13±0.10) eV for Cd/Cu, Cd/Zn and Cd/Sn, respectively. The total average of (0.14±0.10) eV (red line in Figure 75) is in good agreement with data reported in [10]. In order to improve the accepted uncertainty of 0.1 eV for the determination of the VB edge position using the linear extrapolation of the leading edges [77], the energy position of the valence band maxima (VBM) is evaluated by modelling the VB onset with the convolution product of a Gaussian function and a Heaviside step function and applying a numerical fitting procedure that, according to our results, allows us to determine the edge position within 0.02 eV.

In our samples, the VBM positions relative to E_F for CdS and CZTS resulted to be (−1.87 ± 0.02) eV and (−0.53 ± 0.02) eV, respectively. These values are in close agreement with those reported in [53, 8, 10]. Since it is quite difficult to measure conductivity data on the thin CdS deposited by CBD, its E_F position could well be consistent with XPS measurement. On the other hand, the conductivity data on CZTS samples imply, in the bulk material, a value of $E_V - E_F$ of about 0.25 eV (see section 5.4.2). The apparent disagreement can be explained supposing that, even at the surface of pure CZTS, there is a residual downward band bending of the order of 0.25 eV. This effect could be induced by surface defects. However, it is important to note that this background band bending does not influence the VBO determination.

According to equation (8), the average VBO values obtained with the indirect method, using for the pairs Cd/Cu, Cd/Zn and Cd/Sn at different interface points for each of the above core-level combinations result to be (−1.17 ± 0.14) eV, (−1.21 ± 0.14) eV, (−1.21 ± 0.14) eV, respectively. The resulting average value of (−1.20 ± 0.14) eV is our extracted VBO. The error is calculated by adding the uncertainties in the VBM and BE positions. The VBO calculated by the indirect method results to be in good agreement with (−1.20 ± 0.15)eV of [10] and with the value of 1.01 eV of [21].

The VBO determined by the indirect method is affected, in our case, by an error that is mainly due to the band bending calculation by means of the core-level positions. On the other hand, the direct method can allow the determination of VBO without an explicit knowledge of the band bending. According to [14], it consists of measuring directly the VB at the interface CdS/CZTS and determining the two band edges relative to the material components.

The VBO value is simply obtained by the difference between the band edges positions. Figure 76 shows the clean CdS VB (panel (a)), the sequence of the VBs measured at two different thicknesses at the interface CdS/CZTS corresponding to about 14% (panel (b)) and 75% (panel (c)) of detected CZTS intensity and the clean CZTS VB (panel (d)). These spectra are normalized to the same height.

Data show that the main VB peak at about −3.5 eV, moves towards the Fermi level by about 0.15 eV on going from the clean CdS surface to the 75% CZTS. The VB shape evolution from pure CdS to pure CZTS does not show significant changes in the overall shape except for the growth of spectral intensity at about 1 eV from VBM. The shoulder at 1 eV, visible in the 14% CZTS VB (Figure 76(b)), is clearly bigger in the 75% CZTS VB (Figure 76(c)) and it is still observed nearly unchanged in the bulk CZTS VB data (Figure 76(d)).

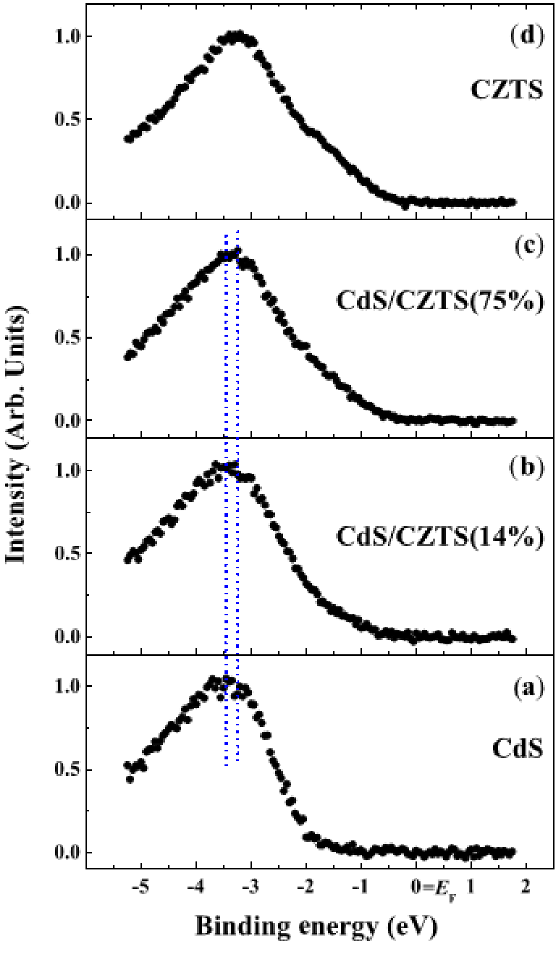

Figure 76: VB measured by XPS at different interface thicknesses. (a) VB of the clean CdS surface; (b) VB of the CdS/CZTS interface at 14% of measured CZTS total intensity; (c) VB of the CdS/CZTS interface at 75% of measured CZTS total intensity; (d)VB of the CZTS substrate only. The two vertical blue lines are guides for the eye indicating a peak shift of about 0.15 eV.

The experimentally observed VB spectral intensity at about 1 eV from VBM, growing with increasing amount of detected CZTS can be explained with the onset of CZTS Cu 3d states which dominate the DOS up to 2 eV from VBM [112, 114]. Due to the nature of the CdS/CZTS system, the VB shape at the interface (Figure 76(b) and (c)) does not show well distinct VB contributions from CdS and CZTS, making impossible a direct determination of the VBO as discussed in [14]. Indeed, the CdS VB in the region close to the VB edge consists of features originating from the outermost cation and anion s- and p-electrons [175], mainly Cd 5s and S 3p, with maximum intensity at about 3 eV from VB maximum [81] and, as discussed above, the CZTS VB has a high DOS within 2 eV from VBM due to Cu 3d states. Although our VB data do not allow a direct VBO determination, it is still possible to obtain the VBO by another approach. According to Klein et al. [76], the VBO can be evaluated by shifting the starting surface VB by the band bending related to a defined interface thickness and successively by subtracting the shifted surface VB from the VB measured on the interface at the same interface thickness.

Figure 77 shows the clean CdS VB shifted by 0.10 eV and superimposed onto the VB measured at the interface at 14% CZTS. Both spectra are normalized to the same height.

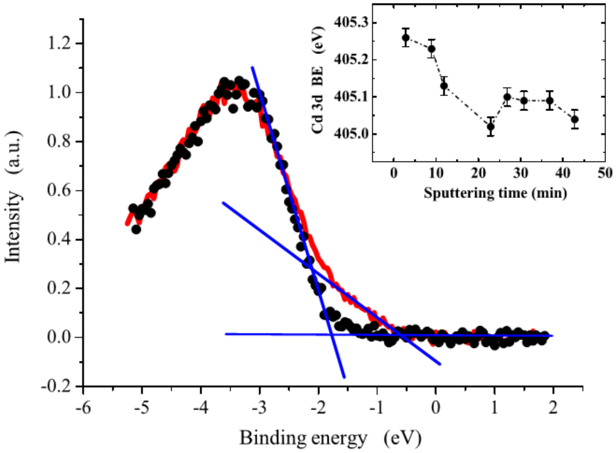

Figure 77: VBO measurement by direct VB analysis. VB measured on the 14% CZTS interface (full red line) with superimposed the clean CdS VB (black dots) shifted by a band bending of 0.10 eV. Data are normalized to the same height. The straight blue lines are only guides for the eye and indicate the approximate VBM positions and the background according to the linear extrapolation method. The inset shows the Cd 3d5/2binding energy as a function of sputtering time. A sputtering time of 12 min corresponds to 14% CZTS.

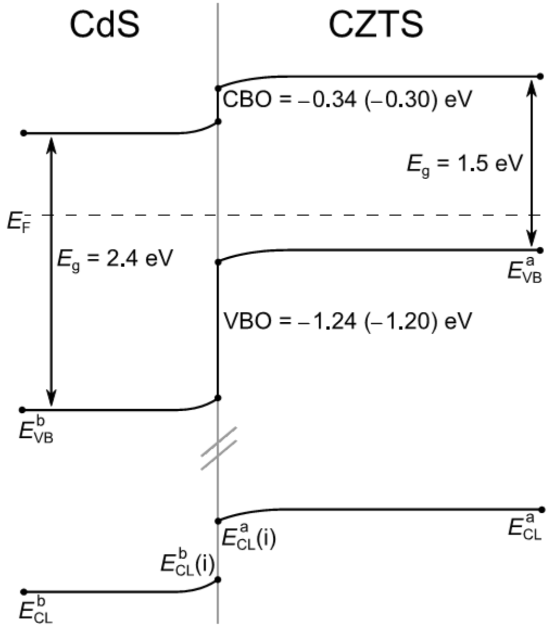

Figure 78: Band diagram of the CdS/CZTS interface resulting from this work. The values of the CBO and VBO reported in parentheses are obtained by the indirect method.

The shift on going from CdS to the CdS/14% CZTS interface is measured by means of a least-squares method to be (0.10 ± 0.02) eV. From the good matching of the two superimposed curves up to the CZTS-induced features shown in Figure 77, it is reasonable assuming that the observed shift is rigid and hence due to the band bending. This finding is also supported by a similar shift observed on the measured Cd $3d_{5/2}$ BE on going from the clean CdS to the CdS/14% CZTS interface. The Cd 3d5/2 shift is shown in the inset of figure3 and was calculated to be (0.13 ± 0.05) eV, the bigger error being due to the uncertainty in

peak position. Therefore, using the VB-determined shift, the VBO results to be (−1.24 ± 0.06) eV. This VBO value is again in good agreement with experimental data by Bar et al [10], who report a VBO of (−1.20 ± 0.15) eV, and with theoretical calculations [21] that predicted for the CdS/CZTS interface a VBO value of 1.01 eV.

The CBO can be calculated from the VBO value and the difference of the energy gaps of the two materials: $CBO = \left(E_g^b - E_g^a\right) + VBO$. Using 1.5 and 2.4 eV for the CZTS (a) and CdS (b) band gaps, respectively, the CBO calculated with the indirect method results to be (−0.30 ± 0.14) eV, while the CBO resulting from VB analysis is (−0.34 ± 0.06) eV, pointing to a cliff-like behaviour in good agreement with [10]. A schematic band diagram of the CdS/CZTS interface with the values measured in this work is shown in Figure 78 and could be one of the reasons for the Voc limitation usually reported for the actual CZTS solar cell technology. In order to improve the device performances, further efforts have to be addressed to engineer new buffer layers with optimized band alignment with CZTS absorber, thus reducing interfacial recombination phenomena.

Part III: Characterization of final devices

5.6 Efficiency evolution of solar cells based on CZTS grown from stacked precursors

The optimization of CZTS solar cells based on CZTS absorber layers grown form staked evaporated precursors was found to be quite difficult.

One of the main problems was identified with the lack of a fine stoichiometry control of the absorber layer. The stacked structure of precursors doesn't allow for compositional analysis of the starting material before sulphurization, so that the stoichiometry can be only checked *a posterior* by EDX measurements on the final materials. The results showed a good correlation with the nominal composition of precursors. However, because of a not-perfect reproducibility of the precursor evaporation process, possible losses of spurious phases during the heat treatment and experimental error of the microanalysis, some scattering is present in EDX data.

These fluctuations were found to be critical for the absorber layer optimization, especially taking into account the small phase stability region of CZTS and the effect of secondary phases on device performances.

Despite these difficulties, some trends of solar cell efficiencies with variation of precursor structure and composition have been identified and improvements of device performances have been obtained.

CZTS absorber layer were grown using ZnS-Sn-Cu stacked precursors with different structures (see Table 23), which we named as bilayer-type (B-type), threelayer-type (T-type) and monolayer-type (M-type), depending on the number of the ZnS layers present into the stack (two, three and one respectively, see Figure 79).

Table 23: Distribution of ZnS, Sn and Cu layers in stacked precursors with different structures, named as B-, T- and M-type.

Precursor Type	structure
B-type	Substrate/ZnS/Sn/Cu/ZnS/Sn/Cu
T-type	Substrate/ZnS(100nm)/Sn/Cu/ZnS/Sn/Cu/ZnS
M-type	Substrate/ZnS/Sn/Cu

The thickness of the different layers was properly set to obtain the desired [Cu]:[Zn]:[Sn] metal proportions and was varied to change precursors' composition within the Cu-poor and Zn-rich stoichiometry region (which is known to give CZTS absorber layers with the best performances [71]). CZTS with different stoichiometry were therefore obtained upon sulphurization treatment.

Their properties as isolated film were studied and discussed in Chapter III. In this section we show the results related to their application as absorber layer in solar cells.

Precursors with different zinc content were prepared by using both B and T-type structure, by varying the [Cu]:[Zn] ratio from 2:1 to 2:1:48, while keeping fixed at 2:1.18 the [Cu]:[Sn] ratio (see Table 24). The total nominal thicknesses of ZnS, Sn and Cu of precursors with different metal ratios are reported in Table 24, where an integer number, increasing from 1 to 4, is added to the precursor-type label (B or T) to indicate the increasing Zn content.

Table 24: Total nominal thicknesses of ZnS, Sn and Cu and corresponding metal ratios in precursors with different compositions.

Precursor Type	ZnS (nm)	Sn(nm)	Cu(nm)	[Cu]:[Zn]:[Sn]
B1 and T1	440	300	240	2 : 1.00 : 1.18
B2 and T2	500	300	240	2 : 1.12 : 1.18
B3 and T3	560	300	240	2 : 1.26 : 1.18
B4 and T4	660	330	240	2 : 1.48 : 1.18

CZTS films grown from B-type precursors showed poor performances as absorber layer, whereas better results have been obtained using the T-type structure. Investigations by Secondary Ions Mass Spectroscopy (SIMS) on the final materials have been discussed in Chapter III and revealed a great excess of Zn at the bottom of the film produced from B-type stacks, suggesting a residual un-reacted ZnS phase at the glass interface (see Figure III - 5). A better homogeneity has been obtained by using precursor with T-type structure, in which the first ZnS layer is only 100nm thick and the remaining Zn amount is deposited in a third layer at the end of the stack: ZnS(100nm)/Sn/Cu/ZnS/Sn/Cu/ZnS. Even for this structure, ZnS segregation is observed in the final CZTS films as a result of the Zn-rich composition of the starting precursors, but the Zn excess was found to be lower compared to samples grown from B-type precursors with the same nominal composition.

For both B-type and T-type structures, the best performing devices were obtained by using absorber layers grown from precursors containing a large excess of Zn ([Cu]:[Zn]=2:1.48), whereas precursor compositions closer to stoichiometric CZTS phase (B1-T1; B2-T2) gave very low efficiencies or not working devices.

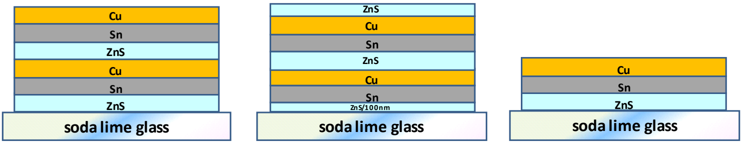

Figure 79: Distribution of ZnS, Sn and Cu layer into B- (left), T- (centre) and M-type (right) stacks.

In Figure 80 and Figure 81 the J-V characteristic curves of solar cells based on CZTS grown from B and T-type precursors with the same nominal composition are compared. The devices are listed in Table 25, where solar cells parameters, precursor type and composition are reported. Figure 80 refers to absorber layer grown from B3 and T3 precursors, whereas B4 and T4-type precursors (with higher Zn content) were used for devices of Figure 81. In both cases, device performances improve by using T-type precursors and higher efficiencies were found for higher Zn concentration. In particular, devices obtained from precursors with T4 structures showed conversion efficiencies varying from 2 to 2.75% (see Table 25), which is the best result obtained from T-type structure. This variability has to be mainly imputed to some irreproducibility of the growth process, even if some fluctuations could also depend on the quality of the *buffer* and the *window* layers and on the extent of Mo back contact sulphurization, which can be slightly different in different devices.

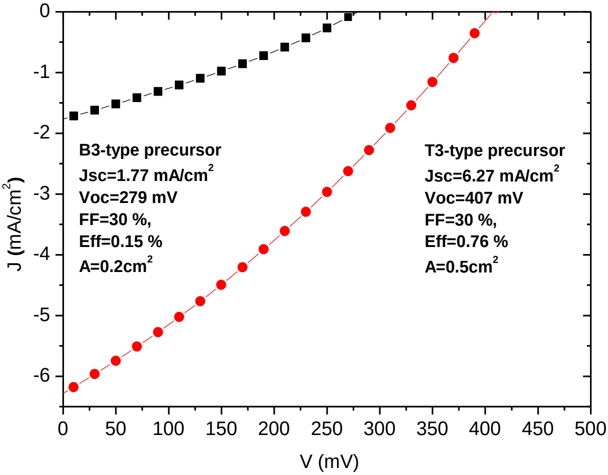

Figure 80: Comparison of J-V characteristic curves under AM1.5G illumination of two solar cells based on CZTS absorber layer grown from B3 and T3-type precursors.

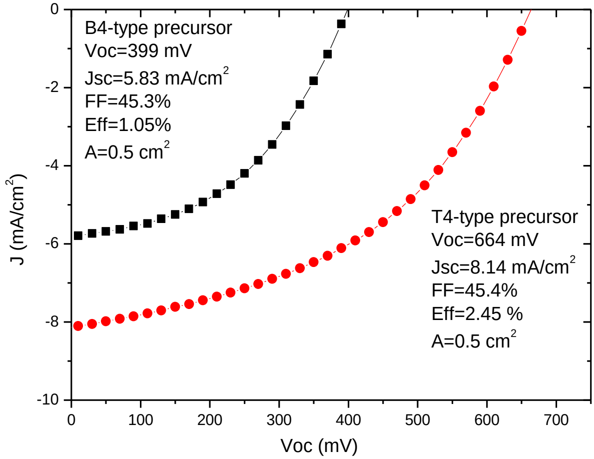

Figure 81: Comparison of J-V characteristic curves under AM1.5G illumination of two solar cells based on CZTS absorber layer grown from B4 and T4-type precursors.

Table 25: Parameters (Voc, Jsc, FF, η) of solar cells obtained from stacked precursors with B and T-type structure and with different Zn content. The nominal metal ratio in the starting precursor is reported for each device.

Cell	Prec. type	Prec. nominal composition Cu : Zn : Sn	Voc (mV)	Jsc (mA/cm^2)	FF (%)	η (%)
KC33	B3	2 : 1.26 : 1.18	279	1.77	30.0	0.15
KC32	T3	2 : 1.26 : 1.18	407	6.27	30.0	0.76
KC11a	B4	2 : 1.48 : 1.18	399	5.83	45.3	1.05
KC53	T4	2 : 1.48 : 1.18	654	6.59	48.5	2.09
KC55	T4	2 : 1.48 : 1.18	664	8.14	45.4	2.45

The not perfect reproducibility of the growth process was evidenced by optical measurements performed on isolated CZTS films, deposited on SLG: materials grown from precursors with the same structure and same nominal composition were often found to show slight differences in their optical properties. Additional investigations, discussed in Chapter IV, revealed the Sn content to be a critical parameter with a strong influence on the material band-gap energy. Possible variations of precursors' composition or losses of tin-compounds (such as SnS) during sulphurization process could therefore lead to CZTS with different quality as absorber layer. Four devices based on CZTS absorbers with different energy gap values have been selected as examples and are listed in Table 26, where solar cell parameters (Vos, Jsc, FF, η, Rs, Rsh) and absorber layer energy gap values (E04) are reported for each device. CZTS films with the highest band gap energy (1.56 and 1.60 eV) were grown using T4-type precursors, and the slight difference (0.04 eV) in their E04 have to be imputed to some variability in the growth process. Absorber layers with smaller E04 (1.50 and 1.48 eV) were instead obtained by an intentional reduction of the nominal tin content in the starting precursors (from [Cu]:[Sn]≈2:1.1 down to stoichiometric ratio 2:1.0), while keeping fixed at 1.48 the copper-zinc nominal ratio.

Table 26: CZTS solar cells obtained from T-type precursors with fixed copper-zinc nominal ratio [Cu]:[Zn] (2:1.48) and increasing tin content ([Cu]:[Sn] from 2:1 to 2:1.18).

	Voc (mV)	Jsc (mA/cm^2)	FF (%)	Rs (Ωcm^2)	Rsh (Ωcm^2)	η (%)	E04 (eV)
KC56	326	3.56	45.6	4.5	1000	0.53	1.45
KC68	462	5.91	41	3.0	3310	1.12	1.50
KC53	654	6.59	48.5	28	8000	2.09	1.56
KC55	664	8.14	45.4	35	7968	2.45	1.60

Trends of solar cell parameters with the absorber layer band-gap energy can be easily identified in Figure 82. A clear improvement of Voc, Jsc and solar cell efficiency η is observed with the increases of the E04. The low Voc resulting from low energy gap absorber layers is also due to the detrimental decrease of the shunt resistance as the E04 decreases. The increase of Jsc for increasing energy gap has to be likely imputed to the improvement of the absorber layer quality: indeed as shown in Chapter III, CZTS films with higher Sn content (resulting in higher Eg values) show lower defect density compared with materials with reduced [Sn] and lower Eg. This is also confirmed by the EQE curves measured on the devices reported in Table 26 and shown in Figure 83. The shape of these curves in the infrared region reveals a clear improvement of the charge collection in CZTS films with higher bandgap energy, related to an improvement of the carrier diffusion length.

Despite the improvement of Jsc, the current value is limited by the increase of series resistance, Rs, likely due to an increase of the bulk resistivity in materials with higher tin content, resulting in lower [Cu]/([Zn]+[Sn]) ratio. Despite this disadvantage, materials with higher energy gap were found to give the best results as absorber layers.

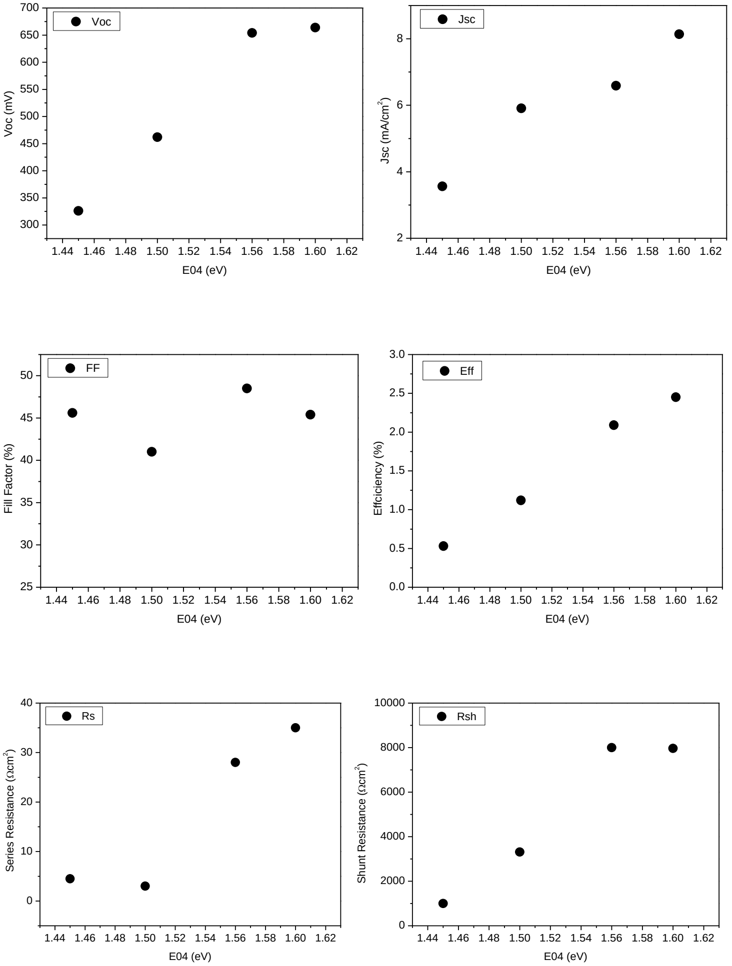

Figure 82: Trends of solar cell parameters (Voc, Jsc, FF, Eff, Rs, Rsh) with the absorber layer bandgap energy.

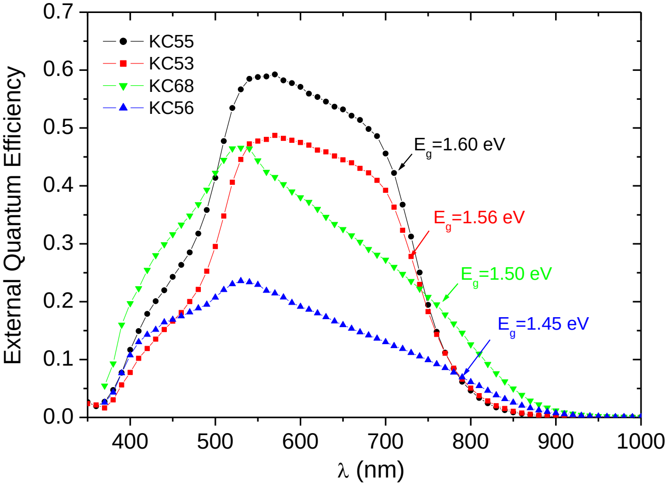

Figure 83: Comparison of EQE curves of four solar cells based on CZTS absorber layers with different bandgap energy.

The record device was obtained by a slight correction of precursor stoichiometry, by lowering the ZnS amount, with a very slight reduction of tin. The nominal thickness of the ZnS, Sn and Cu layers in the starting stack are 410, 200 and 165 nm respectively, corresponding to the nominal composition: Cu:Zn:Sn=2:1.34:1.15. This precursor was deposited according to a simple M-type structure (ZnS/Cu/Sn), in which each material is deposited as a single layer in the starting stack.

This structure was chosen taking into account that, despite the excess of zinc tends to segregate at the bottom of CZTS films (as revealed by SIMS depth profiles shown in Figure III-5), the use of precursor structures with multiple distribution of ZnS layers (as T-type stacks) can lead to the formation of additional ZnS clusters dispersed throughout the absorber layer, behaving as barriers to the grain growth. This possibility can be prevented by using a M-type structure, with a single ZnS layer in contact with the substrate.

The total nominal thickness of the new precursors is 775 nm, smaller of about a factor 1.6 then T4-type stacks (1230 nm). Precursor thickness was reduced to decrease the device series resistance and to lower the metal diffusion length requested for CZTS phase formation during sulphurization treatment.

CZTS absorber layer produced with the new precursor gave a solar cell (KC106) with efficiency 2.7%, which was raised to 3.2% (KC106*) upon evaporation of a MgF_2 antireflection coating). A SEM cross section of the record device is shown in Figure 84. Solar cell parameters (Voc, Jsc, FF, Rs, Rsh and η) are reported in Table 27.

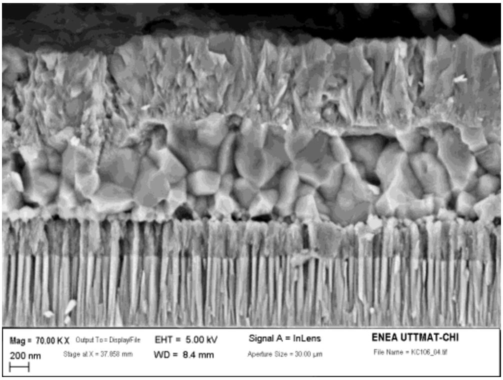

Figure 84: SEM cross section of the record device obtained from stacked precursors: the CZTS absorber layer was grown from M-type precursor with optimized composition.

Optical measurements performed on the same material deposited on SLG showed a bandgap energy of 1.62 eV, also reported in table. Parameters of the best devices obtained from B- and T-type precursors are also reported for completeness, but it has to be pointed out that, because of the difference in both precursor composition and thickness, the improvement of device performances cannot be simply imputed to the new M-type structure of precursor.

External quantum efficiency and J-V characteristic curves under AM1.5G light of the two best devices are compared in Figure 85.

The higher values of the EQE curve of the record device at wavelength higher then 700 nm are related to a larger minority carrier diffusion lenght, revealing a better quality of the absorber layer. At low wavelength (λ<500 nm), the higher EQE have to be mainly imputed to a better quality of the CdS buffer layer, which is probably thinner in case of the best device, thus showing a reduced optical absorption in the blue energy region.

Despite the lower value of the Voc of the record device, the sensible reduction of series resistance leads to higher Jsc and FF, resulting in higher efficiency. The reduction of Rs has to be imputed to both stoichiometry correction and thickness reduction of the starting precursor.

Additional investigations should be necessary to further optimize CZTS stoichiometry, in order to improve the conductivity of the absorber layer, resulting in further improvement of both Rs and FF. It has to be noted that, even removing the effect of the series resistance, the device performances result to be limited by the low value of the Jsc. This effect could be due to possible electron-hole pairs recombination phenomena at CZTS/CdS interface, which need further optimization.

Table 27: Parameters of the best solar cells obtained from CZTS absorber layer grown from precursors with B-type, T-type and M-type structure. The E04 of the same CZTS samples (deposited on SLG) is also reported, when available. Device marked with * was covered with MgF_2 antireflection coating.

Cell	Prec. type	Metal ratio Cu:Zn:Sn	Voc (mV)	Jsc $\left(\frac{mA}{cm^2}\right)$	FF (%)	Rs (Ωcm^2)	Rsh (Ωcm^2)	Eff (%)	E04 (eV)
KC11a	B4	2:1.48:1.18	399	5.83	45.3	10	1089	1.05	—
KC55	T4	2:1.48:1.18	664	8.14	45.4	35	7968	2.45	1.60
KC106	M	2:1.34:1.15	575	9.35	50	6.5	8700	2.7	1.62
KC106*	M	2:1.34:1.15	581	11.14	49.4	6.5	6250	3.2	1.62

Despite the improvement obtained in device performances, the low reproducibility of materials produced from e-beam evaporated precursors made further device optimization very difficult.

The research activity was therefore addressed to the development of a new class of CZTS thin films, grown from co-sputtered precursors. The better homogeneity of these materials, the stoichiometry control and the high reproducibility resulting from the new deposition technique led to a rapid optimization of CZTS absorber layers, giving a sensible increase of device efficiencies.

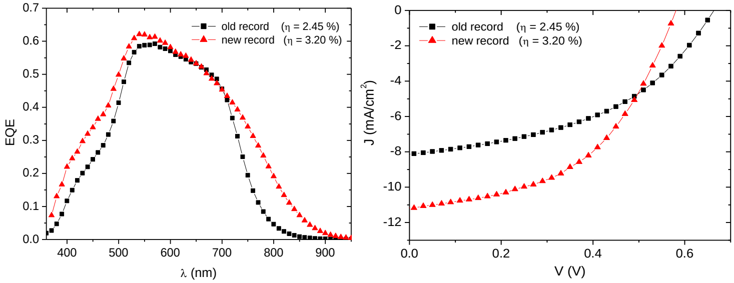

Figure 85: EQE and J-V characteristic curves of the two best devices obtained from T-type (black dots) and M-type precursors (red dots), the latter having optimized stoichiometry and thickness.

5.7 Optimization of solar cells based on CZTS grown from co-sputtered precursors

A rapid improvement of solar cell performances has been obtained by using CZTS absorber layer grown from precursors deposited by co-sputtering of ZnS, CuS and SnS targets.

As shown in Chapter IV, these materials show good homogeneity in chemical composition, which can be controlled by properly setting the power applied to each target. The sputtering conditions were firstly chosen by following the calibration procedure described in Chapter IV, and then empirically optimized looking at the performances of the final devices.

In Table 28 sputtering conditions and thickness of some selected precursors are reported. CZTS films obtained upon sulphurization of these materials were assembled into the solar cell stack in order to check their performances as absorber layer. Solar cells parameters obtained from J-V characteristic curves under AM1.5G illumination are reported the same table.

Table 28: Deposition conditions and thickness of different precursors and parameters of solar cells based on the corresponding CZTS films, obtained upon sulphurization.

prec	P_{CuS} (W)	P_{ZnS} (W)	P_{SnS} (W)	t_{dep} (min)	d (µm)	Cell	Voc (mV)	Jsc (mA)	FF %	Eff %
SP20	107	200	66	41	1.35	**KC163**	531	6.84	28	1.0
SP04	109	200	70	41	1.37	**KC173**	260	10.3	30	0.8
SP16	122	200	59	41	1.35	**KC169**	2	/	/	0
SP19	116	200	63	41	1.38	**KC172**	658	13.2	49	**4.3**
SP33	116	200	63	30	1.08	**KC187**	589	11.9	46	3.2
SP29	116	200	63	21	0.75	**KC182**	578	13	42	3.2
SP36	107	200	66	20	0.70	**KC192**	629	15.2	59	**5.7**

Looking at the last column, it is possible to see the efficiency evolution resulting from the optimization the precursor deposition conditions, changing the sputtering powers and deposition time.

EDX measurements were performed on precursors and on some selected CZTS samples. The results are reported in Table 29, where the efficiency of devices corresponding to the different materials can be also found.

Table 29: Chemical composition of precursors and CZTS samples obtained from EDX measurements. The total metal amount is normalized to 4 ([Cu]+[Zn]+[Sn]=[S]=4) and material composition is expressed using the metal ratios Cu:Zn:Sn. The efficiencies of corresponding solar cells are also reported.

prec.	EDX–prec. Cu:Zn:Sn	Cu/Sn	CZTS	EDX – CZTS Cu:Zn:Sn	Cu/Sn	Zn/Sn	Cell	Eff (%)
SP20	1.62:1.39:0.99	1.63	**K384**	1.71:1.47:0.82	2.09	1.80	**KC163**	1.0
SP04	1.75:1.26:0.98	1.78	**K392**	#	#	#	**KC173**	0.8
SP16	1.80:1.41:0.79	2.27	**K388**	#	#	#	**KC169**	0
SP19	1.73:1.41:0.86	2.01	**K394**	1.74:1.39:0.88	1.98	1.58	**KC172**	**4.3**
SP33	1.66:1.45:0.89	1.86	**K412**	#	#	#	**KC187**	3.2
SP29	1.67:1.46:0.87	1.92	**K404**	#	#	#	**KC182**	3.2
SP36	1.61:1.57:0.82	1.96	**K422**	1.65:1.51:0.84	1.97	1.79	**KC192**	**5.7**

Optimization of precursor stoichiometry

The first four samples have been deposited with a 41 min fixed deposition time, by varying the powers applied to the three targets in order to optimize precursor stoichiometry. The best device (KC172) was obtained with precursors SP19, deposited with powers: P(CuS)=116W, P(ZnS)=200 and P(SnS)=63W.

Despite the large amount of zinc revealed by EDX measurements (see Table 29), CZTS films obtained from this precursor gave a device with a 4.3% efficiency.

The J-V characteristic curves under AM1.5G illumination and dark conditions are reported in Figure 86, where those of the record device obtained from staked precursors (KC106) are also shown for comparison. All the measurements refer to devices covered with a 110 nm thick MgF_2 antireflection coating. Solar cells parameters obtained from J-V measurements under dark and light conditions are reported in Table 30.

Higher Voc and Jsc (658 mV and 13.2 mA/cm^2, respectively) are shown by solar cell KC172 (produced from co-sputtered precursor), while FF value is the same in both devices (49.4%) and it is limited by the high series resistance (about 6 Ωcm^2 in both device). The low value of the reverse saturation current density of KC172 (J_0 = 0.37 µA/cm^2) reveals a good quality of the absorber layer produced from co-sputtered material and also suggests a low carriers recombination phenomena at CZTS/CdS interface.

The great improvement of the absorber layer quality is clearly evidenced by the EQE curve reported in Figure 87, where it is compared with the best device (KC106) obtained from sacked precursors. As the spectra reaches its maximum (at λ~570nm), the curve remains almost constant until the wavelength approaches the material band gap energy (λ~775÷820 nm) and a sharp decrease is observed for higher wavelength. This shape suggests a longer minority carrier diffusion length with respect to that of materials obtained from staked precursors. The short circuit current density obtained from EQE spectra (Jsc^{EQE}) is reported in Table 30. Its higher value compared to the Jsc resulting from J-V measurements is due to the negligible contribution of Rs during the quantum efficiency measurements (being the current very low compared to that flowing under AM1.5G illumination) and to the absence of the “shadowing” effect of the metal contact grid, used for J-V measurements.

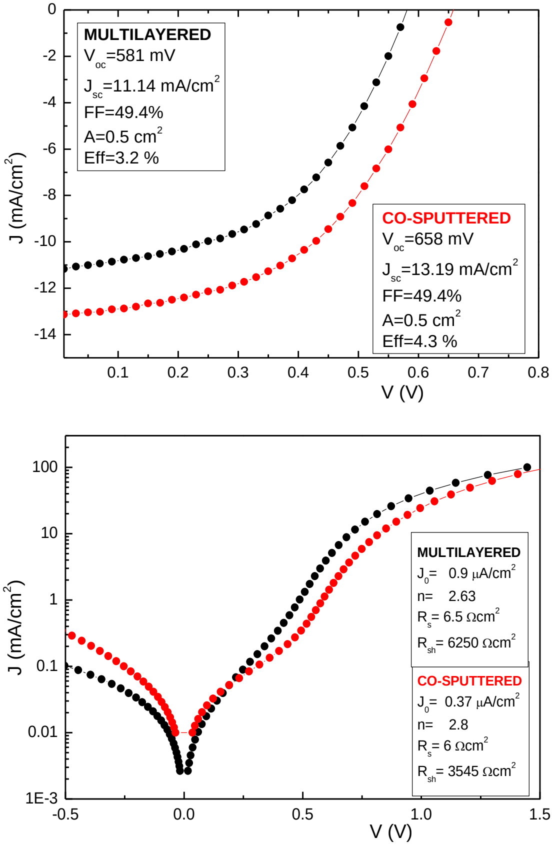

Figure 86: J-V characteristic curves under AM1.5G illumination and dark conditions of CZTS solar cells KC172 obtained from co-sputtered precursor SP19 (see Table 30). The curves of the record device KC106 obtained from stacked precursors are also shown for comparison.

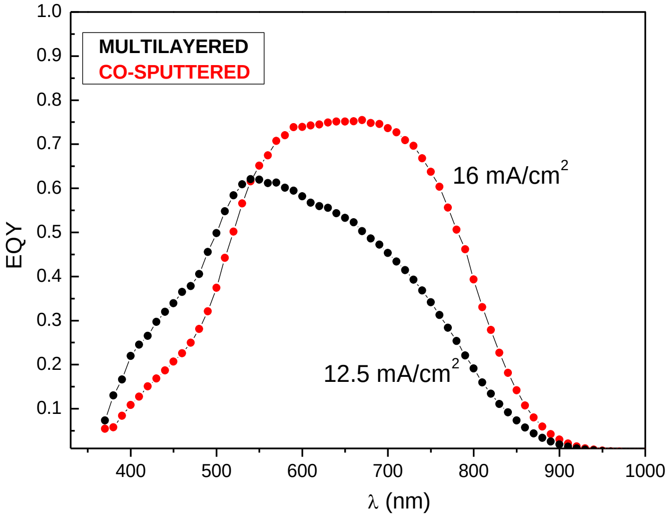

Figure 87: EQE of device KC172 obtained from co-sputtered precursor SP19 (see Table 30). EQE curve of the record device KC106 obtained from stacked precursors is also shown for comparison.

Table 30: Parameters of the best solar cells obtained from staked (M-type – KC106) and co-sputtered precursors (SP19 – KC172, SP36-KC192) and thickness of the corresponding CZTS absorber layers. Voc, Jsc, FF, Eff, Rs, Rsh obtained from J-V measurements are reported. The Jsc^{EQE} obtained from EQE spectra is also shown.

prec	CZTS thick. (μm)	Cell	Voc (mV)	Jsc $\left(\frac{mA}{cm^2}\right)$	FF (%)	J_0 $\left(\frac{\mu A}{cm^2}\right)$	Rs (Ωcm^2)	Rsh (Ωcm^2)	Jsc^{EQE} $\left(\frac{mA}{cm^2}\right)$	Eff (%)
M-type	1.0	**KC106**	581	11.14	49.4	0.90	6.5	6250	12.5	**3.2**
SP19	1.5	**KC172**	658	13.2	49.4	0.37	6.0	3545	16.0	**4.3**
SP36	0.75	**KC192**	629	15.2	59.0	0.12	1.5	19000	15.7	**5.7**

Optimization of precursor thickness

Despite the improvement resulting from optimization of precursor stoichiometry, performances of the optimized device KC172 were found to be limited by the low FF value, due to the high series resistance (6 Ωcm^2), resulting from a not optimized precursor thickness. The best results reported in literature have been obtained using CZTS absorber layer with thickness lower than 1 micron [160]. Precursors resulting from our 41 min long deposition processes are about 1.4um thick and the corresponding CZTS films obtained after sulphurization treatment have a thickness of about 1.5 µm.

Other precursors have been therefore grown by reducing the deposition time (see Table 28). This reduction required further optimization of the sputtering powers. Indeed, precursors deposited with the same sputtering powers of the optimized material (SP19), but with shorter deposition time (SP33, SP29), show different chemical compositions (with lower Cu and higher Zn content) respect the optimized precursor, thus suggesting a not constant growth rate of the sputtered species.

The record device (KC192) was obtained with a CZTS film grown from precursor SP36, deposited with P(CuS)=107W, P(ZnS)=200, P(SnS)=66W and deposition time t=20 min. The precursor thickness is 700 nm, corresponding to a 750 nm thick CZTS absorber layer. The device obtained from this material has shown an efficiency of 5.7%. A SEM cross section is reported in Figure 88. The J-V characteristic curves and EQE spectrum are shown in Figure 89 and Figure 90, while solar cell parameters are reported in Table 30.

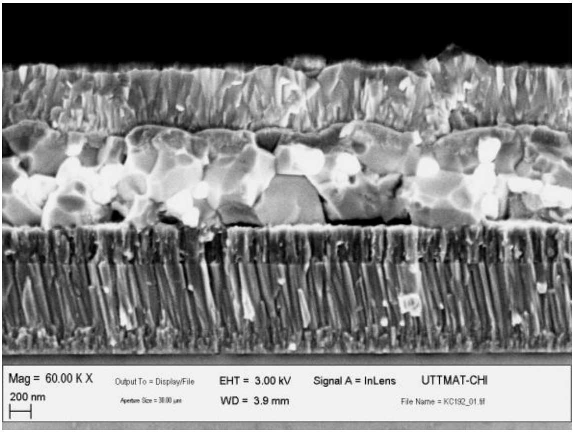

Figure 88: SEM cross section of the record device KC192.

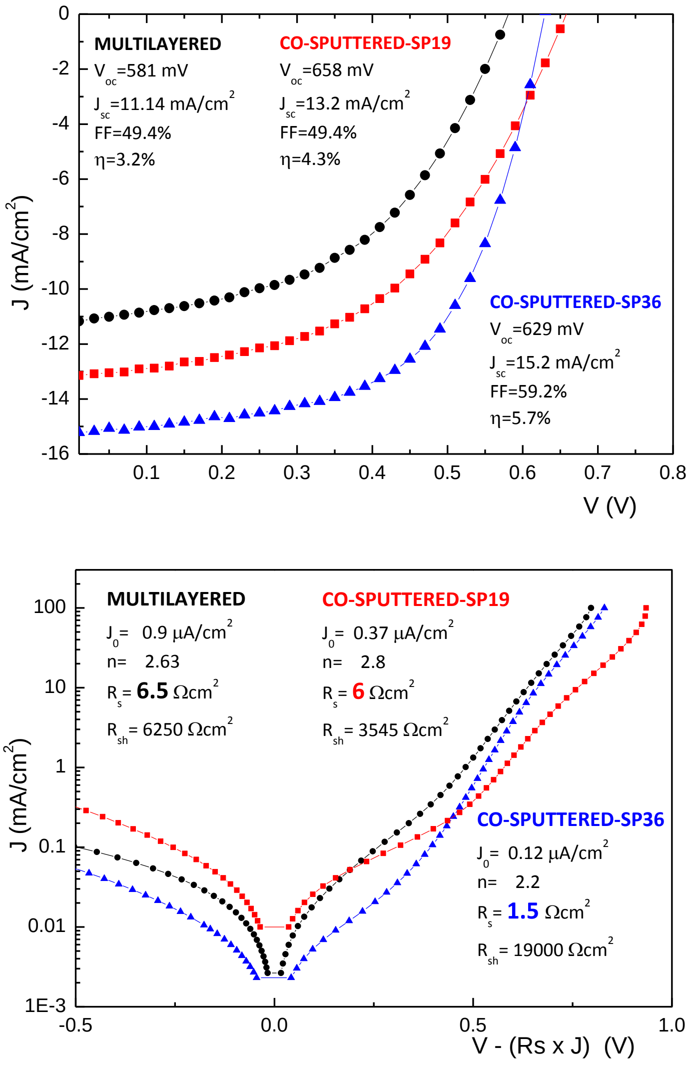

Figure 89: J-V characteristic curves under AM1.5G illumination and dark conditions of solar cells KC192 (record device) and KC172, obtained from optimized co-sputtered precursors (see Table 30). The curves of the record device KC106 obtained from stacked precursors are also shown for comparison. The dark JV curves are corrected for the Rs value of each device.

The thickness reduction led to a great improvement of Rs, which passed from 6 (KC172) to 1.5 Ωcm^2 (KC192), rising the FF from about 49% to 59%.

However, despite the higher efficiency (η=5.7%), the record device shows a lower Voc then the device KC172 (with η=4.3%) and even the quantum efficiency in the infrared region reveals a better charge collection in the latter device respect to the record solar cell. These results suggest that, despite the lower efficiency of KC172 (mainly limited by the low FF value), the corresponding CZTS film shows better properties as absorber layer than the material used in the record device KC192.

Looking at the EDX results reported in Table 29, it appears that the absorber layer stoichiometry requires further optimization: a large excess of zinc is indeed detected in the absorber layer of the record cell, with a Zn/Sn ratio as high as 1.79, while the zinc excess is reduced in case of KC172 ([Zn]/[Sn] =1.58).

Even though the EDX measurements are not available for all CZTS samples, it is interesting to note that the best working devices are based on CZTS absorber layers with a [Cu]/[Sn] ratio close and slightly smaller than the stoichiometric value ([Cu]/[Sn]=2). This result suggests a critical role of the [Cu]/[Sn] ratio on the CZTS based solar cells. Experiments to clarify the effect of CZTS stoichiometry variation on the device performances have been recently undertaken. Some preliminary results are presented in the section 5.7.1.

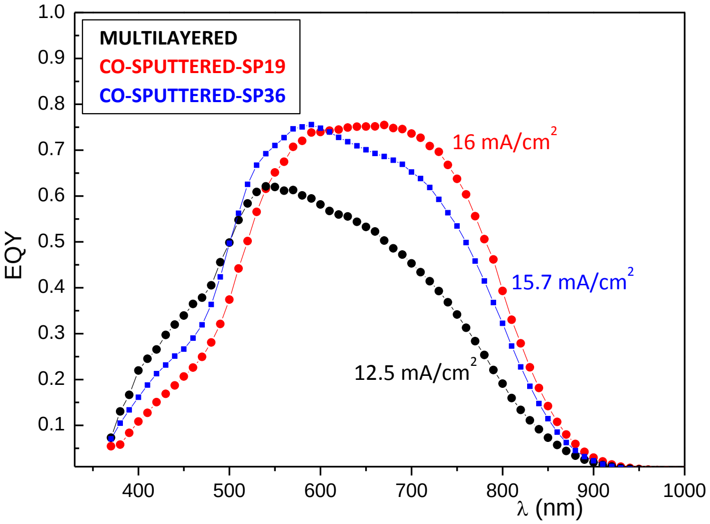

Figure 90: EQE of solar cells KC192 (record device) and KC172, obtained from optimized co-sputtered precursors (see Table 30). The curves of the record device KC106 obtained from stacked precursors are also shown for comparison.

Reduction of the zinc content: blistering effect

As previously shown, our record devices suffer from a very large excess of zinc in the absorber layer. Other solar cells were therefore fabricated using CZTS films grown from precursor with lower zinc content, deposited with sputtering conditions similar to those of the record material (SP36), but decreasing the sputtering power applied to ZnS target from 200 to 180 and 160W. The deposition time was slightly increased (from 20 to to 21 and 22 min, respectively), to obtain the same sample thickness (about 700nm).

As discussed in Chapter IV, CZTS films grown from these materials have shown a great improvement in morphology, showing several grains spanning all the sample thickness, but sever adhesion problems have been found, due to the blistering effect discussed in section 4.5.

An example is shown in Figure 91, where a cross section of the device KC204 (obtained from the precursor deposited with P(ZnS)=160W, see Table 31) is reported, together with a planar view of the corresponding CZTS absorber layer.

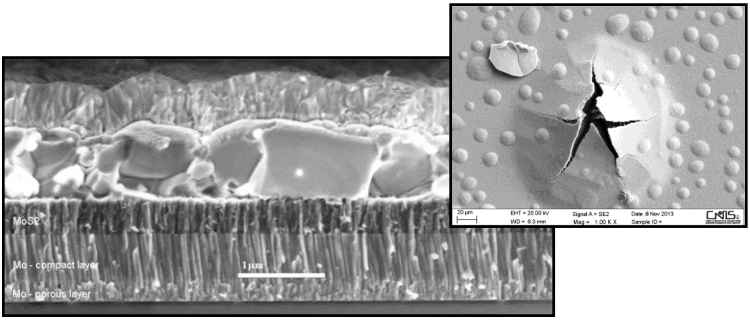

Figure 91: SEM cross sections of the device KC204 obtained from precursor SP43, with a reduced tin content respect to the record device (KC192). In the inset, the planar view of the corresponding CZTS absorber layer, showing blistering effect.

Solar cell parameters of the same device are reported in Table 31, where they are compared with those of the record solar cell (KC192). The increase of the grain dimensions leads to a large improvement in the short circuit current and the EQE spectral response revealed a better charge collection in the infrared energy region, thus suggesting a longer diffusion length of the minority carriers (see Figure 92). However, the device performances are limited by the low value of the shunt resistance (500 Ωcm^2), reducing both Voc and FF. This result is a consequence of the blistering phenomenon: indeed, the breakage of the blisters gives rise to circular holes (with diameter of about 20÷30 µm) with an ensuing device shunting.

Table 31: ZnS power supply used for the deposition of the record material (SP36) and the precursor SP43 with reduced zinc content. The other deposition conditions are the same for both precursors. The Zn/Sn ratio measured by EDX in the as-deposited materials and parameters of the corresponding solar cells obtained from the two precursors are also reported.

prec	P_{ZnS} (W)	$\frac{Zn}{Sn}$	Cell	Vo (mV)	Jsc $\left(\frac{mA}{cm^2}\right)$	FF (%)	J_0 $\left(\frac{\mu A}{cm^2}\right)$	Rs (Ωcm^2)	Rsh (Ωcm^2)	Eff (%)
SP36	200	1.98	**KC192**	629	15.2	59	0.12	1.5	19000	**5.7**
SP43	160	1.23	**KC204**	583	17.9	51	6.8	1.8	500	**5.3**

The solar cell parameters reported in Table 31 (KC204) refer to a very small device (with an active area 0.1 cm^2), with no Al grid and no antireflection coating, obtained by mechanical scribing of a selected zone without a clear blistering effect. However, microscopic holes can be present and are most likely responsible for the very low shunt resistance value. The origin of the blistering phenomenon is still under investigation. Production of solar cells using proper back-contact buffer layer (deposited between CZTS and Mo) is currently ongoing. Preliminary experiments showed that blistering effect can be suppressed by using ZnS and i:ZnO buffers. This last material gave also promising results in terms of device efficiency: a device with 5.6% has been recently produced and further improvements are expected from additional optimization of the absorber layer stoichiometry.

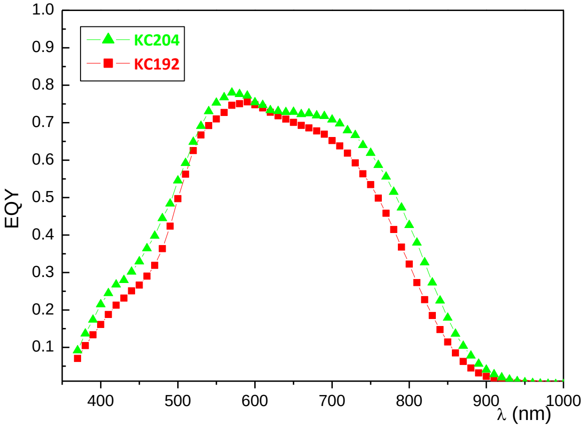

Figure 92: EQE curves of the record device KC192 and of the solar cell KC204, produced by lowering the Zn/Sn ratio in the CZTS absorber layer.

5.7.1 Combinatorial study of co-sputtered Cu_2ZnSnS_4 thin film stoichiometry for photovoltaic devices

It is generally accepted that CZTS thin films with a Zn-rich and Cu-poor composition give the better results in terms of photovoltaic performances [71], but a more detailed definition of the optimal stoichiometry still lacks. The results presented in the previous section and reported in [154] suggest that even Cu/Sn ratio could play an important role.

To investigate the effect of CZTS thin film stoichiometry variation on solar cell performances, combinatorially graded thin-film Cu-Zn-Sn-S library samples were grown spanning a wide region of the ternary Cu_2S-ZnS-SnS_2 phase diagram.

Usually, our precursors are grown by simultaneously sputtering CuS, SnS, and ZnS on a 7.5x7.5 cm^2 rotating substrate. By stopping the substrate rotation, films with a graded composition due to a metal enrichment in the substrate region near the respective sulphide target have been obtained.

Such precursors were then annealed at 550°C in a tube furnace with a stoichiometric excess of sulphur, using the standard process adopted in this work for the sulphurization of stacked and co-sputtered precursors.

The films were then processed to obtain a matrix of small area complete photovoltaic devices to investigate the correlation between the stoichiometry and the device performances. Several devices were also characterized by photoluminescence (PL) measurements aimed to support a recently suggested correlation between PL peak energies and photovoltaic performances [46]. These studies are still ongoing and in the following the first preliminary results are presented.

Seven combinatorial samples with somewhat different growth parameters were prepared, but they all show very similar properties. Therefore, the discussion presented in the following refers to the results obtained on one of them, grown with deposition conditions: $P_{Ar}=3\cdot10^{-3}$ mbar, P_{DC}(CuS) =107 W, P_{RF}(ZnS) =160 W, P_{RF}(SnS) =66 W, and t_{dep}=20 minutes. These parameters are similar to those used for our best device (5.7% efficiency, Table 28) with the exception of a lower P_{RF}(ZnS) (160 W instead of 200 W) to reduce the excess of zinc content detected in the record device absorber layer (see section 5.7).

The composition of the precursor film was mapped by SEM-EDX measurements on 36 different points. In Figure 93 and Figure 94 the maps of [Cu]/[Sn] and [Zn]/[Cu+Sn] ratios are reported. Although the composition variations are quite large, a Zn-rich composition ([Zn]/[Cu+Sn]>0.33) is observed all over the sample surface.

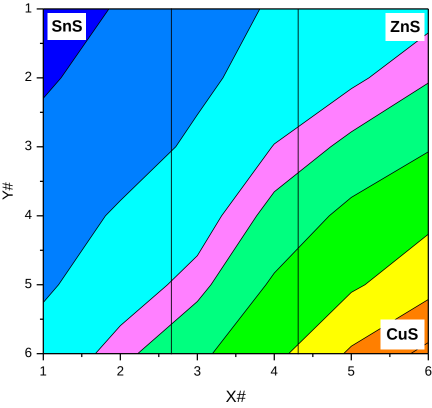

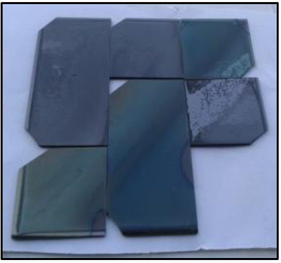

Figure 93: Cu/Sn ratios as measured by EDX. The lables of the binary sulphides at the three corners of the figure show the position of the corresponding target respect to the substrate.

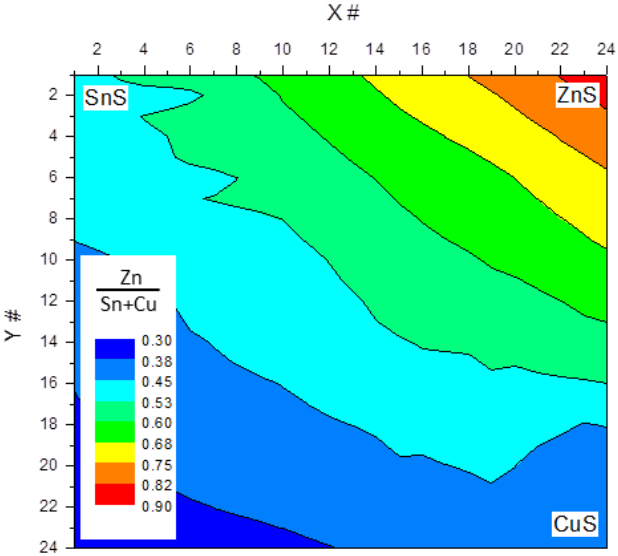

Figure 94: : Zn/(Sn+Cu) ratios as measured by EDX.

After the precursor deposition, the sample was cut into 9 squares (2.5x2.5 cm^2), placed into the small, non-sealed glass-reaction chamber used for the sulphurization treatment, together with a large stoichiometric excess of sulphur, and then putted in the tube oven where the sulphurization takes place. A picture of the samples obtained after the sulphurization treatment is reported in the inset of Figure 93 and clearly shows different diagonal regions with different morphologies, correlated to the composition of the starting material. The optimum composition lies in a diagonal stripe corresponding to a variable Zn content (but always Zn-rich) and a Cu/Sn ratio comprised in a narrow range of values from 1.9 to 2.1 (see Figure 93). This stripe, darker and more polished, is clearly visible in the more detailed picture in Figure 95.

On both sides of this stripe, the CZTS film often shows blisters, with a diameter of 20-30 micron and a few micron high, which result from a combined effect of film compressive stress and of reduced adhesion of the CZTS on the MoS_2 layer. The breakage of these blisters gives rise to circular holes, which degrade the devices lowering their shunt resistance. Regions with more severe adhesion problems or with clear signs of secondary phase formation appear farther away from this stripe, in the Cu-rich and in the Sn-rich regions, respectively.

Figure 95: Picture of two portions of a sulphurized sample containing the [Cu]/[Sn] ≈ 2 stripe

The CZTS thin films have been employed to fabricate solar cells: after sulphurization treatment the device is completed by growing a CdS layer by chemical bath deposition and depositing an intrinsic ZnO layer (100 nm) and an AZO layer (450 nm) by sputtering, using the same experimental procedures described in section 5.2. However, in the case of homogeneous samples, an Al grid was evaporated on the *n*-contact to improve current extraction, the cell area was then defined by mechanical scribing and the best cells were completed with the evaporation of an anti-reflection coating (110 nm of MgF_2). The samples obtained from films with graded compositions were instead scribed in order to get 576 (24×24) square cells (3×3 mm^2) with no Al-grid and no MgF_2 coating. This device matrix was used to map the open circuit voltage (Voc; see Figure 96), the cell short-circuit current density (Jsc; see Figure 97), and the Jsc·Voc product (see Figure 98), measured under AM1.5G illumination. Single selected cells with interesting features were more completely characterized by measuring the J-V characteristic curves, both under AM1.5G illumination and dark conditions, and the External Quantum Efficiency (EQE). Although the spot of our EQE apparatus is slightly too large to fit completely inside the 3x3 mm^2 device, the EQE shape is very useful to evaluate the material properties.

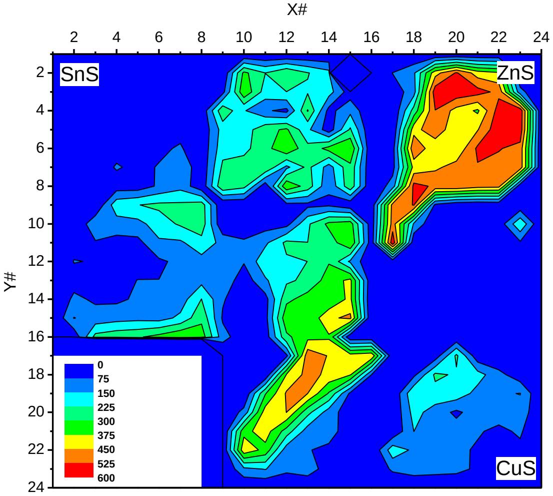

Figure 96: Map of the cell open circuit voltage Voc (in mV).

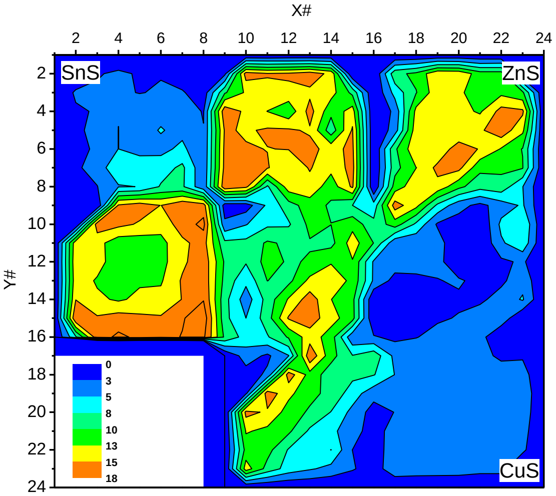

Figure 97: Map of the cell short circuit current density Jsc(in mA/cm2).

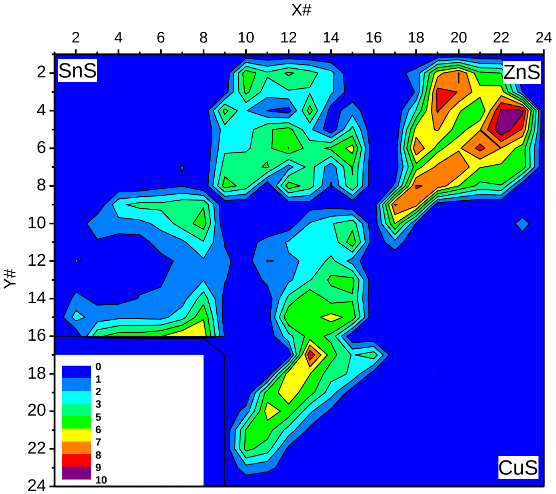

Figure 98: Map of the product Voc·Jsc (in mW/cm2).

All the seven combinatorial samples show clearly that the worst region is the Cu-rich one beyond the diagonal stripe: in that triangular area the solar cells have invariably a V_{oc} near zero. The highest values of V_{oc} are obtained in the nearly stoichiometric stripe. Figure 96 suggests that a large excess of zinc is also useful, but this trend is not always respected.

Good values of J_{sc} are achieved, instead, not only in the nearly stoichiometric stripe but also in the Sn-rich region (see Figure 97), where anyway V_{oc} values are generally low (<400 mV).

The best cell performances are therefore obtained along the nearly stoichiometric diagonal stripe, as evident from Figure 98, where the map of the $V_{oc}\cdot J_{sc}$ product, namely, a more informative parameter, is shown. This parameter, expressed in mW/cm^2, is indeed numerically coincident with the upper limit (Fill Factor=1) of percentage conversion efficiency under standard AM1.5 illumination (100 mW/cm2).

It must be noted that the V_{oc} decrease in the Sn-rich region is not unavoidable: in other samples, some cells with good V_{oc} values were obtained in this region. This suggests that factors different from stoichiometry variations could be involved.

For example, it has been reported that in cells based on Sn-rich materials the CdS deposition often produces “colloidal” films which degrade the cell performances [71].

This has been often, but not always, observed in our samples and deserves further investigation. It could be connected to the presence of spurious phases of SnS_x on the film surface.

To exclude any role of SnS_x spurious phases in the high Jsc values measured in the Sn-rich region, we have compared the External Quantum Efficiency of some cells, located well above the stoichiometric stripe, with that of our best cell based on a material with a [Cu]/[Sn]=1.98 (see Figure 99).

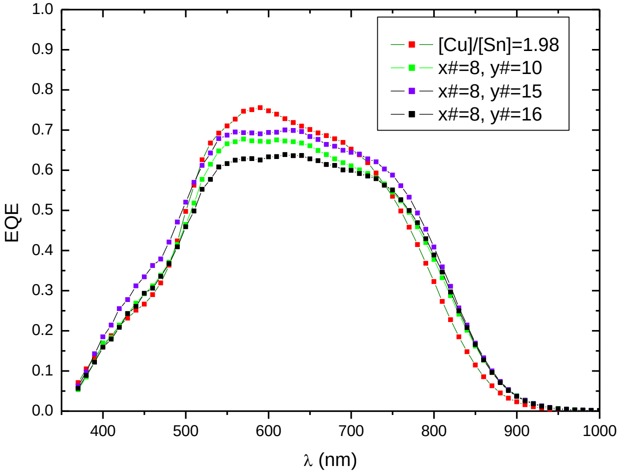

Figure 99: External Quantum Efficiency of 3 cells in the Sn-rich region compared with our best device (with [Cu]/[Sn]≈1.98).

The long wavelength tails are quite similar, thus suggesting that no spurious phases are involved. By taking into account the lack of any antireflection coating and the partial spread of the light spot outside the cell area, the material of the small cells seems to be even better that that in our best cell. The dark JV curves of these small cells show that their performances are limited both by a high J_0 and a low shunt resistance. A low quality CdS buffer layer could account for both these problems.

We have also tried to confirm a correlation between the PL peak energy and photovoltaic performances, recently suggested in [46]. In this work, the peak energy shifts from about 1.23 eV down to 1.18 eV as the cell efficiency increase from 5% to 7.5%. Since the shift is more evident for high efficiency cells, we have selected some of the best cells near the stoichiometric stripe and have measured the PL spectrum. PL was excited by a frequency-doubled Nd:YVO_4 laser with a spot diameter of ~200 micron, dispersed by a 0.75 m monochromator, and detected by a liquid N-cooled Si CCD. The results obtained at 10 K under an excitation power density of 0.4 W/cm^2 are reported in Figure 100, where no correlation is observed. All the devices show the same peak position (about 1.23 eV) with the single exception of a very bad device. The efficiency of our cells is likely still too low to show clearly this effect.

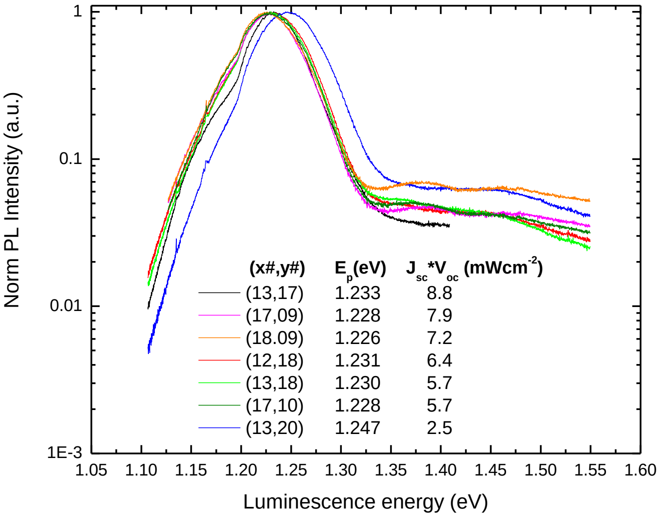

Figure 100: Photoluminescence spectra of seven cells with different Voc×Jsc product.

The results obtained from this study show that the correlation between the CZTS stoichiometry and the performances of photovoltaic devices is not only due to the quality of the grains which build up the material. Mechanical stress as well as surface composition and morphology are important, too. A deeper understanding of these factors could widen the useful composition region with respect to the one that has been considered optimal up to now. Further experiments are under way to investigate in greater detail a more limited range of compositions near the optimal values.

Chapter VI

Conclusion and future perspective

The main goal of this project was the development of CZTS thin films with suitable properties for their application in high efficiency solar cells.

Two different processes have been developed for the material growth, with the aim of achieving a good homogeneity, phase stability, control of the film composition and a good process reproducibility.

Both growth processes are based on vacuum deposition of precursors, followed by a heat treatment in sulphur atmosphere. The first approach, described in Chapter III, was based on electron-beam evaporation of stacked layer precursors made of ZnS, Sn and Cu, whereas a second explored route, described in Chapter IV, was the co-sputtering deposition of the three binary sulphides CuS, ZnS and SnS.

All the materials were characterized as isolated films and their properties as absorber layers in solar cells were also evaluated and discussed in Chapter V.

Both the processes gave good quality thin films, showing CZTS as the main crystalline phase, large grain size and suitable properties for PV applications. However, using stacked layer precursors, the achievement of a good homogeneity was found to be a critical issue. Indeed, experiments performed on solar cells showed that Zn-rich compositions of CZTS are required to obtain good efficiency devices, but such compositions resulted in quite large ZnS segregations at the CZTS/substrate interface in material grown from multilayered precursors.

The co-sputtering route was demonstrated to give more successful results in terms of stoichiometry control and chemical homogeneity: even for off-stoichiometry composition of the samples, a uniform distribution of the elements was observed in as-deposited precursors and a good homogeneity was found to be also preserved in the final materials obtained after the sulphurization treatment.

In this work, detailed studies of CZTS optical properties, microstructure, intrinsic defect density and their correlation with the material composition have been undertaken and presented in Chapter III. CZTS thin films produced from stacked layer precursors were used for these investigations and different materials were grown by varying the film composition in the Zn-rich region. A clear dependence of the CZTS optical properties on the tin content was demonstrated, whereas the zinc concentration was found to be a less important parameter. An abrupt increase of the band gap energy from 1.48 to 1.63, consistent with the spread of results reported in the literature, has been observed for increasing tin content and a large increase of the sub-gap absorption coefficient was found in samples with lower energy gap. A mechanism based on the increase of the intrinsic defect density induced by a reduced tin content was proposed as a possible explanation for the optical properties variability. This hypothesis was also proved to be consistent with the increase of non-radiative recombination phenomena in samples with lower energy gap, as revealed by the huge reduction of their photoluminescence response. The measurement uncertainty of the microanalysis make difficult to clearly identify the optimal stoichiometry region to minimize the defect concentration, but, for Zn-rich compositions, a Cu/Sn ratio lower than two seems to be desirable.

As the tin content increases, an increase of both crystalline domain size and average grain dimensions was also observed. The grain boundaries contribution to the CZTS absorption coefficient was evaluated: it was found that it could account for the increase of the sub-gap absorption spectra observed in materials with higher defect density and lower energy gap, showing smaller grain size.

Further characterization and modelling efforts are needed to clarify the nature of the intrinsic defects and to determine their location in the bulk or/and at the grain boundaries.

Additional investigations are necessary to clarify the effect of the heat treatment conditions (such as annealing temperature, duration, sulphur partial pressure) and of the nature of the precursors (stacked layered or homogeneously mixed). Optical characterizations of CZTS films produced from co-sputtered precursors with different compositions seem to confirm the trend of the bandgap energy with the Cu/Sn ratio observed in materials grown from stacked precursors.

Up to now, the investigations on the optical properties of co-sputtered precursors have been limited by the film delamination on soda lime glass substrates, revealing a high stress state of the as-deposited materials. Adhesion improvement has been recently obtained by optimizing the sputtering conditions and detailed investigation on these materials are expected to confirm the role of the tin content on the CZTS physical properties.

A second and parallel activity presented in this work was focused on the optimization and the characterization of the final devices. CZTS solar cells were produced using the standard structure, typically adopted in the literature, based on Mo back contact, CdS buffer layer and i:ZnO/AZO window layer. CZTS thin films produced from both stacked evaporated and co-sputtered precursors were used as absorber layer.

The investigation performed on CZTS thin films grown from stacked precursors with different composition allowed a first optimization of the absorber layers suggesting that higher energy gap values (of about 1.6 eV) are correlated with a lower defect density and therefore with higher material quality. This conclusion was confirmed by the characterization of the final devices: as the Eg increases, an improvement of conversion efficiency was demonstrated and a clear correlation with the improvement of the absorber layer quality was confirmed by the EQE curves. A record efficiency of 3.2% was achieved using this growth process. However, further advances with CZTS solar cells produced from e-beam evaporated precursors were found to be difficult. Despite the film stoichiometry can be controlled by varying the metal proportions into the starting precursors, the limited reproducibility of the evaporation process didn’t allow for a sufficiently fine control of the film composition, required for additional optimization of the absorber layer.

The co-sputtering route was demonstrated to be more successful in terms of process reproducibility and control of the film composition, which can be finely tuned by properly setting the sputtering powers. Using this approach, a fast improvement of solar cell efficiency was obtained and detailed investigations on the relationship between the absorber layer stoichiometry and the device performances were presented in Chapter V.

Efficiencies over 5% were obtained using absorber layers containing a large excess of zinc, with a Zn/Sn ratio well above the stoichiometric value and with a Cu/Sn ratio close and slightly lower than two (Cu/Sn ~1.97÷1.98), whereas a considerable efficiency reduction was observed for higher value of Cu/Sn.

Nevertheless, it was also proved that an improvement of the material quality can be obtained by reducing the zinc excess. The record device, with efficiency of 5.7%, was obtained using a CZTS film with a Zn/Sn ratio of 1.79 and Cu/Sn =1.97. CZTS films with a lower Zn/Sn ratio, compared to the record material, gave devices with much improved Jsc (with values of about 18 mA/cm^2) and their EQE spectral response revealed a better charge collection in the infrared energy region, thus suggesting a longer diffusion length of the minority carriers. These results are related to a great improvement of the film morphology, showing very large grains spanning all the sample thickness. This result is likely connected to a reduction of the amount of dispersed ZnS clusters, which typically form as result of the Zn-rich composition blocking the grain growth during the heat treatment. The slightly lower efficiency of these devices is due to lower values of both the FF (about 50%, compared to 59% of the record solar cell) and the Voc, correlated with an unexpected blistering phenomenon observed in these samples. Indeed, the breakage of these blisters gives rise to circular holes, which degrade the device performances lowering their shunt resistance.

Further investigations are necessary to clarify the origin of this phenomenon: it could be due to a high compressive stress state of the CZTS films, resulting from the co-sputtering deposition, but some gas evolution or a reduced adhesion of CZTS at the molybdenum interface could also be involved.

The control of the CZTS/Mo interfacial properties is indeed a critical issue and it is connected to the formation of a MoS_2 interfacial layer, as a result of the partial sulphurization of the Mo back-contact during the heat treatment of precursors. Different thicknesses, crystallographic orientation and intrinsic conductivity of MoS_2 layer can have a strong influence both on the adhesion of the CZTS absorber layer and on the electrical behaviour of the back-contact.

According to some simulations presented in this work, a highly p-type conductivity of the MoS_2 interfacial layer is necessary to assure a good ohmic contact with CZTS, whereas a n-type MoS_2 would result in a blocking barrier. The necessity for doping control of the MoS_2 layer was therefore shown, but critical problems remain regarding its possible detrimental reaction with the absorber layer and its influence on CZTS growth and adhesion properties. Further efforts have still to be done to engineer proper back-contact buffer layer able to assure both a good ohmic behaviour and a long term stability of the interface at the same time.

Part of this work was also devoted to the characterization of the CdS/CZTS front interface. A not-optimal *cliff-like* band alignment between CZTS and CdS was found in our devices, in accordance with other results reported in the literature and a clear parasitic absorption was revealed by the EQE measurements. The optimization of growth process conditions to control the physical properties of CdS, such as conductivity, morphology and interface quality could help to improve its performance as buffer layer. However, a substantial increase of the cell V_{oc} could require the shift to some alternative buffer material.

The simple transfer of the CIGS technology to the CZTS compounds has given a quick improvement of the conversion efficiency; hopefully, by employing innovative materials, device efficiency far beyond the current record values will be reachable, thus making the CZTS technology commercially appealing.

Conversion efficiency evolution of the ENEA group CZTS solar cells in the last four years, compared with the world's best efficiencies

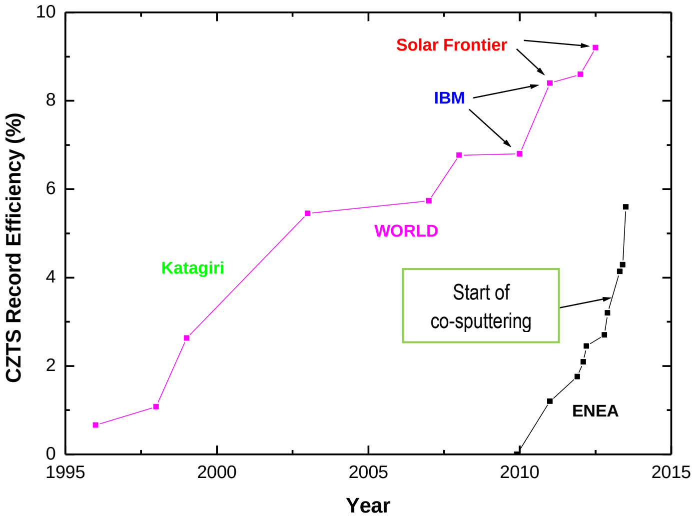

Bibliography

[1] D. Abou-Ras, G. Kostorz, D. Bremaud, M. Kälin, F. V. Kurdesau, A. N. Tiwari, and M. Döbeli, Formation and characterisation of $MoSe_2$ for $Cu(In,Ga)Se_2$ based solar cells. *Thin Solid Films*, 480–481, 433–438, 2005.

[2] International Energy Agency. Technology roadmap, Solar photovoltaic energy (IEA), 2009.

[3] S. Ahn, S. Jung, J. Gwak, A. Cho, K. Shin, K. Yoon, D. Park, H. Cheong and J. H. Yun. Determination of band gap energy (E_g) of $Cu_2ZnSnSe_4$ thin films: on the discrepancies of reported band gap values. *Applied Physics Letters*, 97(2), 021905, 2010.

[4] M. Altosaar, J. Raudoja, K. Timmo, M. Danilson, M. Grossberg, J. Krustok and E. Mellikov. $Cu_2Zn_{1-x}Cd_xSn(Se_{1-y}S_y)_4$ solid solutions as absorber materials for solar cells. *Physica Status Solidi (a)*, 205 , 167–170, 2008.

[5] M. T. Anthony. *Spectrometer calibration*, Chapter: App. 1, p. 429. Wiley, 1983. Book title: Practical surface analysis: by auger and x-ray photo-electron spectroscopy.

[6] S. Bag, O. Gunawan, T. Gokmen, Y. Zhu, T. K.. Todorov and D. B. Mitzi. Low band gap liquid-processed CZTSe solar cell with 10.1% efficiency. *Energy Environ. Sci. 5, 7060*–7065, 2012.

[7] M. Bär, S. Nishiwaki, L. Weinhardt, S. Pookpanratana, W. N. Shafarman and C. Heske. Electronic level alignment at the deeply buried absorber/Mo interface in chalcopyrite-based thin film solar cells. *Applied Physics Letters*, 93(4), 042110, 2008.

[8] M. Bär, B.-A. Schubert, B. Marsen, S. Krause, S. Pookpanratana, T. Unold, L. Weinhardt, C. Heske and H.-W. Schock. Impact of KCN etching on the chemical and electronic surface structure of Cu_2ZnSnS_4 thin-film solar cell absorbers. *Applied Physics Letters*, 99(15), 152111, 2011.

[9] M. Bär, B.-A. Schubert, B. Marsen, S. Schorr, R. G. Wilks, L. Weinhardt, S. Pookpanratana, M. Blum, S. Krause, Y. Zhang, W. Yang, T. Unold, C. Heske and H.-W. Schock. Electronic structure of Cu_2ZnSnS_4 probed by soft X-ray emission and absorption spectroscopy. *Physical Review B*, 84(3), 035308, 2011.

[10] M. Bär, B.-A. Schubert, B. Marsen, R. G. Wilks, S. Pookpanratana, M. Blum, S. Krause, T. Unold, W. Yang, L. Weinhardt, C. Heske and H.-W. Schock. Cliff-like conduction band offset and KCN-induced recombination barrier enhancement at the CdS/Cu_2ZnSnS_4 thin-film solar cell heterojunction. *Applied Physics Letters*, 99(22), 222105, 2011.

[11] N. Barreau, S. Marsillac, J. C. Bernede and L. Assmann. Evolution of the band structure of β-$In_2S_{3-3x}O_{3x}$ buffer layer with its oxygen content. *J. Appl. Phys.*, 93(9), 5456–5459, 2003.

[12] F. Biccari, R. Chierchia, M. Valentini, P. Mangiapane, E. Salza, C. Malerba, C. L. Azanza Ricardo, L. Mannarino, P. Scardi and Alberto Mittiga. Fabrication of Cu_2ZnSnS_4 solar cells by sulfurization of evaporated precursors. *Energy Procedia*, 10(0), 187–191, 2011. Presented at the EMRS 2011 Spring Meeting, Strasbourg, France.

[13] Bruker-AXS. TOPAS Version 3, Karsrluhe, Germany, 2000. http://www.bruker-axs.com/topas.html.

[14] F. Capasso and G. Margaritondo. *Heterojunction Band Discontinuities: Physics and Device Applications*. Elsevier Science Ltd, 1987.

[15] R. Castro-Rodriguez, A. I. Oliva, V. Sosa, F. Caballero-Briones and J. L. Pena. Effect of indium tin oxide substrate roughness on the morphology, structural and optical properties of CdS thin films. *Applied Surface Science*, 161, 340–346, 2000.

[16] R. W. Cheary and A.Coelho. A fundamental parameters approach to X-ray line-profile fitting. *J. Appl. Cryst.*, 25, 109–121, 1992.

[17] S. Chen, A. Walsh, X.G. Gong and S.H. Wei. Classification of lattice defects in the kesterite Cu_2ZnSnS_4 and $Cu_2ZnSnSe_4$ earth-abundant solar cell absorber. *Adv. Mater.*, 25, 1522–1539, 2013.

[18] S. Chen, L. Wang, A. Walsh, X.G. Gong and S.H. Wei. Abundance of Cu_{Zn} + Sn_{Zn} and $2Cu_{Zn}$ + Sn_{Zn} defect clusters in kesterite solar cells. *Appl. Phys. Lett.*, 101(22), 223901, 2012.

[19] S. Chen, X. G. Gong, A. Walsh and S.H. Wei. Crystal and electronic band structure of Cu_2ZnSnX_4 (X=S and Se) photovoltaic absorbers: First-principles insights. *Applied Physics Letters*, 94(4), 041903, 2009.

[20] S. Chen, X. G. Gong, A. Walsh and S.H. Wei. Defect physics of the kesterite thin-film solar cell absorber Cu_2ZnSnS_4. *Applied Physics Letters*, 96(2), 021902, 2010.

[21] S. Chen, A. Walsh, J.H. Yang, X. G. Gong, L. Sun, P.X. Yang, J.H. Chu and S.H. Wei. Compositional dependence of structural and electronic properties of $Cu_2ZnSn(S,Se)_4$ alloys for thin film solar cells. *Physical Review B*, 83(12), 125201, 2011.

[22] S. Chen, J.H. Yang, X. G. Gong, A. Walsh and S.H. Wei. Intrinsic point defects and complexes in the quaternary kesterite semiconductor Cu_2ZnSnS_4. *Physical Review B*, 81(24), 245204, 2010.

[23] K. L. Chopra, P.D. Paulson and V. Dutta. Thin-film solar cell: an overview. *Prog. Photovolt: Res. Appl.*, 12, 69–92, 2004.

[24] European Commission. Critical raw materials for the *EU*, 2010.

[25] F. A. Cotton and G. Wilkinson. *Advances in Organic Chemistry*. Wiley Interscience, New York, 4th Edition, 1980.

[26] S. Delbos. Kësterite thin films for photovoltaics: a review. *EPJ Photovolt.*, 3, 35004, 2012.

[27] J. M. Doña and J. Herrero. Chemical bath deposition of CdS thin films: An approach to the chemical mechanism through study of the film microstructure. *J. Electrochem. Soc.*, 144(11), 1081–4091, 1997.

[28] D. Drouin, A. R. Couture, D. Joly, X. Tastet, V. Aimez and R. Gauvin. CASINO V2.42 – A fast and easy-to-use modeling tool for scanning electron microscopy and microanalysis users. *Scanning*, 29(3), 92–101, 2007.

[29] A. Ennaoui, M. Lux-Steiner, A. Weber, D. Abou-Ras, I. Kötschau, H.W. Schock, R. Schurr, A. Hölzing, S. Jost, R. Hock, T. Voß, J. Schulze and A. Kirbs. Cu_2ZnSnS_4 thin film solar cells from electroplated precursors: Novel low-cost perspective. *Thin Solid Films*, 517(7), 2511–2514, 2009.

[30] J. Pantoja E. and X. Mathew. Influence of the thickness on structural, optical and electrical properties of chemical bath deposited CdS thin films. *Solar Energy Materials and Solar Cells*, 76(3), 313–322, 2003.

[31] B. Eren, L. Marot, G. Gunzburger, P.O. Renault, Th. Glatzel, R. Steiner and E. Meyer. Hydrogen-induced buckling of gold films. *J. Phys. D: Appl. Phys.*, 47, 025302, 2014.

[32] T. Ericson, T. Kubart, J. J. Scragg and C. Platzer-Björkman. Reactive sputtering of precursors for Cu_2ZnSnS_4 thin film solar cells. *Thin Solid Films*, 520(0), 7093–7099, 2012.

[33] A. Fairbrother, E. Garcia-Hemme, V. Izquierdo-Roca, X. Fontanè, F. A. Pulgarín-Agudelo, O.Vigil-Galán, A. Pérez-Rodríguez and E. Saucedo. Development of a selective chemical etch to improve the conversion efficiency of Zn-rich Cu_2ZnSnS_4 solar cells. *J. Am. Chem. Soc.*, 134(19), 8018–8021, 2012.

[34] P. A. Fernandes, P. M. P. Salomé and A. F. da Cunha. Growth and Raman scattering characterization of Cu_2ZnSnS_4 thin films. *Thin Solid Films*, 517(7), 2519–2523, 2009.

[35] P. A. Fernandes, P. M. P. Salomé and A. F. da Cunha. Precursors' order effect on the properties of sulfurized Cu_2ZnSnS_4 thin films. *Semiconductor Science Technology*, 24(10), 105013, 2009.

[36] P. A. Fernandes, P. M. P. Salomé and A. F. da Cunha. Cu_xSnS_{x+1} (x = 2,3) thin films grown by sulfurization of metallic precursors deposited by dc magnetron sputtering. *Physica Status Solidi (c)*, 7(3-4), 901–904, 2010.

[37] P. A. Fernandes, P. M. P. Salomé and A. F. da Cunha. A study of ternary Cu_2SnS_3 and Cu_3SnS_4 thin films prepared by sulfurizing stacked metal precursors. *Journal of Physics D: Applied Physics*, 43(21), 215403, 2010.

[38] P.A. Fernandes, P.M.P. Salomé and A.F. da Cunha. Study of polycrystalline Cu_2ZnSnS_4 films by Raman scattering. *Journal of Alloys and Compounds*, 509(28), 7600–7606, 2011.

[39] P.A. Fernandes, P.M.P. Salomé, A.F. da Cunha and Björn-Arvid Schubert. Cu_2ZnSnS_4 solar cells prepared with sulphurized dc-sputtered stacked metallic precursors. *Thin Solid Films*, 519(21), 7382–7385, 2011.

[40] X. Fontané, L. Calvo-Barrio, V. Izquierdo-Roca, E. Saucedo, A. Pérez-Rodriguez, J. R. Morante, D. M. Berg, P. J. Dale and S. Siebentritt. In-depth resolved Raman scattering analysis for the identification of secondary phases:

Characterization of Cu_2ZnSnS_4 layers for solar cell applications. *Applied Physics Letters*, 98(18), 181905, 2011.

[41] X. Fontané, V. Izquierdo-Roca, E. Saucedo, S. Schorr, V.O. Yukhymchuk, M.Ya. Valakh, A. Pérez-Rodríguez and J.R. Morante. Vibrational properties of stannite and kesterite type compounds: Raman scattering analysis of $Cu_2(Fe,Zn)SnS_4$. *Journal of Alloys and Compounds*, 539(0), 190–194, 2012.

[42] T. A. M. Friedlmeier. *Multinary Compounds and Alloys for Thin-Film Solar Cells: Cu_2ZnSnS_4 and $Cu(In,Ga)(S,Se)_2$*. PhD thesis, Stuttgart University, Institut für Physikalische Elektronik, 2001.

[43] T. M. Friedlmeier, H. Dittrich and H.W. Schock. Growth and characterization of Cu_2ZnSnS_4 and $Cu_2ZnSnSe_4$ thin films for photovoltaic applications. In *Institute of Physics Conference Series*, 152, B, p. 345–348, 1998. Paper presented at the 11th Int. Conf. on Ternary and Multinary Compounds, ICTMC-11, Salford, 8–12 1997.

[44] J. Ge, Y. Wu, C. Zhang, S. Zuo, J. Jiang, J. Ma, P. Yang and J. Chu. Comparative study of the influence of two distinct sulfurization ramping rates on the properties of Cu_2ZnSnS_4 thin films. *Applied Surface Science*, 258(19), 7250–7254, 2012.

[45] P. J. George, A. Sanchez-Juarez and P.K. Nair. Modification of electrical, optical and crystalline properties of chemically deposited CdS films by thermal diffusion of indium and tin. *Semicond. Sci. Technol*, 11, 1090–1095, 1996.

[46] T. Gershon, B. Shin, T. Gokmen, S. Lu, N. Bojarczuk and S. Guha. Relationship between Cu_2ZnSnS_4 quasi donor-acceptor pair density and solar cell efficiency. *Appl. Phys. Lett*, 103, 193903, 2013.

[47] M. Green. The path to 25% silicon solar cell efficiency: History of silicon cell evolution. *Progress in Photovoltaics: Research and Applications*, 17, 183–189, 2009.

[48] Martin A. Green. *Solar Cells*. The University of New South Wales, 1998.

[49] Greenpeace and the European Photovoltaic Industry Association. Solar generation *VI*, 2011.

[50] O. Gunawan, T. K. Todorov and D. B. Mitzi. Loss mechanisms in hydrazine-processed $Cu_2ZnSn(Se,S)_4$ solar cells. *Applied Physics Letters*, 97(23), 233506, 2010.

[51] L. Gutay, A. Redinger, R. Djemour and S. Siebentritt. Lone conduction band in $Cu_2ZnSnSe_4$. *Appl. Phys. Lett.*, 100(10), 102113–4, 2012.

[52] H. Hadouda, J. Pouzet, J.C. Bernede and A. Barreau. MoS_2 thin film synthesis by soft sulfurization of a molybdenum layer. *Materials Chemistry and Physics*, 42(4), 291–297, 1995.

[53] R. Haight, A. Barkhouse, O. Gunawan, B. Shin, M. Copel, M. Hopstaken and D. B. Mitzi. Band alignment at the $Cu_2ZnSn(S_xSe_{1-x})_4$/CdS interface. *Applied Physics Letters*, 98(25), 253502, 2011.

[54] S. R. Hall, J. T. Szymanski and J. M. Stewart. Kesterite, $Cu_2(Zn,Fe)SnS_4$ and stannite, $Cu_2(Fe,Zn)SnS_4$) , structurally similar but distinct minerals. *The Canadian Mineralogist*, 16(2), 131–137, 1978.

[55] G. Hanna, T. Glatzel, S. Sadewasser, N. Ott, H. Strunk, U. Rau and J. H. Werner. Texture and electronic activity of grain boundaries in cu(in,ga)se2 thin films. *Appl. Phys. A: Mater. Sci. Process.*, 82, 1â€“7, 2006.

[56] X. He and H. Shen. First-principles study of elastic and thermo-physical properties of kesterite-type Cu_2ZnSnS_4. *Physica B*, 406, 4604–4607, 2011.

[57] H. Hiroi, N. Sakai and H. Sugimoto. Cd-free $5×5cm^2$-sized Cu_2ZnSnS_4 submodules. In *Proc. 37th IEEE Photovoltaic Specialists Conf. (PVSC)*, 002719–002722, 2011.

[58] H. Hiroi, N. Sakai, S. Muraoka, T. Katou and H. Sugimoto. Development of high efficiency submoduls with Cd-free buffer layer. In *Photovoltaic Specialists Conference (PVSC), 2012, 38th IEEE*, 2012.

[59] W. M. Hlaing Oo, J. L. Johnson, A. Bhatia, E. A. Lund, M. M. Nowell and M. A. Scarpulla. Grain Size and Texture of Cu_2ZnSnS_4 Thin Films Synthesized by Cosputtering Binary Sulfides and Annealing: Effects of Processing Conditions and Sodium. *Journal of Electronic Materials*, 40, 2214–2221, 2011.

[60] K. Hönes, E. Zscherpel, J. Scragg and S. Siebentritt. Shallow defects in Cu_2ZnSnS_4. *Physica B: Condensed Matter*, 404(23-24), 4949–4952, 2009.

[61] M. Ichimura and Y. Nakashima. Analysis of atomic and electronic structures of Cu_2ZnSnS_4 based on first-principle calculation. *Japanese Journal of Applied Physics*, 48(9), 090202, 2009.

[62] K. Ito and T. Nakazawa. Electrical and optical properties of stannite-type quaternary semiconductor thin films. *Japanese Journal of Applied Physics*, 27(Part 1, No. 11), 2094–2097, 1988.

[63] P.J. Sebastian and Hailin Hu. Identification of the impurity phase in chemically deposited CdS thin films. *Adv. Mater. Opt. Electron.*, 4, 407–412, 1994.

[64] A Janotti and C. G. Van de Walle. New insights into the role of native point defects in ZnO. *Journal of Crystal Growth*, 287, 58, 2006.

[65] A. Janotti and C. G. Van de Walle. Fundamentals of zinc oxide as a semiconductor. *Rep. Prog. Phys.*, 72, 126501, 2009.

[66] K. Jimbo, R. Kimura, T. Kamimura, S. Yamada, S. M. Win, H. Araki, K. Oishi and H. Katagiri. Cu_2ZnSnS_4-type thin film solar cells using abundant materials. *Thin Solid Films*, 515(15), 5997–5999, 2007.

[67] L. J. Johnson, H. Nukala, A. Bhatia, W.M. Hlaing Oo, W. R. Loren, M. A. Scarpulla and E. A. Lund. Effects of 2nd phases, stress and Nja at the Mo/Cu_2ZnSnS_4 interface. In *Proc. of the 2010 MRS Spring meeting*, volume 1268, page 1268-EE03-03, 2010.

[68] S. Jost. *The formation of $CuInSe_2$-based thin-film solar cell absorbers from alternative low-cost precursors*. PhD thesis, Universität Erlangen-Nürnberg, 2008.

[69] H. Katagiri. Cu_2ZnSnS_4 thin film solar cells. *Thin Solid Films*, 480–481, 426–432, 2005. Presented at EMRS 2004.

[70] H. Katagiri, K. Jimbo, W.S. Maw, K. Oishi, M. Yamazaki, H. Araki and A. Takeuchi. Development of CZTS-based thin film solar cells. *Thin Solid Films*, 517(7), 2455–2460, 2009.

[71] H. Katagiri, K. Jimbo, M. Tahara, H. Araki and K. Oishi. The influence of the composition ratio on CZTS-based thin film solar cells. In *Proceedings of the European Material Research Society Conference, 2009*, 1165, p. M04–01, 2009.

[72] H. Katagiri, K. Jimbo, S. Yamada, T. Kamimura, W. S. Maw, T. Fukano, T. Ito and T. Motohiro. Enhanced conversion efficiencies of Cu_2ZnSnS_4-based thin film solar cells by using preferential etching technique. *Applied Physics Express*, 1(4), 041201, 2008.

[73] H. Katagiri, K. Saitoh, T. Washio, H. Shinohara, T. Kurumadani and S. Miyajima. Development of thin film solar cell based on Cu_2ZnSnS_4 thin films. *Solar Energy Materials and Solar Cells*, 65(1-4), 141–148, 2001.

[74] T. Kato, H. Hiroi, N. Sakai, S. Muraoka and H. Sugimoto. Characterization of front and back interfaces on Cu_2ZnSnS_4 thin-film solar cells. In *Proc. of the 27th EU-PVSEC*, 2012.

[75] W. Kautek, H. Gerischer and H. Tributsch. The role of carrier diffusion and indirect optical transitions in the photoelectrochemical behavior of layer type d-band semiconductors. *Journal of The Electrochemical Society*, 127(11), 2471–2478, 1980.

[76] A. Klein, T. Loher, Y. Tomm, C. Pettenkofer and W. Jaegermann. Band lineup between CdS and ultra high vacuum-cleaved $CuInS_2$ single crystals. *Appl. Phys. Lett.*, 70(10), 1299–1301, 1997.

[77] E. A. Kraut, R. W. Grant, J. R. Waldrop and S. P. Kowalczyk. Precise determination of the valence-band edge in X-ray photoemission spectra: Application to measurement of semiconductor interface potentials. *Phys. Rev. Lett.*, 44(24), 1620–1623, 1980.

[78] J. Langford and P. Louer, D.and Scardi. Effect of a crystallite size distribution on x-ray diffraction line profiles and wholepowder-pattern fitting. *J. Appl. Crystallogr.*, 33, 964–974, 2000.

[79] N. Lejmi and O. Savadogo. The effect of heteropolyacids and isopolyacids on the properties of chemically bath deposited cds thin films. *Solar Energy Materials and Solar Cells*, 70, 71–83, 2001.

[80] M. Leoni, T. Confente and P. Scardi. PM2K: a flexible program implementing whole powder pattern modelling. *Z. Kristallogr. Suppl.*, 2006 (suppl_23_2006), 249–254, 2006.

[81] L. Ley, R. A. Pollak, F. R. McFeely, S. P. Kowalczyk and D. A. Shirley. Total valence-band densities of states of III-V and II-VI compounds from X-ray photoemission spectroscopy. *Phys. Rev. B*, 9(2), 600–621, 1974.

[82] J. Li, D. B. Mitzi and V. B. Shenoy. Structure and electronic properties of grain boundaries in earth-abundant photovoltaic absorber $Cu_2ZnSnSe_4$. *ACS Nano*, 5(11), 8613–8619, 2011.

[83] D. Lincot, R. Ortega-Borges and M. Froment. *Phil. Mag. B*, 68, 185, 1993.

[84] F. Liu, K. Zhang, Y. Lai, J. Li, Z. Zhang and Y. Liu. Growth and characterization of Cu_2ZnSnS_4 thin films by DC reactive magnetron sputtering for photovoltaic applications. *Electrochemical and Solid-State Letters*, 13(11), H379–H381, 2010.

[85] D.C. Look, G. C. Farlow, P. Reunchan, S. Limpijumnong, S. B. Zhang and K. Nordlund. Evidence for native-defect donors in n-type ZnO. *Phys. Rev. Lett*, 95, 225502, 2005.

[86] L. S. Price, I.P. Parkin, A. M. E. Hardy and R. J. H. Clark. Atmospheric Pressure Chemical Vapor Deposition of Tin Sulfides (SnS, Sn_2S_3 and SnS_2) on Glass. *Chem. Mater.*, 11(7), 1792-1799, 1999.

[87] P. Lukashev, W. R. L. Lambrecht, T. Kotani and M. van Schilfgaarde. Electronic and crystal structure of $Cu_{2-x}S$: Full-potential electronic structure calculations. *Physical Review B*, 76(19), 195202, 2007.

[88] T. Maeda, S. Nakamura and T. Wada. Electronic structure and phase stability of In-free photovoltaic semiconductors, $Cu_2ZnSnSe_4$ and Cu_2ZnSnS_4 by first-principles calculation. In *Material Research Society Symposium Proceedings*, volume 1165, 2009.

[89] T. Maeda, S. Nakamura and T. Wada. First-principles calculations of vacancy formation in In-free photovoltaic semiconductor $Cu_2ZnSnSe_4$. *Thin Solid Films*, 519(21), 7513-7516, 2011.

[90] R. Mainz, A. Singh, S. Levcenko, M. Klaus, C. Genzel, K. M. Ryan and Unold T. Phase-transition-driven growth of compound semiconductor crystals from ordered metastable nanorods. *Nature Communications*, 2014.

[91] J. R. Mann, N. Vora and I. L. Repins. In situ thickness measurements of chemical bath-deposited CdS. *Solar Energy Materials and Solar Cells*, 94(2), 333–337, 2010.

[92] M. A. Martinez, C. Guillen and J. Herrero. Morphological and structural studies of CBD-CdS thin films by microscopy and diffraction techniques. *Applied Surface Science*, 136, 8–16, 1998.

[93] R. J. Matson, O. Jamjoum, A. D. Buonaquisti, P. E. Russell, L. L. Kazmerski, P. Sheldon and R. K. Ahrenkiel. Metal contacts to $CuInSe_2$. *Solar Cells*, 11(3), 301–305, 1984.

[94] H. Matsushita, T. Ichikawa and A. Katsui. Structural, thermodynamical and optical properties of Cu_2-II-IV-VI_4 quaternary compounds. *Journal of Materials Science*, 40(8), 2003–2005, 2005.

[95] H. Matsushita and A. Katsui. Materials design for Cu-based quaternary compounds derived from chalcopyrite-rule. *Journal of Physics and Chemistry of Solids*, 66, 1933–1936, 2005.

[96] P. S. McLeod, L. D. Partain, D. E. Sawyer and T. M. Peterson. Photoconductivity of sputtered Cu_xS films. *Applied Physics Letters*, 45(4), 472–474, 1984.

[97] F. Meillaud, A. Shah, C. Droz, E. Vallat-Sauvain and C. Miazza. Efficiency limits for single-junction and tandem solar cells. *Solar Energy Materials and Solar Cells*, 90, 2952–2959, 2006.

[98] T. Minemoto, T. Matsui, H. Takakura, Y. Hamakawa, T. Negami, Y. Hashimoto, T. Uenoyama and M. Kitagawa. Theoretical analysis of the effect of conduction band offset of window/CIS layers on performance of CIS solar cells using device simulation. *Solar Energy Materials and Solar Cells*, 67(1-4), 83–88, 2001.

[99] D. B. Mitzi, O. Gunawan, T. K. Todorov, K. Wang and S. Guha. The path towards a high-performance solution-processed kesterite solar cell. *Solar Energy Materials and Solar Cells*, 95, 1421–1436, 2011.

[100] N. Moritake, Y. Fukui, M. Oonuki, K. Tanaka and H. Uchiki. Preparation of Cu_2ZnSnS_4 thin film solar cells under non-vacuum condition. *Physica Status Solidi C*, 6(5), 1233–1236, 2009.

[101] K. Moriya, J. Watabe, K. Tanaka and H. Uchiki. Characterization of Cu_2ZnSnS_4 thin films prepared by photo-chemical deposition. *Physica Status Solidi C*, 3, 2848–2852, 2006.

[102] K. Moriya, K. Tanaka and H. Uchiki. Fabrication of Cu_2ZnSnS_4 thin-film solar cell prepared by pulsed laser deposition. *Japanese Journal of Applied Physics*, 46(9A), 5780–5781, 2007.

[103] A. Nagoya, R. Asahi, R. Wahl and G. Kresse. Defect formation and phase stability of Cu_2ZnSnS_4 photovoltaic material. *Physical Review B*, 81(11), 113202, 2010.

[104] S. Nakamura, T. Maeda and T. Wada. Electronic structure of stannite-type $Cu_2ZnSnSe_4$ by first principles calculations. *Physica Status Solidi C Current Topics*, 6, 1261–1265, 2009.

[105] N. Nakayama and K. Ito. Sprayed films of stannite Cu_2ZnSnS_4. *Applied Surface Science*, 92, 171–175, 1996.

[106] W.G. Nilsen. *Phys. Rev.*, 182, 838, 1969.

[107] H. Nozaki, K. Shibata and N. Ohhashi. Metallic hole conduction in CuS. *Journal of Solid State Chemistry*, 91, 306–311, 1991.

[108] U.S. Department of Energy. Critical material strategy, December 2010.

[109] I. D. Olekseyuk, I. V. Dudchak and L. V. Piskach. Phase equilibria in the Cu_2S-ZnS-SnS_2 system. *Journal of Alloys and Compounds*, 368(1-2), 135–143, 2004.

[110] A. I. Oliva, O. Solis-Canto, R. Castro-Rodriguez and P. Quintana. Formation of the band gap energy on CdS thin films growth by two different techniques. *Thin Solid Films*, 391, 28–35, 2001.

[111] R. Ondo-Ndong, G. Ferblantier, M. Al Kalfioui, A. Boyer and A. Foucaran. Properties of RF magnetron sputtered zinc oxide thin films. *Journal of Crystal Growth*, 255, 130–135, 2003.

[112] J. Paier, R. Asahi, A. Nagoya and G. Kresse. Cu_2ZnSnS_4 as a potential photovoltaic material: A hybrid Hartree-Fock density functional theory study. *Physical Review B*, 79(11), 115126, 2009.

[113] C. Persson. *Appl. Phys. Lett.*, 93, 072106, 2008.

[114] C. Persson. Electronic and optical properties of Cu_2ZnSnS_4 and $Cu_2ZnSnSe_4$. *Journal of Applied Physics*, 107(5), 053710, 2010.

[115] W. Pitschke, H. Hermann and N. Mattern. The influence of surface roughness on diffracted X-ray intensities in Bragg-Brentano geometry and its effect on the structure determination by means of Rietveld analysis. *Powder Diffr.*, 8, 74–83, 1993.

[116] A. Polizzotti, I. Repins, R. Noufi, S. H. Wei and D. Mitzi. The state and future prospects of kesterite photovoltaics. *Energy & Environ. Sci.*, 6, 3171-3182, 2013.

[117] A. E. Rakhshani and Al-Azab A. S. Characterization of cds films prepared by chemical-bath deposition. *J. Phys.: Condens. Matter*, 12, 8745–8755, 2000.

[118] A. Redinger, D. M. Berg, P. J. Dale and S. Siebentritt. The consequences of kesterite equilibria for efficient solar cells. *Journal of the American Chemical Society*, 133(10), 3320–3323, 2011.

[119] R. F. Reilman, A. Msezane and S. T. Manson. Relative intensities in photoelectron spectroscopy of atoms and molecules. *Journal of Electron Spectroscopy and Related Phenomena*, 8(5), 389–394, 1976.

[120] I. Repins, N. Vora, C. Beall, S.H. Wei, Y. Yan, M. Romero, G. Teeter, H. Du, B. To, M. Young and R. Noufi. Kesterites and chalcopyrites: A comparison of close cousins. In *Proceedings of the Materials Research Society Spring Meeting (2011), San Francisco (USA)*, 2011. NREL/CP-5200-51286.

[121] S. J. Roosendaal. *Passivation Mechanisms in the Initial Oxidation of Iron by Oxygen and Water Vapor*. PhD thesis, Utrecht University, 1999.

[122] S. Siebentritt and S. Schuler. Defects and transport in the wide gap chalcopyrite cugase2. *J. Phys. Chem. Solids*, 64, 1621-1626, 2003.

[123] A. Sanchez-Juarez and A. Ortíz. Effects of precursor concentration on the optical and electrical properties of Sn_xS_y thin films prepared by plasma-enhanced chemical vapour deposition. *Semiconductor Science and Technology*, 17(9), 931, 2002.

[124] A. Santoni, F. Biccari, C. Malerba, M. Valentini, R. Chierchia and A. Mittiga. Valence band offset at the CdS/Cu_2ZnSnS_4 interface probed by X-ray photoelectron spectroscopy. *Journal of Physics D: Applied Physics*, 46(17), 175101, 2013.

[125] S. Schorr and G. Gonzalez-Aviles. In-situ investigation of the structural phase transition in kesterite. *Physica status solidi (a)*, 206, 1054–1058, 2009.

[126] S. Schorr. The crystal structure of kesterite type compounds: A neutron and X-ray diffraction study. *Solar Energy Materials and Solar Cells*, 95, 1482–1488, 2011.

[127] S. Schorr, H.J. Hoebler and M. Tovar. A neutron diffraction study of the stannite-kesterite solid solution series. *European Journal of Mineralogy*, 19(1), 65–73, 2007.

[128] R. Schurr, A. Hölzing, S. Jost, R. Hock, T. Voβ, J. Schulze, A. Kirbs, A. Ennaoui, M. Lux-Steiner, A. Weber, I. Kötschau and H.W. Schock. The crystallisation of Cu_2ZnSnS_4 thin film solar cell absorbers from co-electroplated Cu-Zn-Sn precursors. *Thin Solid Films*, 517(7), 2465–2468, 2009.

[129] J. H. Scofield. Hartree-Slater subshell photoionization cross-sections at 1254 and 1487 eV. *Journal of Electron Spectroscopy and Related Phenomena*, 8(2), 129–137, 1976.

[130] J. H. Scofield, A. Duda, D. Albin, B.L. Ballard and P.K. Predecki. Sputtered molybdenum bilayer back contact for copper indium diselenide-based polycrystalline thin-film solar cells. *Thin Solid Films*, 260(1), 26–31, 1995.

[131] J.J. Scragg. *Studies of Cu_2ZnSnS_4 films prepared by sulfurization of electrodeposited precursors*. PhD thesis, Department of Chemistry, University of Bath, UK, 2010.

[132] J. J. Scragg, P. J. Dale, L. M. Peter, G. Zoppi and I. Forbes. New routes to sustainable photovoltaics: evaluation of Cu_2ZnSnS_4 as an alternative absorber material. *Physica Status Solidi B Basic Research*, 245, 1772–1778, 2008.

[133] J. J. Scragg, T. Ericson, X. Fontané, V. Izquierdo-Roca, A. Perez-Rodriguez, T. Kubart, M. Edoff and C. Platzer-Björkman. Rapid annealing of reactively sputtered precursors for Cu_2ZnSnS_4 solar cells. *Prog. Photovolt: Res. Appl.*, 2012.

[134] J. J. Scragg, T. Ericson, T. Kubart, M. Edoff and C. Platzer-Björkman. Chemical insights into the instability of Cu_2ZnSnS_4 films during annealing. *Chem. Mater.*, 23(20), 4625–4633, September 2011.

[135] M. P. Seah and W. A. Dench. Quantitative electron spectroscopy of surfaces: A standard data base for electron inelastic mean free paths in solids. *Surf. Interface Anal.*, 1(1), 2–11, 1979.

[136] J.-S. Seol, S.-Y. Lee, J.-C. Lee, H.-D. Nam and K.-H. Kim. Electrical and optical properties of Cu_2ZnSnS_4 thin films prepared by RF magnetron sputtering process. *Solar Energy Materials and Solar Cells*, 75(1-2), 155–162, 2003.

[137] C. Sevik and T. Çağın. Assessment of thermoelectric performance of Cu_2ZnSnX_4, X=S, Se and Te. *Applied Physics Letters*, 95(11), 112105, 2009.

[138] T. Shimada, F. S. Ohuchi and B. A. Parkinson. Work function and photothreshold of layered metal dichalcogenides. *Japanese Journal of Applied Physics*, 33, 2696–2698, 1994.

[139] B. Shin, O. Gunawan, Y. Zhu, N. A. Bojarczuk, S. J. Chey and S. Guha. Thin film solar cell with 8.4% power conversion efficiency using an earth-abundant Cu_2ZnSnS_4 absorber. *Prog. Photovolt: Res. Appl.*, 21, 72–76, 2013.

[140] B. Shin, Y. Zhu, N. A. Bojarczuk, S. J. Chey and S. Guha. Control of an interfacial $MoSe_2$ layer in $Cu_2ZnSnSe_4$ thin film solar cells: 8.9% power conversion efficiency with a tin diffusion barrier. *Appl. Phys. Lett.*, 101(5), 053903–4, 2012.

[141] W. Shockley and H. J. Queisser. Detailed balance limit of efficiency of p-n junction solar cells. *J. Appl. Phys.*, 32, 510–519, 1961.

[142] S. Siebentritt. What limits the efficiency of chalcopyrite solar cells? *Solar Energy Materials and Solar Cells*, 95(6), 1471–1476, 2011.

[143] H. Sugimoto, H. Hiroi, N. Sakai, S. Muraoka and T. Katou. Over 8% efficiency Cu_2ZnSnS_4 submodules with ultra-thin absorber. *IEEE Photovolatic Specialist Conference*, page 2997, 2011.

[144] G. Suresh Babu, Y. B. Kishore Kumar, P. Uday Bhaskar and V. Sundara Raja. Effect of Cu/(Zn+Sn) ratio on the properties of co-evaporated $Cu_2ZnSnSe_4$ thin films. *Solar Energy Materials and Solar Cells*, 94(2), 221–226, 2010.

[145] G. Suresh Babu, Y. B. Kishore Kumar, P. Uday Bhaskar and V. Sundara Raja. Effect of post-deposition annealing on the growth of $Cu_2ZnSnSe_4$ thin films for a solar cell absorber layer. *Semiconductor Science Technology*, 23(8), 085023, August 2008.

[146] R. Swanepoel. Determination of the thickness and optical constants of amorphous silicon. *Journal of Physics E: Scientific Instruments*, 16, 1214–1222, 1983.

[147] S. M. Sze. *Physics of Semiconductor Devices 1981*. Wiley, New York, 2nd Edition, 1981.

[148] H. Tanaka, T. Shimakawa, T. Miyata, H. Sato and T. Minami. Effect of AZO film deposition conditions on the photovoltaic properties of AZO-Cu_2O heterojunctions. *Applied Surface Science*, 244(1-4), 568–572, 2005.

[149] K. Tanaka, Y. Fukui, N. Moritake and H. Uchiki. Chemical composition dependence of morphological and optical properties of Cu_2ZnSnS_4 thin films deposited by sol-gel sulfurization and Cu_2ZnSnS_4 thin film solar cell efficiency. *Solar Energy Materials and Solar Cells*, 95(3), 838–842, 2011.

[150] T. Tanaka, T. Nagatomo, D. Kawasaki, M. Nishio, Q. Guo, A. Wakahara, A. Yoshida and H. Ogawa. Preparation of Cu_2ZnSnS_4 thin films by hybrid sputtering. *Journal of Physics and Chemistry of Solids*, 66(11), 1978–1981, 2005.

[151] T. Tanaka, A. Yoshida, D. Saiki, K. Saito, Q. Guo, M. Nishio and T. Yamaguchi. Influence of composition ratio on properties of Cu_2ZnSnS_4 thin films fabricated by co-evaporation. *Thin Solid Films*, 518(21, Supplement 1), S29–S33, 2010.

[152] T. K. Todorov, K. B. Reuter and D. B. Mitzi. High-efficiency solar cell with earth-abundant liquid-processed absorber. *Advanced Materials*, 22(20), E156–E159, 2010.

[153] J. R. Tuttle, M. Contreras, D. S. Albin and R. Noufi. Physical, chemical and structural modifications to thin-film $CuInSe_2$-based photovoltaic devices. In *in Proceedings of the22nd IEEE Photovoltaic Specialists Conference*, volume 2, pages 1062–1067, 1991.

[154] M. Valentini, C. Malerba, F. Biccari, E. Salza, A. Santoni, C. L. Azanza Ricardo, P. Scardi and A. Mittiga. Study of CZTS solar cells obtained from two different types of precursors. In *Proc. 28th Eur. Photov. Solar Energy Conf. , Paris*, page 2459, 2013.

[155] B. Vermang, H. Goverde, V. Simons, In. De Wolf, Johan Meersschaut, S.Tanaka, J. John, J. Poortmans and R. Mertens. A study of blister formation in ALD Al_2O_3 grown on silicon. In *38th IEEE Photovoltaic Specialists Conference (PVSC)*, pages 001135–001138, 2012.

[156] T. Wada, N. Kohara, Nishiwaki S. and T. Negami. *Thin Solid Films*, 387, 118, 2001.

[157] R. Wagner and H. D. Wiemhöfer. Hall effect and conductivity in thin films of low temperature chalcocite Cu_2S at 20°C as a function of stoichiometry. *Journal of Physics and Chemistry of Solids*, 44, 801–805, 1983.

[158] J. R. Waldrop, R. W. Grant, S. P. Kowalczyk and E. A. Kraut. Measurement of semiconductor heterojunction band discontinuities by X-ray photoemission spectroscopy. *J. Vac. Sci. Technol. A*, 3(3), 835–841, 1985.

[159] A. Walsh, S. Chen, S.-H. Wei and X.-G. Gong. Kesterite thin-film solar cells: Advances in materials modelling of Cu_2ZnSnS_4. *Adv. Energy Mater.*, 2(4), 400–409, 2012.

[160] K. Wang, O. Gunawan, T. Todorov, B. Shin, S. J. Chey, N. A. Bojarczuk, D. Mitzi and S. Guha. Thermally evaporated Cu_2ZnSnS_4 solar cells. *Applied Physics Letters*, 97(14), 143508, 2010.

[161] K. Wang, B. Shin, K. B. Reuter, T. Todorov, D. B. Mitzi and S. Guha. Structural and elemental characterization of high efficiency Cu_2ZnSnS_4 solar cells. *Applied Physics Letters*, 98(5), 051912, 2011.

[162] W. Wang, M. T. Winkler, O. Gunawan, T. Gokmen, T. K. Todorov, Y. Zhu and D. B. Mitzi. Device characteristics of CZTSe thin-film solar cells with 12.6 efficiency. *Advanced Energy Materials*, 2013.

[163] A. Weber, R. Mainz and H. W. Schock. On the Sn loss from thin films of the material system Cu-Zn-Sn-S in high vacuum. *Journal of Applied Physics*, 107(1), 013516, 2010.

[164] A. Weber. *Wachstum von Dünnschichten des Materialsystems Cu-Zn-Sn-S*. PhD thesis, Friedrich-Alexander-Universität Erlangen-Nürnberg, 2009.

[165] A. Weber, R. Mainz, T. Unold, S. Schorr and H.-W. Schock. In-situ XRD on formation reactions of Cu_2ZnSnS_4 thin films. *Physica Status Solidi C*, 6(5), 1245–1248, 2009.

[166] W. O. Winer. Molybdenum disulfide as a lubricant: A review of the fundamental knowledge. *Wear*, 10(6), 422, 1967.

[167] C. Wu, Z. Hu, C. Wang, H. Sheng, J. Yang and Y. Xie. Hexagonal Cu_2SnS_3 with metallic character: Another category of conducting sulfides. *Applied Physics Letters*, 91, 143104, 2007.

[168] www.firstsolar.com.

[169] www.solar frontier.com.

[170] H. Yoo and J. Kim. Comparative study of Cu_2ZnSnS_4 film growth. *Solar Energy Materials and Solar Cells*, 95(1), 239–244, 2011.

[171] J. Yoo, J. Lee, S. Kim, K. Yoon, I. Jun Park, S. K. Dhungel, B. Karunagaran, D. Mangalaraj and Junsin Yi. High transmittance and low resistive ZnO:Al films for thin film solar cells. *Thin Solid Films*, 480-481, 213–217, 2005.

[172] J. Zhang and L. Shao. Cu_2ZnSnS_4 thin films prepared by sulfurizing different multilayer metal precursors. *Science in China Series E: Technological Sciences*, 52(1), 269–272, 2009.

[173] Y. Zhang, X. Yuan, X. Sun, B.-C. Shih, P. Zhang and W. Zhang. Comparative study of structural and electronic properties of Cu-based multinary semiconductors. *Physical Review B*, 84(7), 075127, 2011.

[174] Z. Zhou, Y. Wang, D. Xu and Y. Zhang. Fabrication of Cu_2ZnSnS_4 screen printed layers for solar cells. *Solar Energy Materials and Solar Cells*, 94, 2042–2045, 2010.

[175] A. Zunger and A. J. Freeman. Local-density self-consistent energy-band structure of cubic CdS. *Phys. Rev. B*, 17(12), 4850–4863, 1978.